

# **Linking Detector Radiometry from Milliwatts Radiant Power to Single Photons**

Bridging the Radiometric Gap

D I S S E R T A T I O N

zur Erlangung des akademischen Grades

Doctor rerum naturalium  
im Fach Physik

eingereicht an der  
Mathematisch-Naturwissenschaftlichen Fakultät I  
Humboldt-Universität zu Berlin

von

**Dipl.-Phys. Ingmar Müller**

Präsident der Humboldt-Universität zu Berlin:  
Prof. Dr. Jan-Hendrik Olbertz

Dekan der Mathematisch-Naturwissenschaftlichen Fakultät I:  
Prof. Stefan Hecht, Ph.D.

Gutachter/innen:

1. Prof. Dr. Oliver Benson
2. Prof. Dr. Mathias Richter
3. Prof. Achim Peters, Ph.D.

**Tag der mündlichen Prüfung:** 18.12.2013



*Ich widme diese Arbeit  
meiner Frau Daniela sowie meinen Söhnen Mika und Niklas.*



## Abstract

This thesis addresses the bridging of the radiometric gap in the transition from classical radiometry to the few and single photon radiometry. In this context, two main tasks were emphasised.

First: A new radiometric primary detector standard for wavelengths between 400 nm and 800 nm, suitable for classical and few photon radiometry, the so-called “Predictable Quantum Efficient Detector” (PQED) was characterised and validated. For the validation of the PQED, the relative uncertainties achievable in classical radiometry and, in particular, with cryogenic radiometers had to be reduced to a level of  $10^{-5}$  with the commissioning of a new cryogenic radiometer facility.

Second: A calibration method for single photon detectors in the visible and NIR has been used which is based on the unique properties of synchrotron radiation. This calibration method allows radiometric single photon detector calibrations with the lowest uncertainties reported so far. This method can be used to calibrate free space and fibre-coupled single photon detectors traceable to the international system of units at practically every desired optical wavelength.

With the new cryogenic radiometer, the PQED, and the calibration method based on synchrotron radiation, the uncertainties in radiometry have been significantly reduced in the range from milliwatts of radiant power down to attowatts corresponding to a few photons per second.



## Zusammenfassung

Das Ziel dieser Dissertation ist das Schließen der radiometrischen Lücke zwischen der klassischen Radiometrie und der Radiometrie im Bereich weniger und einzelner Photonen. In dieser Arbeit wurden dazu zwei wesentliche Themen bearbeitet. Erstens, die Charakterisierung und Validierung eines neuen radiometrischen Detektorprimärnormals für den Wellenlängenbereich von 400 nm bis 800 nm basierend auf Silizium-Photodioden. Dieses neuartige Primärnormal kann sowohl in der Radiometrie im Bereich weniger Photonen als auch in der klassischen Radiometrie eingesetzt werden, der sogenannte “Predictable Quantum Efficient Detector” (PQED). Der PQED wurde im Rahmen dieser Arbeit charakterisiert und experimentell validiert. Für die Validierung war es nötig, die relativen Unsicherheiten der klassischen Radiometrie und insbesondere der Kryoradiometrie, deutlich zu verringern. Mit der Inbetriebnahme eines neuen Kryoradiometers wurde das Ziel, in den Unsicherheitsbereich von ca.  $10^{-5}$  vorzudringen, erreicht.

Zweitens, es wurde eine Kalibriermethode für Einzelphotonendetektoren eingesetzt, rückgeführt auf das internationale Einheitensystem, die auf den einzigartigen Eigenschaften von Synchrotronstrahlung basiert. Diese Methode kann benutzt werden um sowohl Freistrah- als auch fasergekoppelte Einzelphotonendetektoren bei praktisch jeder gewünschten Wellenlänge zu kalibrieren und erreicht im Moment die weltweit geringsten Messunsicherheiten.

Mit dem neuen Kryoradiometer, dem PQED und dem auf Synchrotronstrahlung basierenden Kalibrierverfahren sind die erreichbaren Messunsicherheiten in der Radiometrie im Bereich von wenigen Photonen bis zu Strahlungsleistungen im Milliwattbereich deutlich reduziert worden.



# Contents

<b>List of Abbreviations</b>	<b>xi</b>
<b>1 Introduction</b>	<b>1</b>
1.1 Background . . . . .	1
1.2 Aim of this Work . . . . .	3
1.2.1 Objectives . . . . .	5
1.2.2 Outline . . . . .	6
<b>2 Improving Radiant Power Scales</b>	<b>7</b>
2.1 Current State of Detector Based Radiant Power Scales . . . . .	8
2.1.1 Detectors with Predictable Quantum Efficiency . . . . .	8
2.1.2 Cryogenic Electrical Substitution Radiometer . . . . .	9
2.1.3 Trap Detectors as Transfer Standards . . . . .	10
2.2 Development of a Laser Source for Measurements at the 10 ppm Standard Uncertainty Level . . . . .	15
2.2.1 Setup of the Power Stabilised Laser Source . . . . .	15
2.2.2 Characterisation of the Power Stabilised Laser Source . . . . .	16
2.3 Improving Cryogenic Radiometry . . . . .	20
2.3.1 Improving the Primary Standard for Radiant Power Measurements of PTB . . . . .	20
2.3.2 Uncertainty Budget of the Radiant Power Measurement with the CRCF . . . . .	23
2.4 Improving Detectors with Predictable Quantum Efficiency . . . . .	29
2.4.1 Modelling the PQED . . . . .	29
2.4.2 Validating the Predictable Quantum Efficient Detector . . . . .	38
2.5 Conclusions . . . . .	54
<b>3 Bridging the Radiometric Gap</b>	<b>57</b>
3.1 Single Photon Detectors . . . . .	58
3.1.1 Types of Single Photon Detectors . . . . .	58
3.1.2 Characteristics of Single Photon Detectors . . . . .	62
3.2 Current Methods for Single Photon Detector Calibrations . . . . .	64
3.2.1 Calibration Methods of Single Photon Detectors Without Refer- encing to a Primary Standard . . . . .	64
3.2.2 Calibration Method of Single Photon Detectors Referencing to a Primary Standard . . . . .	67

## Contents

3.3	Bridging the Radiometric Gap with Synchrotron Radiation . . . . .	71
3.3.1	Introduction to Synchrotron Radiation based Source Standards . .	71
3.3.2	Determination of the Photon Statistics of the Metrology Light Source	74
3.3.3	Traceable Calibration of Free Space Single Photon Avalanche Diodes	83
3.3.4	Traceable Calibration of Fibre-coupled Superconducting Single Photon Detectors . . . . .	93
3.4	Conclusions . . . . .	99
<b>4</b>	<b>Conclusions and Outlook</b>	<b>101</b>
	<b>Bibliography</b>	<b>105</b>
	<b>List of Figures</b>	<b>117</b>
	<b>List of Tables</b>	<b>125</b>

# List of Abbreviations

**Candela** Joint Research Project “Candela - Towards Photon based Standards”

**CMC** Calibration and Measurement Capabilities

**CMI** Český metrologický institut, Czech Republic

**CRCF** Cryogenic Radiometer Calibration Facility

**DMM** Digital Multimeter

**DUT** Device under Test

**GRT** Germanium Resistance Thermometer

**GUM** Guide to the Expression of Uncertainties in Measurements

**INRIM** Istituto Nazionale di Ricerca Metrologica, Italy

**JUSTERVESENET** Norwegian Metrology Service, Norway

**AS Metrosert** Central Office of Metrology, Estonia

**MIKES** Mittatekniikan keskus Finland, Finland

**MIQC** Joint Research Project “Metrology for Industrial Quantum Communications”

**MLS** Metrology Light Source

**NIST** National Institute of Standards and Technologies, USA

**NMI** National Metrology Institute

**PCT** Parametric Current Transformer

**PTB** Physikalisch-Technische Bundesanstalt, Germany

**PTR** Physikalisch-Technische Reichsanstalt

**ppm** Parts per Million

**PQED** Predictable Quantum Efficient Detector

**QKD** Quantum Key Distribution

**SI** International System of Units

## *List of Abbreviations*

**SNSPD** Superconducting Nanowire Single Photon Detector

**SPAD** Single Photon Avalanche Diode

**SPDC** Spontaneous Parametric Down Conversion

# 1 Introduction

Major technologies and applications of the twenty-first century, such as information and communications technologies, earth observation, manufacturing, healthcare, life sciences, solid state lightning, displays, as well as photonics for safety and security are substantially driven by optical technologies. To gather access to the advantages provided by optical technologies in each of these fields one needs something to “see” the light. To see the light, the necessary “eye”, i.e. the photodetector, will be different for the specific applications depending on wavelength and radiant power. Very often - almost always - photodetectors in research and development are used as metrological devices, i.e. to provide quantitative results.

## 1.1 Background

A current field of research in radiometry is to connect the two different “metrological universes”: On the one hand, conventional radiometry at moderate and high radiant power levels, as it is necessary, for instance, to measure the solar irradiation on the earth (earth observation), and on the other hand, single photon measurements in the quantum universe, as it is needed, for example to investigate single atoms or molecules, e.g. in life sciences. This is a true challenge for the quantitative measurement of electromagnetic radiation, as more than ten orders of magnitude of radiant power have to be covered. It is obvious that the detectors made for the two “universes” will be different in many ways as well. The detector sizes will differ, the detection mechanism will be different, et cetera.

A significant problem that arises from the variety of detector types and the “non-equivalence” of allegedly identical detectors is the comparability of the quantities measured with these detectors. The only way to compare, e.g., spaceborne observation results with measurements on earth, and every comparison between detectors that absolutely measure a certain quantity, is an uninterrupted traceability chain to the International System of Units (SI) [1]. If this traceability chain is provided, results obtained, e.g. in the United States of America, can be compared with results obtained in Germany or anywhere else in the world. The importance of the scientific field of metrology is easily underestimated as it is so commonplace for all of us that a screw manufactured in China will fit into a nut manufactured in Germany.

Indeed, it is no coincidence that the economic growth at the end of the 19th century was accompanied by the foundation of the first national metrology institutes (NMI) worldwide and in Germany of the “Physikalisch-Technische Reichsanstalt”, the predecessor of the “Physikalisch-Technische Bundesanstalt” (PTB), in 1877. At this time, the label “Made in Germany” was introduced by the “Merchandise Marks Act 1887” [2]. The label

## 1 Introduction

“Made in Germany” was used intentionally in the British Empire to distinguish between low quality products produced in Germany from higher quality products produced in the Commonwealth. However, it became - driven by metrological improvements - one of the most valuable trademarks worldwide. The metrological work in Germany, led to the availability of high-quality standards and tools but it also gave a boost to fundamental scientific work. The discovery of famous and world-changing physical laws, such as the laws of thermal radiation marking the starting point of quantum mechanics, was decisively supported by the researches of Wilhelm Wien, Otto Lummer and Ferdinand Kurlbaum at the Physikalisch-Technische Reichsanstalt. The work of these pioneers in the field of radiometry led to the development of an electrically heated blackbody and the first absolute measuring radiometer based on the electrical substitution principle [3, 4, 5].

Today, the “Calibration and Measurement Capabilities” (CMCs) of the NMIs for the different quantities can be seen at [www.bipm.org](http://www.bipm.org). The mass, for instance, can be measured at PTB with an uncertainty of  $2 \cdot 10^{-10}$  kg for customer calibrations. These are very low uncertainties compared with the CMCs for radiometric and photometric units. At PTB, the spectral responsivity of general photodetectors can be disseminated to customers by the use of cryogenic radiometers based on the electrical substitution principle with an uncertainty of 0.01% at laser lines between 238 nm and 1014 nm. Although these uncertainties are sufficient for most applications, the relative uncertainties associated with measurements of radiant power are the highest among the SI units.

In this sense, optically driven technologies lack a set of very low-uncertainty standards and radiant power scales, traceable to the SI, available to customers and stakeholders to further push the growth of optical and photonics industries. This is of utmost importance for applications at the single or few photon level, where the traceability to national standards is often disseminated with uncertainties at the few percent level. For instance, the emerging field of quantum cryptography and quantum communications with its high security concerns depends on certified/calibrated systems. For example, the SARG04-protocol [6], applied in commercial quantum key distribution (QKD) systems, requires detectors with known detection efficiency to establish secure communication [7]. Therefore, traceable calibration of single photon detectors is a key component for secure communications for the users of QKD systems. The detection efficiency of detectors used in a commercial QKD system directly influences the performance and operation distance of such a system and, hence, it is a crucial figure of merit to compare systems. To gain further momentum, traceability for the few photon regime has to be established to provide a worldwide comparability of the techniques and devices. Also spaceborne applications like space and earth observation gain scientific impact if the optical measurements, that often cover several orders of magnitude of radiant power, are traceable to the SI. Indeed, to provide traceability to scales for different wavelength ranges from the x-ray range to mm-waves and radiant power levels from single photons to Watts is a rather new challenge in radiometry. Especially the traceability to the SI of the single photon regime is a research topic that gains a lot of interest as the quantum communication emerges to become a mature industry. These demands led to increased research efforts on this topic and the achievable uncertainties for calibrations of single

photon detectors decreased by a factor of about 50 from 10% to 0.18% [8] in the last 25 years. Single photon detectors can be calibrated traceable to primary standards or primary methods, i.e. traceable to the cryogenic radiometer and, for instance, a primary calibration method based on spontaneous decays of one photon in an optical parametric process into a pair of photons.

However, the few photon radiometry is a field that differs from classical radiometry. While in classical radiometry the radiant power is measured in terms of watt, photons are counted in the few photon radiometry. “Classical” detectors like photodiodes, thermopiles and cryogenic radiometers are not well suited for radiant power levels in the few photon regime, thus, special detectors such as single photon detectors and photon number resolving detectors are used in the few photon radiometry. Most single photon detectors apply an internal amplification after the absorption of a single photon that has a much lower noise level than classical detectors. In this amplification process, the information on the composition of the detected event, e.g. the number of detected photons or the arrival time, is usually sacrificed in order to obtain a macroscopic output signal. The cryogenic radiometer, the most advanced primary detector standard in radiometry, is normally operated in the radiant power range from 1  $\mu$ W to 1 mW while single photon detectors are used for photon fluxes from several photons/s to  $10^8$  photons/s, i.e from approximately 1 aW to approximately 10 pW. Thus, traceability of radiant power measurements covering at least six orders of magnitude of radiant power have to be achieved with a significant reduction of uncertainties to bridge the radiometric gap.

Finally, the Candela is the only SI unit that provides a direct link to biology (especially life sciences). Hence, lower uncertainties in radiometry and photometry will enable a higher quality of life as light sources and ambient conditions can be more accurately adjusted to suit one of the most important human senses: vision.

## 1.2 Aim of this Work

The aim of this work was the reduction of the uncertainties associated with the measurement of radiometric units in classical and few / single photon radiometry and to bridge the radiometric gap between the mature classical radiometry based on radiant power measurements and the emerging field of few photon / single photon radiometry. As will be shown in the following chapters, these two goals are inseparably linked and interdependent. In order to reduce the uncertainties in radiometric measurements a new primary detector standard for measurements in the wavelength range from 400 nm to 800 nm, the “Predictable Quantum Efficient Detector” (PQED) based on photodiodes with a surface charge induced n-p-junction [9] was developed within a cooperation of five national metrology institutes, namely, Mittateknikan keskus Finland (MIKES), Physikalisch-Technische Bundesanstalt (PTB), Istituto Nazionale di Ricerca Metrologica (INRIM), Central Office of Metrology (AS METROSERT), and the Norwegian Metrology Service (Justervesenet). The development, simulation and validation of the PQED was one of the major subjects of the joint research project “The Quantum Candela” (“Candela”

## 1 Introduction

project) within the European Metrology Research Programme. The design and construction was realised by MIKES. The simulation of the response to optical radiation was done by Justervesenet and Metroser. The experimental characterisation and validation of the single photodiodes and the PQED itself was the task of PTB. INRIM supervised the work. The PQED has been absolutely characterised within this thesis. Finally, the development was an iterative process that merged the contributions of the five NMIs. The focus of the measurements presented in this thesis is put on electro-optical properties of single induced n-p-junction photodiodes and the PQED. These results were needed as input for the modelling and the experimental validation of the external quantum efficiency as well as for design improvements. The design of the detector and its components are expected to enable measurements of radiant power with a relative uncertainty of 1 ppm (ppm = parts per million) as a long-term objective. To reach this low uncertainty level, the internal and external quantum efficiency of this detector has to be predicted with uncertainties at the ppm level and to be validated with equally low uncertainties.

For this purpose, the new cryogenic radiometer of PTB, that has been set-up in parallel to this work, has been equipped with a measurement setup to accommodate the PQED with the aim to significantly reduce the uncertainties when calibrating photodetectors against a cryogenic radiometer. Absolute radiometers based on the electrical substitution principle are used at the radiometric labs of PTB for more than hundred years. The aim to improve and to apply electrical substitution radiometers at the PTB follows a tradition of radiometric developments that goes back to the foundation times of the Physikalisch-Technische Reichsanstalt. The principle of electrical calibrated substitution radiometers has been invented here around 1891 [3] and was used to discover Wien's approximation [10] and eventually lead to the formulation of Planck's law [11].

Since the PQED is made of cryogenic photodiodes, which reduces the noise of the detector by several orders of magnitude, this type of detector has a sufficiently large dynamic range for the possible use as the only primary detector standard operating in both, the "classical" radiant power measurement regime as well as in the few photon regime where photon counting detectors are used. Thus, the PQED has the unique potential to notably reduce the level of uncertainty in radiometry and, furthermore, to bridge the radiometric gap with a primary detector standard. Hence, the PQED may make possible traceable calibrations of single photon detectors directly to a primary standard.

Two methods have been used to bridge the radiometric gap in this work. First, the so-called substitution method [12], where the reference detector and the single photon detector to be calibrated are irradiated with the same photon flux sequentially. If the PQED is used as a reference detector single photon detectors can be directly calibrated against a primary detector standard with this method. This will tremendously simplify the availability of radiant power scales for stakeholders and NMIs at the few photon level. In addition, a new method, that has been developed within the framework of this thesis, has been used, based on the unique properties of synchrotron radiation [13, 14]. The possibility to use synchrotron radiation to calibrate photon counting detectors traceable to CR in the spectral range from UV radiation to X-rays has been shown before [15, 16]. The advantage of this method is the operation of the single photon detector, as well as

the reference detector, under the best suitable power level conditions for the corresponding devices. For the work presented here, the synchrotron radiation based method [15] was adopted for the requirements of optical radiometry with the aim to further reduce the uncertainties achievable when calibrating single photon detectors. This method was used for calibrations in the visible and in the near infrared. The PQED could be used for this method, as well, and, thus, would simplify the traceability chain for the synchrotron method, too.

### 1.2.1 Objectives

In order to reduce the uncertainties associated with the measurement of radiometric and photometric units in the classical and the few photon radiometry and to bridge the radiometric gap the following objectives have to be accomplished to serve the aims of this work.

- To achieve low uncertainties in radiometric measurements a suitable radiation source is mandatory. To fulfil the demanding goals of this thesis, a power stabilised laser source has to be developed that enables radiometric measurements at the 10 ppm level.
- The photodiodes to be used in the PQED have to be characterised. To characterise the single photodiodes a facility to measure the uniformity of the relative spectral responsivity has to be setup. Furthermore, a facility to measure the linearity of the spectral responsivity has to be adopted to be compatible with the PQED, the power stabilised DFB laser and the necessary measurement equipment such as transimpedance amplifiers.
- For the fabrication and simulation of the photodiodes produced for the PQED several additional characterisation measurements have to be performed. For instance, the dependence of the photocurrent on the applied bias voltage and the temperature of the photodiodes has to be measured with high accuracy.
- The facility to accommodate the new cryogenic radiometer of PTB has to be set up. Additionally, an uncertainty budget of the new cryogenic radiometer facility has to be compiled based on a thorough characterisation of the facility.
- The PQED has to be validated by verifying the predicted spectral responsivity of the PQED by measurements with the new cryogenic radiometer of PTB with an uncertainty of the validation of the order of tens of ppm.
- An uncertainty budget of the validation of the PQED with the new cryogenic radiometer facility has to be compiled.
- The experimental results obtained in this work have to be evaluated and merged to provide input for the development of the PQED and to prove the feasibility of this new detector to be used as a primary standard.

## 1 Introduction

To bridge the radiometric gap by means of synchrotron radiation four objectives have to be fulfilled:

- The types of single photon detectors to be calibrated in terms of detection efficiency have to be chosen. Furthermore, the single photon detectors to be calibrated have to be characterised in order to achieve a reduced calibration uncertainty.
- Calibration setups have to be established and characterised to enable the calibration of fibre-coupled and free space single photon detectors by means of synchrotron radiation.
- The photon statistics of the synchrotron radiation source used in this work has to be determined. The uncertainty associated with the emission statistics of the radiation can become dominant depending on the actual calibration conditions.
- An uncertainty budget for the radiometric calibration of single photon detectors by means of synchrotron radiation has to be compiled.

### 1.2.2 Outline

In chapter 2, the achieved necessary improvements of the radiometric tools and of the radiant power scales within this work are described. The improved radiant power scales are provided by the new cryogenic radiometer of PTB and the PQED, the newly developed and only potential primary detector standard suitable for the use both in the few photon radiometry and the classical radiometry. To predict the spectral responsivity of the PQED, the internal quantum deficiency [17] and the reflectance losses have been simulated [18]. This prediction is validated by characterising a set of single photodiodes as they are built into the PQED and by measurements with the new cryogenic radiometer of PTB [19] to compare the predicted and measured external quantum deficiency. This comparison with the cryogenic radiometer is of utmost importance. It is the only experimental method to validate the prediction with experimental uncertainties that are similar to the uncertainties of the prediction. Furthermore, it is a prerequisite for the validation of every primary standard to be compared with other primary standards of the same quantity.

In chapter 3, the radiometric gap is bridged. Two established methods, based on spontaneous parametric down conversion [20, 21] and the so-called “substitution” method [12] are described with own experimental results for the latter one. In addition, a method for the traceable calibration of single photon detectors in the visible and near infrared based on the properties of synchrotron radiation is introduced [13].

In chapter 4, a conclusion on the methods and devices used and developed in this work is given.

## 2 Improving Radiant Power Scales

An absolute radiant power scale is needed for, e.g. radiometry, photometry, and radiation thermometry. It can be based on absolute radiation sources like electron storage rings [22] or calculable blackbodies [23] operated as primary source standards, but also on absolute detectors like cryogenic electrical substitution radiometers [24] and detectors with predictable quantum efficiency. When the use of the p-n-junction in silicon as a primary detector standard was proposed by Jon Geist in 1979 [25], the two most important approaches to absolute radiometry, i.e. electrical substitution radiometers and photodiodes with calculated response, were similar in terms of achievable uncertainties. An important improvement of absolute radiant power measurements was achieved with the introduction of cryogenic electrical substitution radiometers in the late 1980s [26]. This type of radiometer reduced the uncertainty of radiant power measurements by more than one order of magnitude down to about 0.01%.

A recent trend in optical radiometry, followed by this work, is to use the advanced software models and the experiences in semiconductor processing to develop primary detector standards made from silicon photodiodes.

Chapter 2.1 gives an introduction into detector based radiant power scales.

In chapter 2.2 the development and characterisation of a power stabilised laser radiation source, a prerequisite for the reduction of radiometric uncertainties, is described.

Chapter 2.3 describes the improvement of the new detector based radiant power scale of PTB, based on a state-of-the-art cryogenic radiometer, which is necessary for the ultra-low uncertainty validation of the potential primary detector standard based on custom-made silicon photodiodes, the so-called “Predictable Quantum Efficient Detector” (PQED). The PQED and its experimental validation is described in chapter 2.4.

### 2.1 Current State of Detector Based Radiant Power Scales

Optical detectors are mainly divided into two types: thermal detectors, that sense a change of temperature and quantum detectors that generate charge carriers after photon absorption. A widely used example for a quantum detector is a photodiode [27], i.e. a photo detector based on the inner photoeffect [28], while pyroelectric radiometers and bolometers are grouped as thermal detectors. Thermal detectors have a spectrally flat responsivity which facilitates the use as absolute detectors to realise radiant power scales. The advantage of quantum detectors is their high-speed response and higher signal to noise ratio as compared to thermal detectors.

#### 2.1.1 Detectors with Predictable Quantum Efficiency

The use of the quantum efficiency of the p-n-junction as an absolute radiometric standard was proposed by Jon Geist [25] in the late 1970s. At this time the uncertainties that were stated for the prediction of the photodiode's response to optical radiation were lower than the uncertainty of 0.3% achievable with state-of-the-art electrical substitution radiometers [29].

The prediction of the spectral responsivity of the photodiode can be based on two different approaches:

- Self-Calibration [29, 30, 31]: Here the losses in the front region and the bulk region of the photodiode are determined by applying a bias voltage minimising the internal losses due to recombination of radiation generated electron-hole pairs. The losses can be calculated from the ratio of the photocurrent with and without reverse bias. Nevertheless some values needed for this method have to be calculated by simulating the values for an ideal photodiode [30]. With this method the spectral responsivity of a silicon photodiode can be determined with a relative standard uncertainty of  $3.5 \cdot 10^{-4}$  [30].
- Simulation of detector response: Here the losses, like the reflectance of the photodiode, the internal quantum deficiency, i.e. the recombination of electron-hole pairs, etc., of the photodiode are used to model the response of photodiodes to radiation. The measurement of the reflectance is straight forward. The internal quantum deficiency is obtained by solving drift-diffusions-equations of the photodiodes [32]. To improve the accuracy of the model it is advantageous to apply this method to detectors with very low losses and a simple structure like photodiodes with an induced junction (inversion layer photodiodes) [9] as proposed in [31]. The relative standard uncertainty of the calculation of the internal quantum deficiency has been estimated in [32] to 9%. However, the resulting internal quantum deficiency of high quality silicon photodiodes is well below 1% and, thus, the combined standard uncertainty, including the uncertainty of the reflectance, etc., of this method is  $9 \cdot 10^{-4}$  and, thus, similar to the self-calibration method.

In this work the latter approach is pursued to obtain an absolute detector with predictable quantum efficiency, the PQED (see chapter 2.4). The improved software mod-

els available [17] may eventually make possible primary detector standards based on photodiodes with equal or lower uncertainties as they occur in the classical cryogenic radiometry.

### 2.1.2 Cryogenic Electrical Substitution Radiometer

Cryogenic electrical substitution radiometers (cryogenic radiometer) are the most advanced primary detector standard to establish radiant power scales from the X-ray to the NIR [24, 33, 34, 35, 15, 36, 37, 38, 39] as they enable radiometric measurements with the lowest uncertainties. Even the feasibility to work as primary standard for terahertz radiation has been studied [40] and the traceability of the terahertz radiant power scale of PTB is provided by a cryogenic radiometer as described in [40]. A review of the evolution of and operation principle of absolute radiometers going back to the year 1797 can be found in [41] and [42].

In principle, an electrical substitution radiometer is a thermometer which measures a temperature rise due to the absorption of radiant power (see Figure 2.1). This radiant

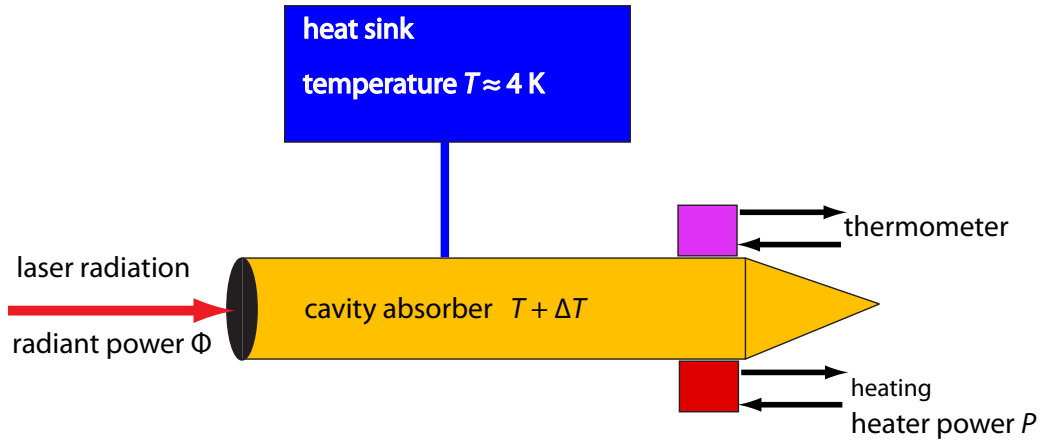


Figure 2.1: Schematic of the operation principle of an electrical substitution radiometer (see text). A detailed description is given in chapter 2.3.

power is substituted by electrically heating the detector to the same temperature. Thus, the traceability of the radiant power measurement to the SI is obtained from the equivalence of radiant power and electrical heating power. The detector, i.e. the receiving cavity, is connected to a constant temperature heat sink at a reference temperature  $T_{\text{ref}}$  with a thermal conductance  $G_{\text{th}}$ . A radiant flux  $\Phi$  incident on the cavity gives a temperature rise of  $T - T_{\text{ref}} = \Phi/G_{\text{th}}$ . This equation only holds if losses can be neglected. In this case, the radiant power is given by  $\Phi = i_h^2 R$ , with  $i_h$  the current to maintain temperature stability and  $R$  the resistance of the heater. Below 100 K, the temperature of the cavity is typically measured with Germanium Resistance Thermometers (GRTs) which are very sensitive in the temperature range from 1 K to 10 K.

The challenge in operating electrical substitution radiometer is to characterise the losses precisely in order to apply the appropriate corrections to the power equivalence relationship [43]. There exist several systems working at room temperature such as the PMO6 system [44] and the membrane type electrical substitution radiometer described in [45]. However, the lowest experimental uncertainties can be achieved with cryogenic radiometer [26, 46, 47] as, for instance, the Cryorad III system which was used in the experiments described in this work. The operation of a cryogenic radiometer is more complicated in terms of operation and needed infrastructure such as, for instance, to provide the availability of liquid nitrogen and liquid helium. The lower uncertainties of cryogenic radiometer are not achieved by a higher sensitivity of the detector or a lower intrinsic noise level, but by the smaller corrections needed, because of less radiative or convective losses. The main design goal of a electrical substitution radiometer is to have as small and as few corrections as possible. The uncertainties, commonly achieved with the PMO6 system are of the order of 0.06% [44] while cryogenic radiometer can measure the radiant power at discrete laser lines with uncertainties of about 0.003% [47]. The main corrections and uncertainties of cryogenic radiometer and how they can be measured and reduced are described in chapter 2.3.1 using the example of a new cryogenic radiometer of PTB.

### 2.1.3 Trap Detectors as Transfer Standards

Trap detectors (see Figure 2.2) built from silicon photodiodes and calibrated against primary detector standards are the most common choice for secondary/working or transfer standards in the wavelength range from 400 nm to about 1000 nm. The properties of these detectors have been intensively studied in terms of linearity, polarisation dependence, spectral responsivity, reflectance and temporal stability [24, 48, 49, 50, 51, 52]. This type of detector makes radiant power measurements possible with low uncertainties as it incorporates the following qualities:

1. High external quantum efficiency of more than 99% in the visible wavelength range
2. High uniformity of the spectral responsivity in the central area of the detector of 0.02% or better
3. Low polarisation dependence of the spectral responsivity
4. High temporal stability in the visible wavelength range allowing for re-calibration periods of two years or more depending on the required uncertainties

Furthermore, trap detectors have been used in this work as monitor detectors and as feedback detectors for the different laser stabilisation systems used in this work, especially the system described in chapter 2.2.

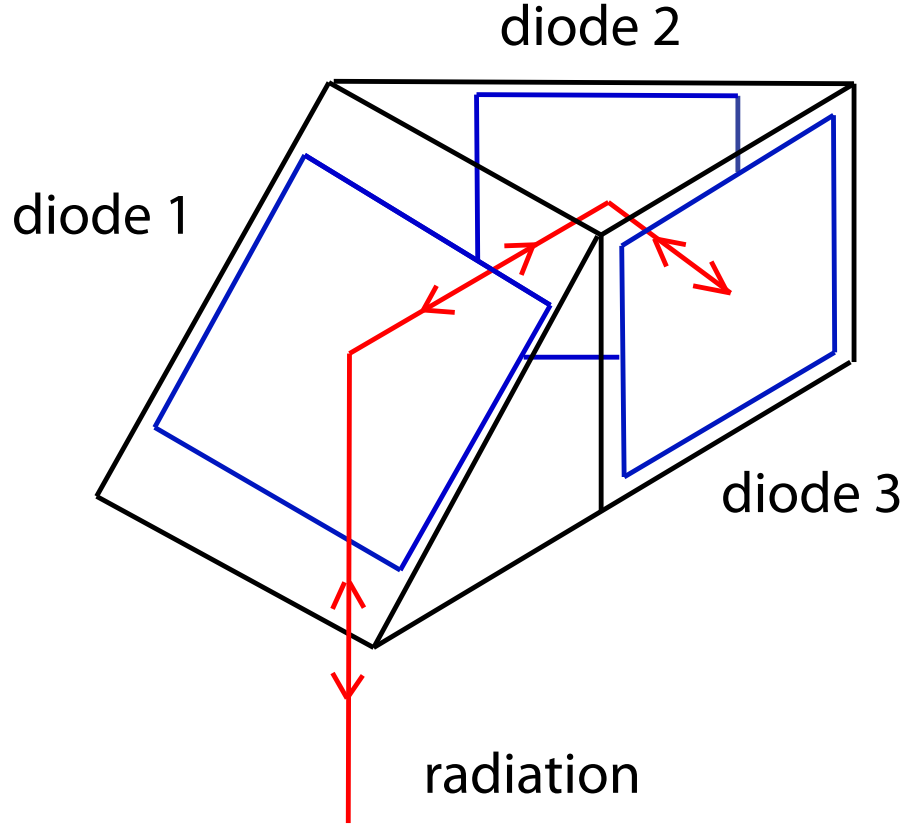


Figure 2.2: Schematic of a three-element reflection trap detector and the path of light (red line) inside the trap detector.

### Modelling of the Spectral Responsivity of Silicon Photodiodes

The spectral responsivity  $S(\lambda)$  of a detector is defined as

$$S(\lambda) = \frac{DO(\lambda)}{P(\lambda)}. \quad (2.1)$$

with  $DO(\lambda)$  the detector signal and  $P(\lambda)$  the incident radiant power. If there is a detector signal without optical radiation, than  $DO(\lambda)$  is given by:

$$DO(\lambda) = SIG_{\text{illuminated}} - SIG_{\text{dark}} \quad (2.2)$$

with  $SIG_{\text{illuminated}}$  the detector signal with optical radiation and  $SIG_{\text{dark}}$  the detector signal without optical radiation.

## 2 Improving Radiant Power Scales

For a photodiode,  $S(\lambda)$  becomes

$$S(\lambda) = \frac{eQE \cdot \lambda \cdot e}{h \cdot c} \approx \frac{eQE \cdot \lambda}{1240 \text{ nm}} \cdot \frac{\text{A}}{\text{W}} \quad (2.3)$$

with  $eQE$  the external quantum efficiency,  $\lambda$  the incident wavelength,  $e$  the elementary charge,  $h$  the Planck constant and  $c$  the speed of light. The external quantum efficiency is given by the ratio of incident photons to the number of photon generated charge carriers detectable with the external measurement circuit.

The spectral responsivity  $S(\lambda)$  of a detector can be directly measured with a cryogenic radiometer from the ratio of the photocurrent  $I$  of the detector and the spectral radiant power  $P$ , measured with the cryogenic radiometer (see also chapter 2.4.2). If the external quantum efficiency, and thus, the spectral responsivity is known for all wavelengths of interest, a radiant power scale can be provided by photodiode based detectors.

If the spectral responsivity  $S(\lambda)$  has only been determined at certain laser lines, the value for  $S(\lambda)$  has to be interpolated for wavelengths in between. This approach to estimate the external quantum efficiency of photodiodes is different to the self-calibration and the simulation of the detector response. At PTB a physical model, which was originally developed by Gentile et al. [53], is used to interpolate the external quantum efficiency of silicon photodiode trap detectors. It can be applied to detectors based on silicon photodiodes for wavelengths above 400 nm up to about 1000 nm. According to [25] the internal quantum efficiency  $\eta_i(\lambda)$  of a silicon photodiode of thickness  $h$  can be calculated by:

$$\eta_i(\lambda) = \int_0^h \exp[-\alpha(\lambda)x] \alpha(\lambda) P(x) dx \quad (2.4)$$

if the absorption coefficient  $\alpha(\lambda)$  and the collection efficiency  $P(x)$  are known.

The collection efficiency is a function of the distance from the photodiode surface  $x$  and describes the fraction of generated excess charge carriers that reach the p-n-junction, to be separated there and, thus, contribute to the photocurrent.  $P(x)$  is approximated by a simple model [54], starting with a collection efficiency,  $P_f$ , at the  $\text{SiO}_2/\text{Si}$  interface (see Figure 2.4 and 2.3). The value of  $P_f$  increases linearly with depth and reaches unity at the p-n-junction of the photodiode at depth  $t$ . Behind the p-n-junction the collection efficiency linearly decreases until it reaches the bulk value  $P_b$  of silicon at depth  $D$  which is maintained up to the rear surface. Assuming that each absorbed photon generates not more than one electron-hole pair, the resulting spectral responsivity  $S(\lambda)$  is given by:

$$S(\lambda) = \frac{[1 - r(\lambda)] \cdot \eta_i(\lambda) \cdot n_{\text{air}} \cdot \lambda \cdot e}{h \cdot c} \quad (2.5)$$

with  $r(\lambda)$  the reflectance of the detector,  $n_{\text{air}}$  the index of refraction of air,  $e$  the elementary charge,  $h$  Planck's constant,  $c$  the speed of light and  $\lambda$  the wavelength in air of the radiation. In the visible wavelength range, this interpolation allows the estimation of  $S(\lambda)$  with uncertainties down to 0.02 % [23]. However, for wavelengths in the UV and NIR this method is not sufficient to estimate the external quantum efficiency of transfer standards in between the wavelengths where the spectral responsivity has been

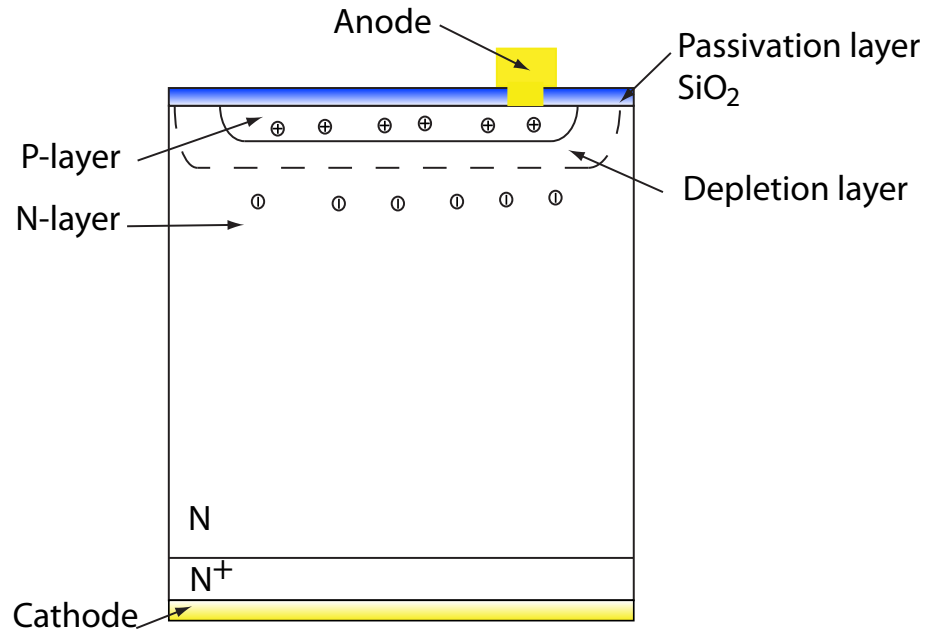


Figure 2.3: Cross section of a typical silicon photodiode. At the Si-SiO<sub>2</sub> interface, located at the intersection of the passivation layer and the bulk silicon, the collection efficiency  $P(x)$  is decreased (see text and Figure 2.4).

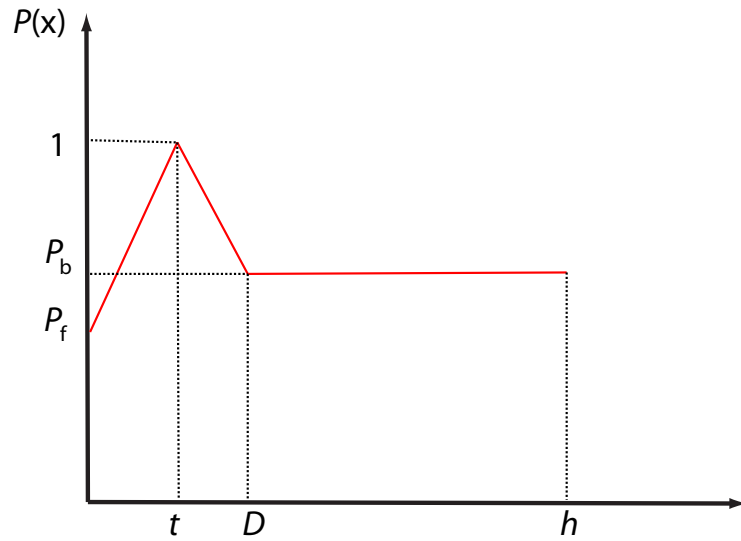


Figure 2.4: Collection efficiency of a silicon p-n-photodiode as a function of distance from the front surface (see text).

## *2 Improving Radiant Power Scales*

measured with cryogenic radiometer. To calibrate photodetectors without the need of interpolation between the laser lines, monochromator based cryogenic radiometer are used. At PTB, the so-called “CRI”-facility, has been developed to calibrate detectors in the UV and NIR by means of monochromatised broadband radiation [37].

## 2.2 Development of a Laser Source for Measurements at the 10 ppm Standard Uncertainty Level

A stabilised laser source is key to many aspects of radiometry. It is crucial for measurements of quantities such as the uniformity of the relative spectral responsivity of photodetectors, the nonlinearity, or the calibration of detectors against a cryogenic radiometer if low uncertainties are required (see chapter 2.4). All of these tasks are strongly affected by radiant power noise.

For the electro-optical characterisation of the PQED, a stabilised laser source had to be developed which enables radiometric measurements with uncertainties at the ppm level. While the demand for power stabilisation is ubiquitous the request for wavelength stability is relaxed. A slight change in the laser wavelength introduces only a minor uncertainty at measurements of, e.g., the relative spectral responsivity. According to (2.3), a change of the laser wavelength by 0.001 nm changes the measured spectral responsivity of a photodiode based detector, at a wavelength of 760 nm by approximately one ppm. The experimental requests on the radiometric laser source, for the characterisation and validation of the PQED, are a relative standard deviation of the measured laser power of better than 10 ppm for a period of 30 minutes and a wavelength change of less than 0.001 nm. The laser setup, developed to fulfil these requirements based on a distributed-feedback-(DFB)-laser (see for instance reference [55]) is described below. A diode laser system can be power stabilised by directly modulating the laser diode current. Laser diodes have a monotonous and, far beyond the laser threshold, an almost linear dependence of laser power and driving current. Hence, they offer a simple way of modulating and stabilising the laser power. The stabilisation frequency is depending on the laser diode driver and the controller that generates the modulation signal. Typical modulation frequencies are in the range from 0 Hz to 100 kHz. However, a modulation of the laser diode current can change the emitted wavelength and, hence, this method is not feasible for applications that require a wavelength stability of typically more than 1 pm. Furthermore, a change of the laser current can trigger a so-called “mode-hop”, i.e. an erratic fluctuation of the laser wavelength and power. The DFB laser was chosen, because the grating in this type of diode laser, enables the tuneability of the laser diode current and, hence, the laser power over a wide range without “mode-hops”.

### 2.2.1 Setup of the Power Stabilised Laser Source

The schematic of the setup of the power stabilised laser source is shown in Figure 2.5. The laser diode current is provided by a Newport 505B laser driver. The temperature of the laser diode is set to a value of 5 °C with a Newport 350B temperature controller. The operation of the laser diode at a temperature of 5 °C increases the stability of the emitted radiant power, which becomes less sensitive for changes in the ambient conditions and, in addition, increases the output power. The polarisation state of the beam is adjusted by a wave plate. The laser radiation output of the DFB-laser with a wavelength of 760 nm is expanded [56] with a spatial filter to about 4 mm to resemble the calibration conditions at the new cryogenic radiometer facility of PTB (see chapter 2.3). Wedged

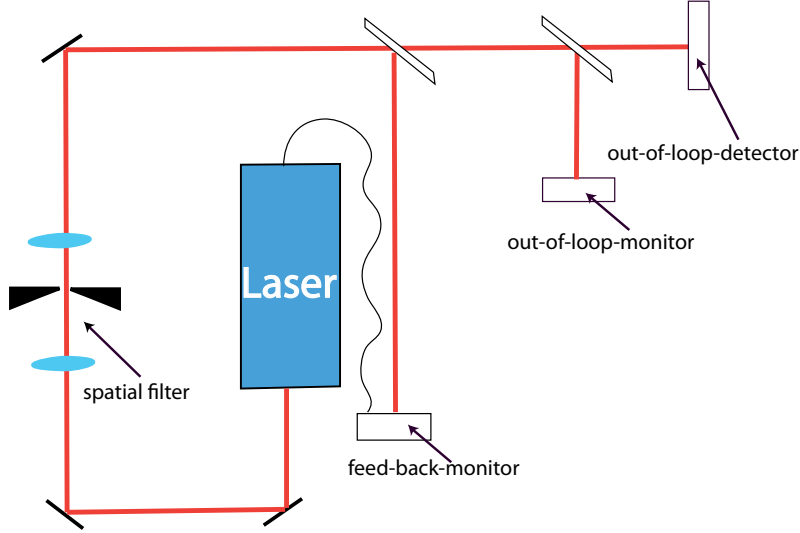


Figure 2.5: Schematic of the stabilised laser source. The laser beam of the DFB-laser with a wavelength of 760 nm is expanded with the spatial filter to a diameter of about 4 mm. Wedged glasses are used to decouple a fraction of the laser radiation for the feed-back-monitor and the out-of-loop-monitor.

glasses are used to decouple a fraction of the laser radiation (see Figure 2.6) for the feed-back-monitor and the out-of-loop-monitor. The output signal of the feed-back-monitor is used to modulate the laser diode current. The signal of the out-of-loop-monitor is used to correct for changes of the radiant power of the laser close to the out-of-loop-detector. The feed-back-monitor is a custom made, temperature controlled, trap-detector with integrated current-to-voltage converter. The out-of-loop detectors are trap detectors made of S1337 photodiodes from Hamamatsu Photonics K.K., Japan and are used in a power regime where no non-linearities should occur, i.e. below 0.8 mW [57]. The output of the feed-back-monitor is fed into a custom made laser power controller that directly modulates the driving current of the laser diode. To stabilise the laser radiant power, the voltage of the feed-back-monitor is compared with a low noise temperature stabilised voltage source within the laser power controller. The wanted radiant power of the laser is measured with an out-of-loop trap-detector and monitored with an out-of-loop trap detector. The out-of-loop-detector and out-of-loop-monitor, used as substitutes for the PQED and monitor during the characterisation and validation measurements of the PQED, are fed into low noise current-to-voltage converters and are read out by two synchronised Agilent 3458A digital multimeter.

### 2.2.2 Characterisation of the Power Stabilised Laser Source

Directly modulating the laser diode current leads to a shift of the emitted laser wavelength. The dependence of the wavelength on the laser diode current was studied sep-

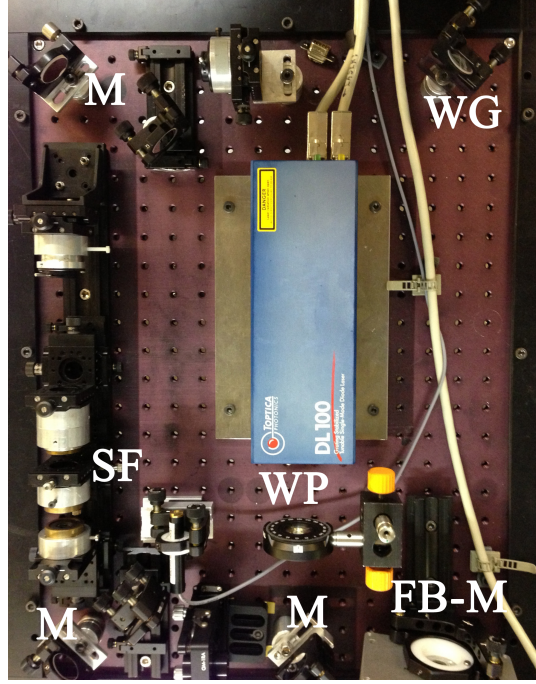


Figure 2.6: Photograph of the laser stabilisation setup with  $M$  the mirrors,  $WP$  the  $\lambda/2$ -wave-plate to control the polarisation direction,  $SF$  the spatial filter,  $WG$  the wedged-glass decoupler for the feed-back-monitor and  $FB-D$  the feed-back-monitor.

arately. A Burley spectrum analyser was used to measure the wavelength shift caused by adding a given current to the laser driving current. The laser driver is equipped with an external current modulation input. This input is internally connected in series with a high quality resistor and, thus, produces a current proportional to the applied external modulation voltage. The transfer function, that relates the wavelength shift and the applied modulation voltage was measured in 10 mA steps and at laser diode temperatures of 5 °C and 25 °C. The measured transfer function for the current induced wavelength change at a laser diode temperature of 5 °C by applying a voltage to the external modulation circuit of the laser driver is given by

$$\frac{\Delta\lambda}{\Delta U} = (0.036 \pm 0.001) \frac{\text{nm}}{\text{V}} . \quad (2.6)$$

However, for a well prepared setup, i.e. a cleaned beam profile, clean mirrors and proper alignment, the modulation current of the laser diode can become small and, hence, the resulting wavelength fluctuation. Figure 2.7 shows the wavelength shift which was calculated according to (2.6) for a typical measurement condition within a time span of 4 s. The standard deviation of the wavelength was calculated to 0.0014 pm. For the

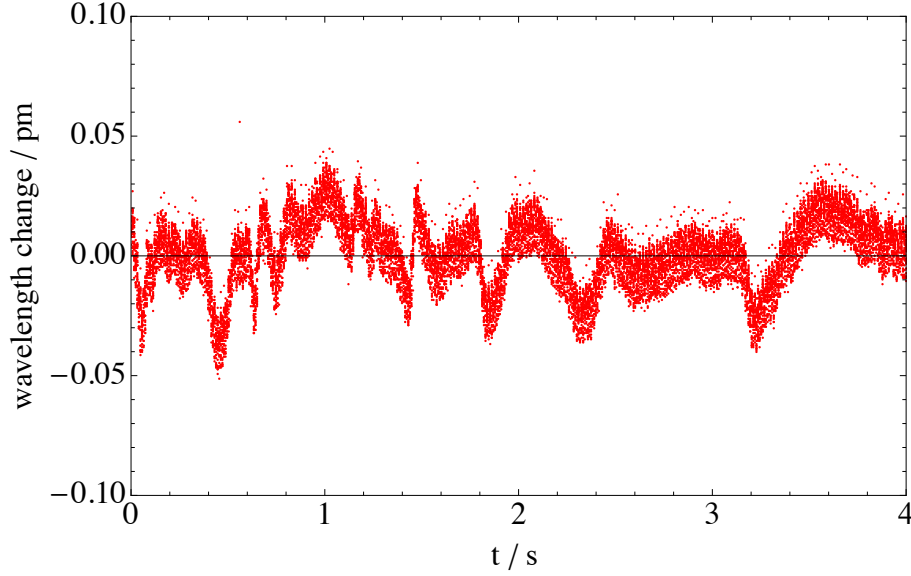


Figure 2.7: Calculated relative change of the emitted laser wavelength due to the modulation of the laser diode current for a period of 4 seconds. The wavelength change was calculated with (2.6) and the output signal of the laser power controller that directly modulates the laser diode current. The change is well below 0.001 nm and is therefore negligible.

application as a radiation source for radiometric measurements, this value is negligible and far better than what is necessary to characterise the PQED.

To determine the radiant power noise, the output of the current-to-voltage converters connected to the the out-of-loop-detectors was measured for a period of 30 minutes (see Figure 2.8). In addition, the same measurement was performed without external stabilisation using only the built-in current stabilisation of the laser driver (see Figure 2.9). For each measurement point, the photocurrent has been integrated over a period of five power line cycles, i.e. 0.1 s. In that way, influences coming from mains hum are minimised. As shown in Figure 2.9, the external stabilisation reduces the power noise of the wanted signal by a factor of approximately 50. The relative standard deviation of the power of the wanted laser radiation within 30 minutes was determined to be  $\sigma_{30 \text{ min}} = 4.3 \cdot 10^{-6}$  and  $\sigma_{300 \text{ min}} = 7.34 \cdot 10^{-6}$  for five hours of measurement. This is sufficient for the aims of this work and, thus, this setup was used for the characterisation and validation of the PQED and to bridge the radiometric gap with the “substitution-method”.

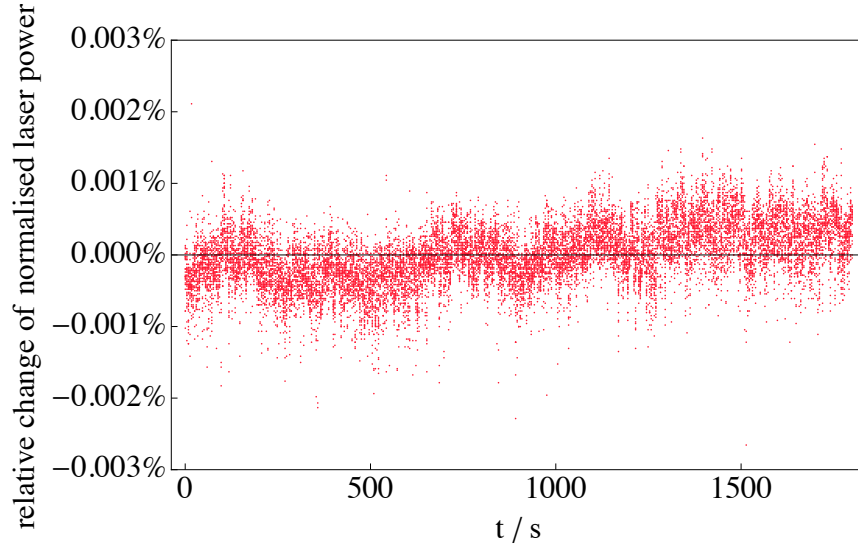


Figure 2.8: Relative change of the laser power of the stabilised laser radiation measured with the out-of-loop-detector and normalised by the signal of out-of-loop-monitor (see Figure 2.5).

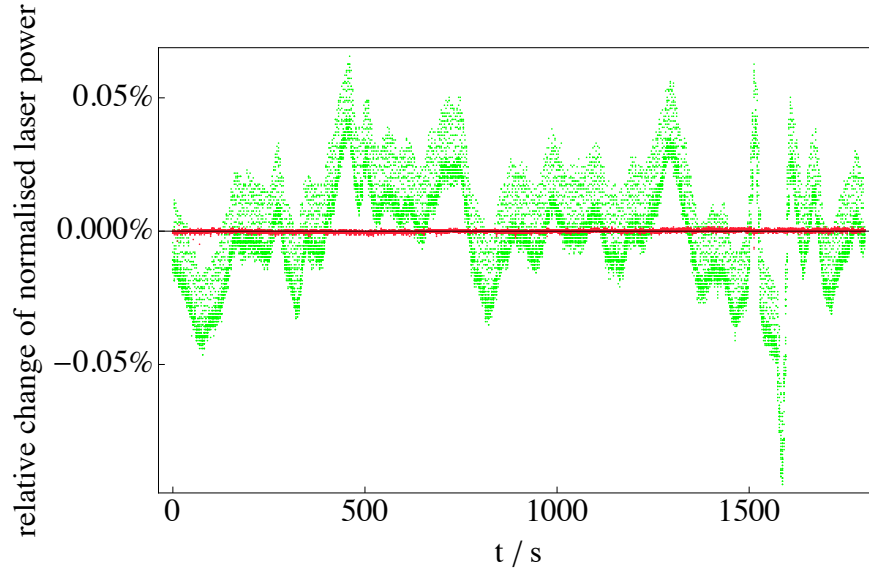


Figure 2.9: Comparison of the relative change of the laser power with external stabilisation (red points) and without external stabilisation (green points). The external stabilisation reduces the noise by a factor of approximately 50.

## 2.3 Improving Cryogenic Radiometry

Cryogenic radiometers are on top of a typical traceability chain in radiometry and photometry. The “detector radiometry” group in the division “7. Temperature and Synchrotron Radiation” of the Physikalisch-Technische Bundesanstalt, where the work for this thesis was done, uses cryogenic radiometers as primary standards for more than 20 years to maintain the spectral radiant power scale from 200 nm to 2000 nm and to calibrate secondary transfer standards.

On the one hand, cryogenic radiometers enable measurements of the spectral radiant power with lowest uncertainties if sufficient radiant power is provided by, for instance, laser sources.

On the other hand, continuously tuneable continuous wave laser radiation is not feasibly available for all wavelengths. Thus, for the calibration of photodetectors in the wavelength range from 400 nm to 1015 nm, a laser based cryogenic radiometer is used, where the spectral responsivity of the devices under test (DUTs) is interpolated in between the laser lines, as described in chapter 2.1.3. The total relative standard uncertainty of the spectral responsivity at the laser lines in the visible and NIR is  $u = 10^{-4}$ .

To validate the PQED as a primary detector standard it is necessary to perform a comparison with another primary detector standard. For an established primary standard, like a cryogenic radiometer, this direct comparison validates the equality of the measurement result of the observed quantity among the other primary standards. For a primary standard which is in development, like the PQED, the direct comparison with an established primary standard is necessary to create input for the design and development of this kind of detector and to give momentum for the acceptance of this new detector. However, the level of uncertainties commonly achieved with cryogenic radiometers is not sufficient to give input for the simulation of the external quantum deficiency and for the validation at the level of uncertainty claimed for the PQED.

In this section the improvements of the new primary detector standard for spectral radiant power of Germany in the wavelength range from 400 nm to 1100 nm, the Cryogenic Radiometer Calibration Facility (CRCF), are described with the aim to significantly reduce the level of uncertainty when calibrating photodetectors down to a level that is necessary for the validation of the PQED. In addition, the uncertainty budget of the CRCF is compiled, which is a prerequisite for the application of this new calibration facility with reduced uncertainties. Furthermore, the uncertainty budget is necessary for a conclusive validation of the PQED and to prove the agreement, of the established cryogenic radiometer and potential primary detector standard PQED, at a high level.

### 2.3.1 Improving the Primary Standard for Radiant Power Measurements of PTB

The Cryogenic Radiometer Calibration Facility (CRCF), a laser based cryogenic radiometer calibration facility (see Figure 2.10), is meant to replace the existing primary detector standard facility, based on a cryogenic radiometer as described in [26], developed more than 20 years ago. The design and efforts made to reduce the uncertainties

from approximately  $10^{-4}$  at the former cryogenic radiometer facility to uncertainties of the order of  $10^{-5}$  at the CRCF are presented below.

### Design of the Cryogenic Radiometer Calibration Facility

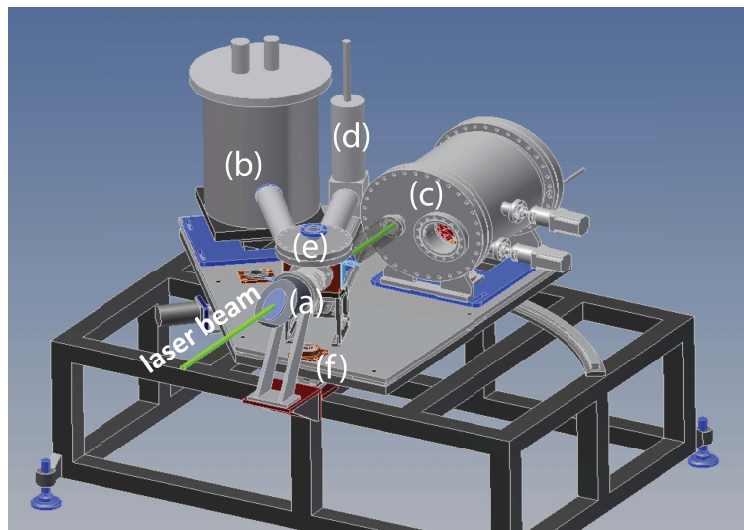
The fundamental design of the CRCF is based on the idea to reduce the uncertainty contribution of the Brewster-window in front of the entrance of the cryogenic radiometer. A CAD picture and a photograph of the CRCF are shown in Figure 2.10. The concept of the CRCF is borrowed from two monochromator-based facilities [59, 60] and a laser-based facility [61]. It has been adopted for the needs of laser-based radiometry at PTB to reach the designated uncertainty of the order of  $10^{-5}$ . Since there are only two remaining manufacturer for cryogenic radiometer, namely the “National Physics Laboratory” (NPL) and “L-1 Standards and Technology, Inc.”, the “CryoRad III” (C3) system from L-1 (New Windsor, Maryland, USA) was chosen. The C3 system allows measurements with a higher sensitivity and lower noise floor than the mechanically cooled NPL system [47] due to the lower operating temperature of down to 2 K.

The laser radiation enters the system via a fixed Brewster-window. The cryogenic radiometer, the detector chamber containing the DUTs, and the spare port are connected to the distribution chamber via CF-vacuum-tubes allowing operation of the whole system in the ultra high vacuum (UHV) regime. These devices are mounted on a movable plate that can be rotated on an axis positioned between the distribution chamber and the fixed Brewster-window (see Figure 2.10(a)) to irradiate the cryogenic radiometer and the DUTs sequentially and at the same position relative to the laser beam.

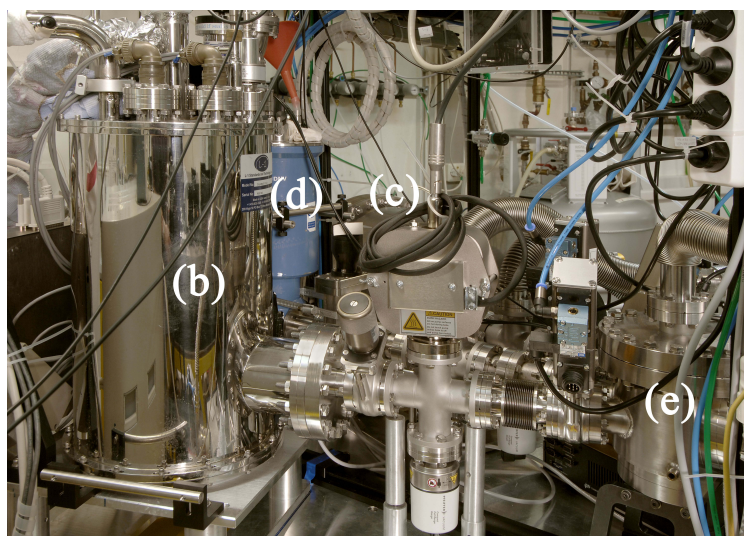
### Measurement Procedure

To calibrate the DUTs, power stabilised lasers are used as radiation sources. The laser radiant power is monitored with a silicon photodiode based three-element trap detector to correct for any change of the radiant power during the measurement. The radiant power is measured with the absolute detector, the cryogenic radiometer, by substituting the radiant power with electrical power (see chapter 2.1.2). An optical shutter is used to determine the heater power of the cryogenic radiometer with ( $P_{\text{rad}}$ ) and without ( $P_{\text{dark}}$ ) optical radiation. The radiant power is then given by:  $P_{\text{laser}} = c_f \cdot (P_{\text{dark}} - P_{\text{rad}})$  with the correction factor  $c_f$  that contains the corrections as described in chapter 2.3.2.

After the radiant power was measured, the system moves the DUTs into the beam and the photocurrent caused by optical radiation is determined from the difference of the photocurrent measured with ( $I_{\text{rad}}$ ) and without optical radiation ( $I_{\text{dark}}$ ) giving:  $I(\lambda, P) = I_{\text{rad}}(\lambda, P) - I_{\text{dark}}$ . This procedure is repeated several times and the spectral responsivity is determined from  $S(\lambda) = c_f \cdot I(\lambda, P)/P_{\text{laser}}$ .



(a)



(b)

Figure 2.10: CAD picture (Figure 2.10(a)) and photograph (Figure 2.10(b)) of the cryogenic radiometer facility set-up in the “detector radiometry” group of PTB. The CAD picture [58] shows the Brewster-window (a), the cryogenic radiometer (b), the detector chamber (c) containing the detectors to be calibrated (DUTs), the cryostat of the “Predictable Quantum Efficient Detector (PQED)” (see chapter 2.1.1) at a spare port (d), the distribution chamber (e) and the bearing (f). The laser radiation enters the setup through the fixed Brewster-window (a) and is then directed onto the cryogenic radiometer and the DUTs by moving the table around the axis (f). The photograph shows the cryogenic radiometer (b), the Predictable Quantum Efficient Detector (d), the detector chamber (c), and the distribution chamber (e).

### 2.3.2 Uncertainty Budget of the Radiant Power Measurement with the CRCF

To be operated as a primary detector standard for spectral radiant power measurements, the CRCF has to be characterised, i.e. the correction factors and operation parameters have to be determined, and an uncertainty budget has to be compiled. The uncertainty budget is mandatory to obtain meaningful results with the CRCF and to document the improvements achieved within this work. Furthermore, the uncertainty budget is a prerequisite for the validation of the PQED with low uncertainties, i.e. to show the agreement between the existing primary standard, the cryogenic radiometer, and the potential primary standard, the PQED, at a high level.

The radiant power outside the cryogenic radiometer can be obtained from the substituted electrical power by applying the correction factor  $c_f$ . The correction factor  $c_f$  is given by

$$c_f = c_{ca} \cdot c_{bw} \cdot c_{sl} \quad (2.7)$$

with  $c_{ca}$  the correction factor for the cavity absorptance,  $c_{bw}$  the correction factor for the Brewster-window transmittance, and  $c_{sl}$  the correction factor for stray light. The contributions to the uncertainty budget of the CRCF when measuring the radiant power behind the last aperture in front of the cavity, like absorptance of the cavity, non-equivalence, noise or the Brewster-window, are discussed below.

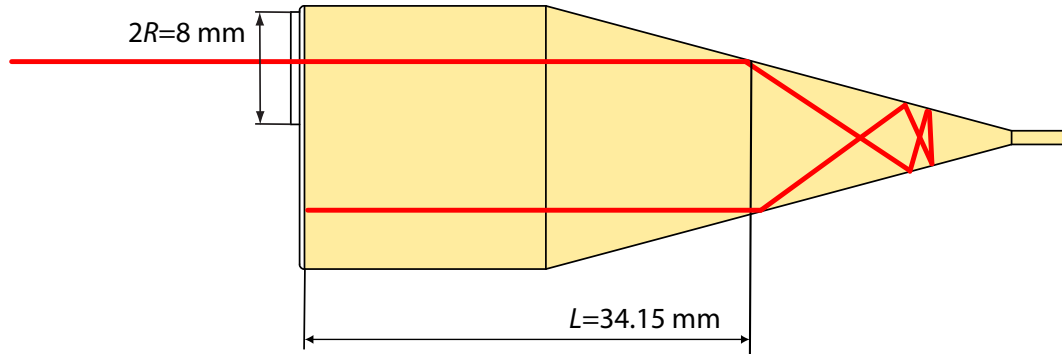


Figure 2.11: Drawing of the cavity and the laser beam path of the new cryogenic radiometer of PTB. The laser beam hits the cavity surface in a distance of  $L = 34.15$  mm from the opening aperture ( $2R = 8$  mm). The overall length of the cavity is 51.41 mm.

#### Cavity Absorptance

The correction  $c_{ca} = a^{-1}$ , associated with the absorptance  $a$  of the cavity, is the most fundamental correction factor and, thus, crucial for the radiant power measurements

## 2 Improving Radiant Power Scales

with a cryogenic radiometer. The absorptance can be measured with an integrating sphere collecting the reflected radiation from inside the cavity. A description of this method can be found in [62]. The cavity of the CRCF-cryogenic radiometer is made of copper with a wall thickness of 0.05 mm with gold plate outside (see Figure 2.12). The inside of the cavity is painted with Chemglaze Z302. The path of light inside the

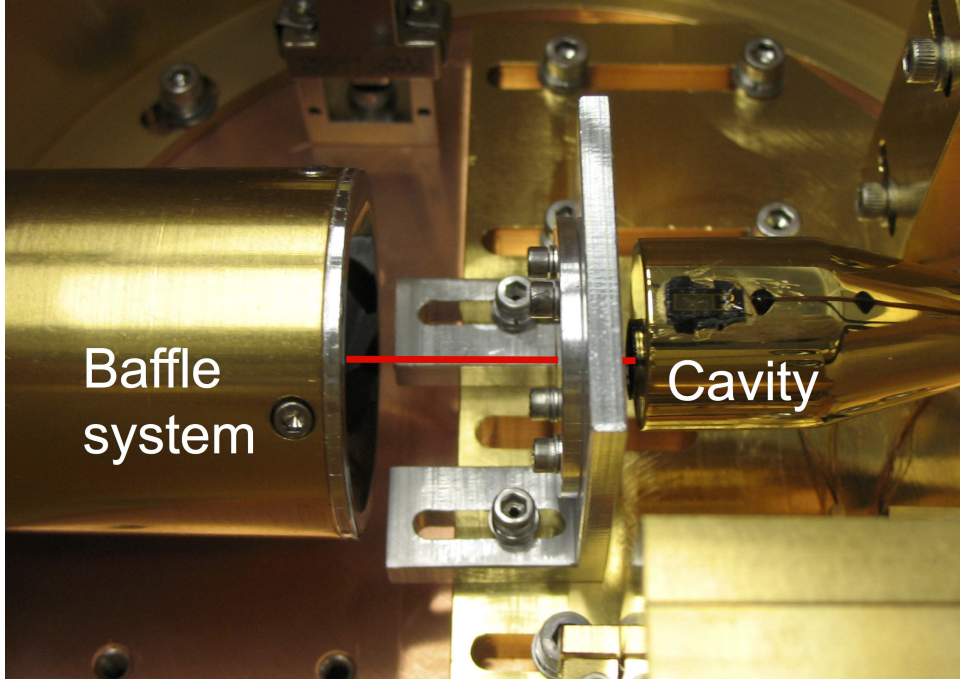


Figure 2.12: Picture of the inside of the new cryogenic radiometer of PTB. The cavity of the cryogenic radiometer of the CRCF is irradiated with laser radiation (red line) through a set of baffles inside the pipe to suppress stray light and thermal radiation detectable with the cavity.

cavity is shown in Figure 2.11. The radiation is specular reflected 13 times inside the cavity and, hence, the specular reflection losses can be neglected. Thus, the exiting radiation, caused by the absorptance of the cavity smaller than unity, is dominated by the diffuse reflected radiation inside the cavity. The absorptance of the cavity has been measured by the manufacturer to be  $a = 0.999975$  with a relative standard uncertainty of  $1.23 \cdot 10^{-6}$  [63].

When the CRCF will replace the former facility as a primary detector standard, the absorptance of the cavity needs to be validated traceable to the SI. However, it was not possible to perform this validation within the framework of this thesis. To theoretically estimate the order of magnitude of the absorptance  $a$  of the cavity an approximation [26] was used here:

$$a \approx \varrho_w \cos \theta R^2 / (R^2 + L^2) \quad (2.8)$$

with  $\theta$  the angle of incidence of the beam at the rear wall,  $\varrho_w$  the hemispherical diffuse reflectance of the wall,  $L$  the distance along the cavity axis from the entrance aperture to rear wall, and  $R$  the radius of the entrance aperture. The values used for the calculation are:  $\varrho_w = 0.008$  [64],  $\theta = 75^\circ$ ,  $L = 34.15$  mm and  $R = 4$  mm (see Figure 2.11). This approximation yields an absorptance of the cavity of 0.999972 which is in good agreement with the result 0.999975 of the measurement performed by the manufacturer. Nevertheless, this value will be measured at a later time as a part of the validation process of the new cryogenic radiometer. The uncertainty of the absorptance  $a$  is estimated to 50% of the reflection losses measured by the manufacturer, i.e.  $u(c_{ca}) = 13$  ppm.

### Non-Equivalence

The non-equivalence of a cryogenic radiometer is the difference in optical and electrical heating of the cavity. At low temperatures, the thermal diffusivity increases while the specific heat capacity decreases [65], i.e. there is practically no temperature gradient on the cavity. This leads to an almost perfect equivalence of electrical and optical heating of the detector even if the heater is at a different position than where the absorption takes place. The standard heater is located at the position where the radiation hits the cavity wall for the first time and most of radiant power is transferred into heat. An additional heater is placed close to the entrance of the cavity and, thus, further away from the position where the radiation is absorbed. Hence, the difference between electrical and optical heating during a radiant power measurement is always smaller than the measured non-equivalence between standard and additional heater. The use of superconducting leads to the heating element insures that all the heat is generated in the heater. The non-equivalence of the cavity of the CRCF cryogenic radiometer was determined by comparing the heating power necessary to maintain a certain temperature with the standard heater and with the additional heater. The results of this comparison can be found in Table 2.1 and show no detectable non-equivalence.

Heater power	Non-equivalence	$u$
350 $\mu$ W	0.0012%	0.0003%
350 $\mu$ W	-0.0011%	0.0004%
350 $\mu$ W	0.0006%	0.0004%
750 $\mu$ W	0.0000%	0.0003%
750 $\mu$ W	-0.0005%	0.0003%
750 $\mu$ W	0.0000%	0.0003%
mean = 0.0000%		$u_{\text{mean}} = 0.00036\%$

Table 2.1: The relative difference of the heater power of the regular heater and of the additional heater at a different position and the standard uncertainty of this difference. The measurements were performed at a heater power of 350  $\mu$ W and 750  $\mu$ W.

### Brewster-window and Stray Light

The operation of the cryogenic radiometer at temperatures of about 5 K enforces the employment of an entrance window in front of the cryogenic radiometer. This window could introduce interferences when the wavelength of the laser radiation slightly changes or could transmit a weakened and spatially shifted image of the laser beam. These unwanted effects can be drastically reduced by the proper use of Brewster-angled windows reducing the reflectance for p-polarised radiation by several orders of magnitude down to below 0.0003 in the visible. When the concept of the CRCF was developed the main focus was put on the avoidance of this source of uncertainty, i.e. the uncertainty associated to the correction factor  $c_{bw}$ , by making measurements of the Brewster window unnecessary. The cryogenic radiometer measures the laser power and afterwards the DUTs, in the so-called detector chamber, are moved to the position of the cryogenic radiometer and the photocurrent is measured at exactly ( $\pm 20 \mu\text{m}$ ) the same position and behind the same Brewster-window. Thus, for calibrations at the CRCF the transmittance of the Brewster-window does not need to be measured. Furthermore, there is no contribution of the change of the transmittance of the Brewster-window to the uncertainty budget, since any changes of window transmission are observed by the cryogenic radiometer and the DUTs in the same way. Thus, the influence of the transmittance of the Brewster-window of the CRCF does not need to be corrected, i.e.  $c_{bw} = 1$  with  $u(c_{bw}) = 0$ .

Stray light is introduced at each optical component of the setup with an unknown intensity distribution. If the cryogenic radiometer and the DUT are affected by different parts of the stray light, the calibration result can be heavily compromised. The uncertainty contribution of the stray light becomes a dominant contribution to the uncertainty budget if the sensitive areas of cryogenic radiometer and DUT are different and both devices are irradiated at different positions in the beam path. However, the influence of stray light on the calibration result can be corrected. This is possible with low uncertainties when the cryogenic radiometer and the DUT are irradiated at the same position in the beam path but have different sensitive areas and more difficult, with higher uncertainties, if the cryogenic radiometer and the DUT are measuring at different positions in the beam path. If the measurements of the cryogenic radiometer and of the DUT are performed at the same position, and with the same aperture defining the measured beam area, the influence of stray light can be neglected. This condition is nearly fulfilled at this setup as the cryogenic radiometer and the DUT measure at the same position and have similar apertures to define an almost identical acceptance of the stray light. At the CRCF the apertures of all detectors and of the cryogenic radiometer are set to 7 mm. To estimate the uncertainty contribution of the stray light, a special detector was developed (see Figure 2.28). This device, the uncertainty contribution of the stray light, and the associated correction for the experimental validation of the PQED is described in detail in chapter 2.4.2. Finally, this uncertainty contribution depends on the current experimental condition, hence, no uncertainty contribution of the stray light is given in Table 2.2.

### Heater Power Measurement

The heater power of the cryogenic radiometer is measured with two Agilent 3458A digital multimeter (DMM). One DMM measures the heater voltage  $V_{\text{heater}}$ , i.e. the voltage drop over the heater, while the other DMM measures the voltage drop  $V_{\text{sense}}$  over an external resistance  $R_{\text{sense}}$  connected in series in order to determine the heater current given by

$$I_{\text{heater}} = \frac{V_{\text{sense}}}{R_{\text{sense}}} . \quad (2.9)$$

This setup simplifies the traceability of the heater power measurement to the SI. The heater power is then given by

$$P_{\text{laser}} = \frac{V_{\text{heater}} \cdot V_{\text{sense}}}{R_{\text{sense}}} . \quad (2.10)$$

However, the measured heater power is flawed with noise from several independent

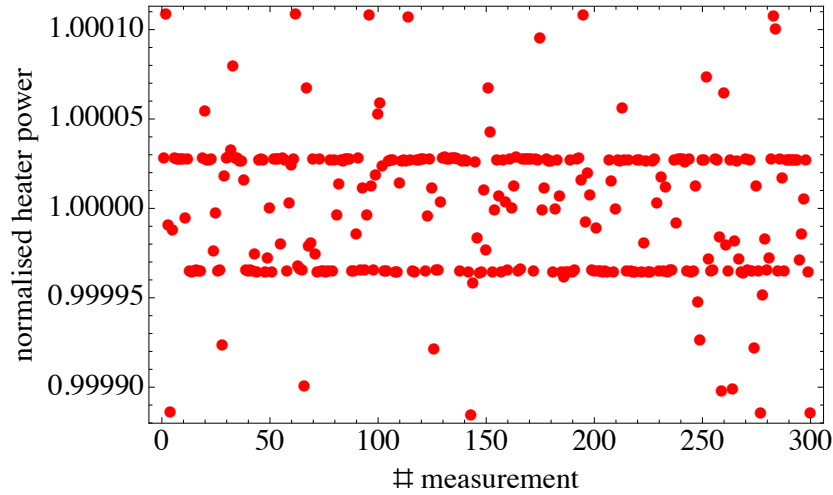


Figure 2.13: Normalised heating power of the CRCF-cryogenic radiometer measured without laser radiation. The relative standard deviation of the heating power is  $u_{\text{hp}} = 2.23 \cdot 10^{-6}$ .

sources. The thermal radiation entering the cavity contributes to the measured noise and can introduce a drift of the detected radiant power. The amount of thermal radiation entering the cavity can be controlled by a suitable field of view for the certain application. In an electrical power measurement with the cryogenic radiometer, the electrical noise (“white noise”) of the temperature controller is always present and can be reduced by proper grounding and careful electrical circuit design. Furthermore, in a spectral radiant power measurement, also the noise from the non-perfect laser power stabilisation

## 2 Improving Radiant Power Scales

contributes to the detected noise as described in chapter 2.4.2. Hence, the standard deviation of the detected heater power was measured without laser radiation. Figure 2.13 shows the measured noise of an electrical heating power measurement without laser radiation, i.e. the dark signal of the cryogenic radiometer. The high resolution of the DMMs (8.5 digits) in combination with the 12 bit resolution of the temperature controller lead to the visibility of the discrete steps in the heating power as can be seen in Figure 2.13. The noise floor at a receiver power level of  $350 \mu\text{W}$  is  $0.78 \text{ nW}$ , i.e. the relative standard uncertainty of the heater power measurement of the CRCF-cryogenic radiometer is  $u_{\text{hp}} = 2.25 \cdot 10^{-6}$ . To determine this uncertainty, the correlation between the two voltage measurements, that are both caused by the same current, was taken into account. The uncertainty contributions of the heater power measurement in Table 2.2 resembles the typical experimental uncertainty that includes the contributions described before.

### Uncertainty Budget

The uncertainty contributions of the CRCF-cryogenic radiometer are presented in Table 2.2. The combined relative standard uncertainty of the CRCF radiant power measurements is  $u(P(\lambda)) = 18.6 \text{ ppm}$ . Thus, the uncertainty of radiant measurements has been reduced by a factor of approximately three as compared to the cryogenic radiometer the CRCF has replaced. The most dominant contributions to the uncertainty budget are the cavity absorptance and the heater power measurement.

Source of uncertainty	Value of RTCR / ppm	Value of CRCF / ppm
Brewster-window $c_{\text{bw}}$	30	0
Non-equivalence	20	3.6
Cavity absorptance $c_{\text{ca}}$	30	13
Heater power noise	14	2.25
Thermal drift	20	3.8
Heater power measurement	10	10
Combined standard uncertainty	<b>53.9 ppm</b>	<b>18.6 ppm</b>

Table 2.2: Uncertainty budget of the radiant power measurement for the CRCF and it's predecessor RTCR without uncertainty contributions from the DUTs. The uncertainty budget of the RTCR was taken from [66], The instrumental uncertainties are stated for a calibration of the DMMs not longer than 90 days before usage.

## 2.4 Improving Detectors with Predictable Quantum Efficiency

The Predictable Quantum Efficient Detector (PQED) is the main objective of the “Candela” project. It combines both approaches to detectors with predictable quantum efficiency, i.e. the modelling method [17, 32] and the self calibration method [29, 30], to reach a predictability of the external quantum efficiency of the PQED with an uncertainty of less than 100 ppm. The PQED is based on the set of methods to reduce and to determine the quantum deficiency of inversion layer silicon photodiodes [9] proposed by Geist et al. [31]. It has been shown before that inversion layer photodiodes can reach almost 100% internal quantum efficiency [67, 68] and in trap configuration even an external quantum efficiency of almost 100% [69]. Additionally, it has been shown that high accuracy modelling of the photon-to-electron conversion of this type of photodiode is possible [32] by solving the drift-diffusions equations of the photodiodes in one dimension. The developments within the framework of the PQED are supposed to eventually enable the prediction of the spectral responsivity with an uncertainty of about 1 ppm. Thus, the PQED is the most important development in the field of detector based radiometry since the introduction of cryogenic radiometer in the 1980s. A working PQED will enable National Metrology Institutes that don't have cryogenic radiometer to perform absolute measurements of radiant power in the visible wavelength range with uncertainties commonly achieved with cryogenic radiometers. A detailed description of inversion layer photodiodes and the PQED is given below.

### 2.4.1 Modelling the PQED

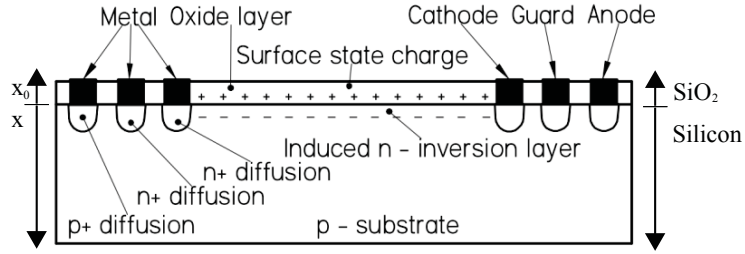
In this section the photodiodes - that make up the PQED - and the modelling of the reflectance and internal losses of the PQED, i.e. the prediction of the response of the PQED to optical radiation, is described.

#### Inversion Layer Photodiodes

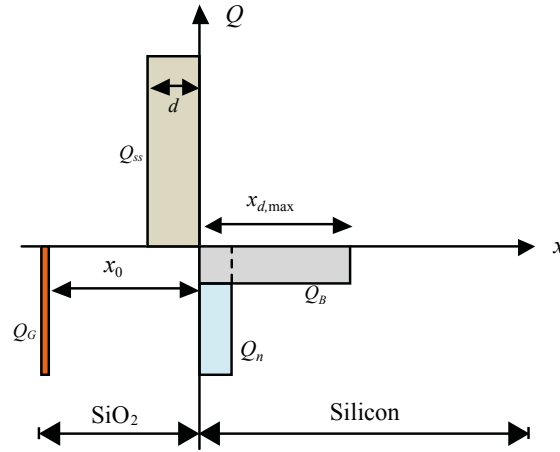
In this type of photodiodes, the natural inversion layer occurring in thermally oxidised p-type silicon is exploited to create an n-p-junction [9]. The photodiodes are made from a p-type substrate with very low impurity concentration. The photodiode is created by thermally growing a silicon dioxide layer with a highly predictable and fixed amount of positive surface charges  $Q_{ss}$  on top of the bulk silicon wafer (see Figure 2.14(a)). These surface charges induce an n-type inversion layer and an n-p-junction is formed if the induced charge density  $Q_n$  is negative as described by Hansen [9], i.e.  $Q_n < 0$ :

$$Q_n = -Q_{ss} \left( 1 - \frac{d}{2x_0} \right) - Q_B \left( 1 + \frac{\epsilon_{0x} x_{d,max}}{2\epsilon_s x_0} \right). \quad (2.11)$$

Here  $x_{d,max}$  is the width of the depletion layer,  $x_0$  is the width of the SiO<sub>2</sub>-oxide layer,  $d$  is the width of the surface charge layer,  $Q_B$  is the negative depletion charge, and the parameters  $\epsilon_{0x}$  and  $\epsilon_s$  are the permittivity for the silicon dioxide, and the silicon respectively. Figure 2.14(b) shows the charge distribution of inversion layer photodiodes. From



(a)



(b)

Figure 2.14: Cross section (Figure 2.14(a)) and charge density distribution (Figure 2.14(b)) of induced junction photodiodes that are used in the PQED (see text and [70, 71]). The charges are:  $Q_{ss}$  positive surface charge,  $Q_B$  negative depletion charge,  $Q_n$  the inversion layer charge in the silicon and the mirror charge  $Q_G$ .

(2.11) it is obvious that reducing the thickness of the silicon dioxide layer  $x_0$  will decrease the electron concentration  $Q_n$ , and, additionally, that this concentration strongly depends on  $Q_{ss}$ . Figure 2.15 shows the calculated induced charge density as a function of surface charge density for different SiO<sub>2</sub>-oxide thicknesses. To fulfil the photodiode

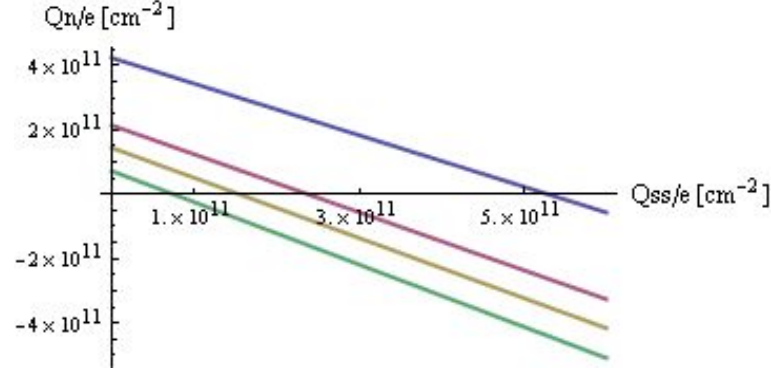


Figure 2.15: Induced charge  $Q_n$  as a function of surface charge  $Q_{ss}$  for different SiO<sub>2</sub>-oxide thicknesses (figure taken from [72]). The blue line indicates the calculation for a SiO<sub>2</sub>-oxide thickness of 50 nm, the red line for 100 nm, the yellow line for 150 nm and the green line for 310 nm. All calculations were made for an applied bias voltage of 0 V, a doping density  $N_A = 2 \cdot 10^{12} \text{ cm}^{-3}$  and a temperature of 78 K. To have a working photodiode,  $Q_n$  has to be negative.

requirement, several methods can be applied to the silicon wafer during the manufacturing process. The number of induced surface state charges  $Q_{ss}$  is highly predictable and can be controlled to satisfy  $Q_n < 0$  by, e.g., the annealing conditions [73] or by applying a strong electric field to the photodiodes [73].

Two batches of photodiodes have been produced within the “Candela” project by the Technical Research Centre of Finland (VTT) on 525  $\mu\text{m}$  thick silicon wafers with a boron doping density of  $2 \cdot 10^{12} \text{ cm}^{-3}$  (6.6 k $\Omega \text{ cm}$  resistivity, as specified by the wafer manufacturer). In the first batch, the photodiodes had a SiO<sub>2</sub>-oxide thickness of 100 nm and 310 nm. In the second batch, photodiodes were produced with a SiO<sub>2</sub>-oxide thickness of 220 nm and 300 nm by applying an improved production procedure. The electro-optical characterisation of the first batch photodiodes revealed some disappointing qualities. It became obvious that the number of induced surface charges was not sufficient for the 100 nm SiO<sub>2</sub>-oxide layer photodiodes due to a deficient production procedure in the first processing round. Figure 2.16 shows, as an example, the measured uniformity of the relative spectral responsivity (see chapter 2.4.2) of two first batch photodiodes. Furthermore, the first batch photodiodes with a SiO<sub>2</sub> oxide layer thickness of 300 nm showed a supra-linearity [74] at a wavelength of 760 nm. Supra-linearity in the NIR is commonly explained with the existence of recombination channels [75] and, thus, a non-unity internal quantum efficiency. According to the manufacturer between  $2 \cdot 10^{11} \text{ e/cm}^2$  and  $4 \cdot 10^{11} \text{ e/cm}^2$  SiO<sub>2</sub>-oxide surface charges were induced and, as it can be seen from

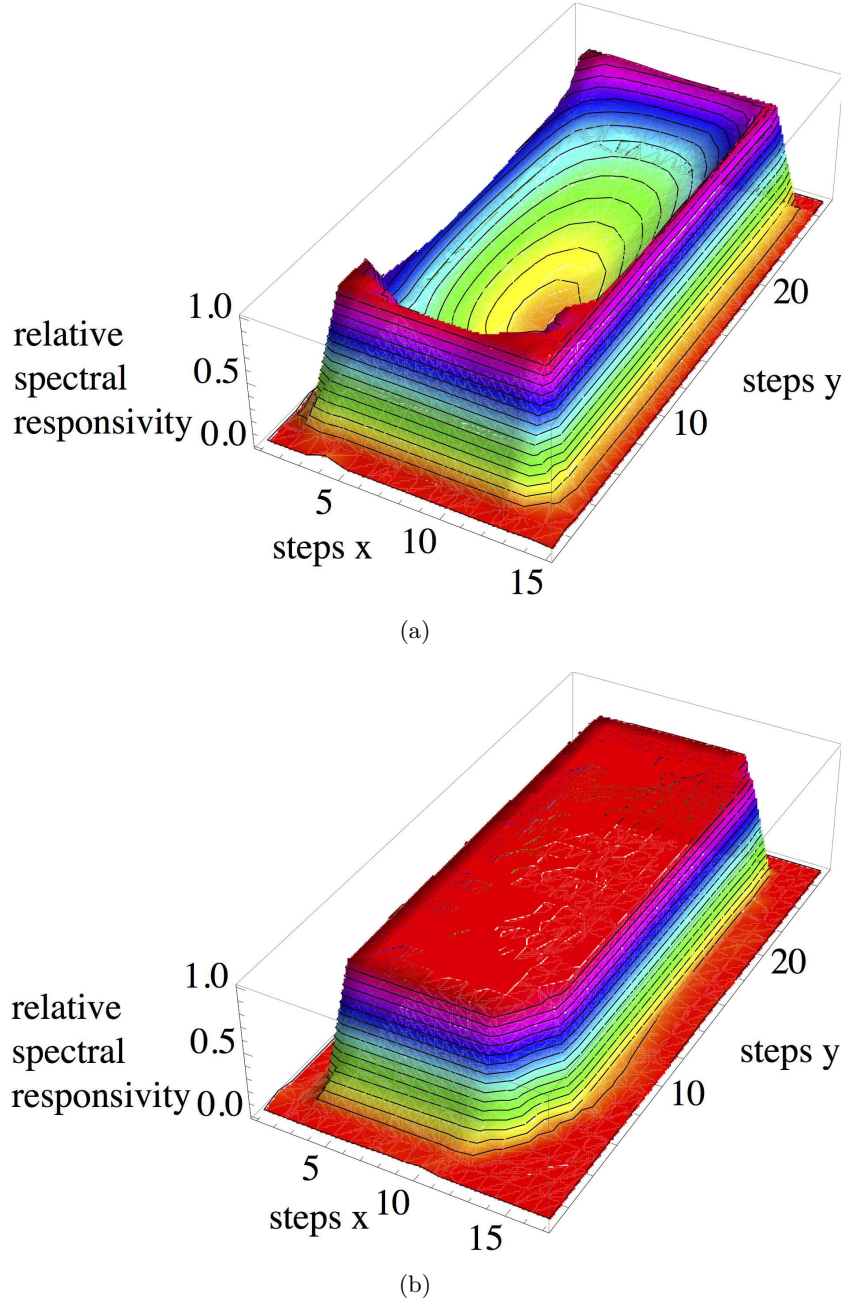


Figure 2.16: Relative spectral responsivity of first batch photodiodes with an SiO<sub>2</sub>-oxide thickness of 100 nm (Figure 2.16(a)) and 300 nm (Figure 2.16(b)). The induced surface charges between  $2 \cdot 10^{11} e/cm^2$  and  $4 \cdot 10^{11} e/cm^2$  were not sufficient to create a working photodiode in the case of a SiO<sub>2</sub>-oxide thickness of 100 nm which results in a highly non-uniform relative spectral responsivity while the photodiode with a SiO<sub>2</sub>-oxide thickness of 300 nm shows a uniform relative spectral responsivity. The relative spectral responsivity was measured with the setup described in chapter 2.4.2.

Figure 2.15, this is not sufficient to create an inversion layer in the case of 100 nm SiO<sub>2</sub>-oxide thickness photodiodes. As a consequence of these results, the second batch photodiodes were produced with SiO<sub>2</sub> oxide layer thicknesses of 300 nm and of 200 nm to replace the 100 nm SiO<sub>2</sub>-oxide layer photodiodes. Moreover, the characterisation results of the first batch photodiodes strongly supported the position of PTB to add a back-electrode to a fraction of 50% of the photodiodes to possibly reduce recombination losses at wavelengths above 600 nm. However, the back electrode was not connected to the external measurement circuit used for the validation PQED (see chapter 2.4.2) and, thus, the influence of the back electrode on the internal quantum deficiency has not been determined yet. The second batch photodiodes reached a higher surface charge density of  $6.2 \cdot 10^{11} e/cm^2$  due to the improved production procedure. The electro-optical characterisation of the second batch photodiodes is described below in chapter 2.4.2.

### Design of the Predictable Quantum Efficient Detector

To reach almost 100% external quantum efficiency, the reflectance and internal losses have to be as small as possible (see also (2.12)), i.e. two requirements have to be fulfilled:

- Reflectance losses have to be reduced by, e.g., a light trap design based on multiple reflections.
- The internal quantum deficiency has to be close to zero. The internal quantum deficiency of photodiodes can be reduced applying a reverse bias voltage which extends the depletion layer and, thus, reduces the fraction of photons that are absorbed behind the depletion layer.

The reflectance of several possible PQED-designs has been calculated in [76]. In the final PQED, two photodiodes are arranged in a special “wedge” design (see Figure 2.17). The reflectance losses of this design can be below 1 ppm for certain combinations of photodiodes with different SiO<sub>2</sub>-oxide thicknesses and 13 reflections inside the PQED [76]. The actual PQED has a design as shown in Figure 2.17 with the upper photodiode, hit first by radiation, having a SiO<sub>2</sub>-oxide thickness of 210 nm and the lower photodiode, hit second by radiation, having a SiO<sub>2</sub>-oxide thickness of 300 nm. The dimensions of the photodiodes (see Figure 2.18) are  $11 \times 22 \text{ mm}^2$  and the resulting reflectance is below 50 ppm for wavelengths above 450 nm (see below).

### Modelling of the External Quantum Deficiency of the PQED

To predict the spectral responsivity of a photodetector, the optical losses caused by reflection at the photodiode surface and incomplete absorption inside the photodiode as well as the internal quantum deficiency have to be taken into account (see also [18]). The internal quantum deficiency of the PQED has been predicted within the “Candela” project by the partners Justervesenet and Metrosert [17]. The reflectance has been measured and an uncertainty budget for the reflectance has been compiled by the “Candela” partner MIKES [18]. However, the predicted spectral responsivity is wavelength dependent. To simplify the presentation of the prediction of the spectral responsivity of the

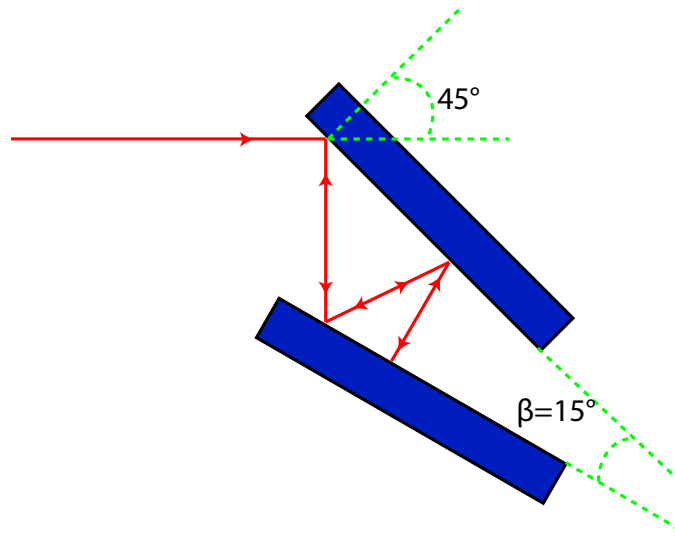


Figure 2.17: The structure of the PQED with two photodiodes in a “wedge” configuration yielding seven reflections [76]. The angle  $\beta$  between the photodiodes is set to  $15^\circ$ . The first photodiode is irradiated at an angle of incidence of  $45^\circ$ .

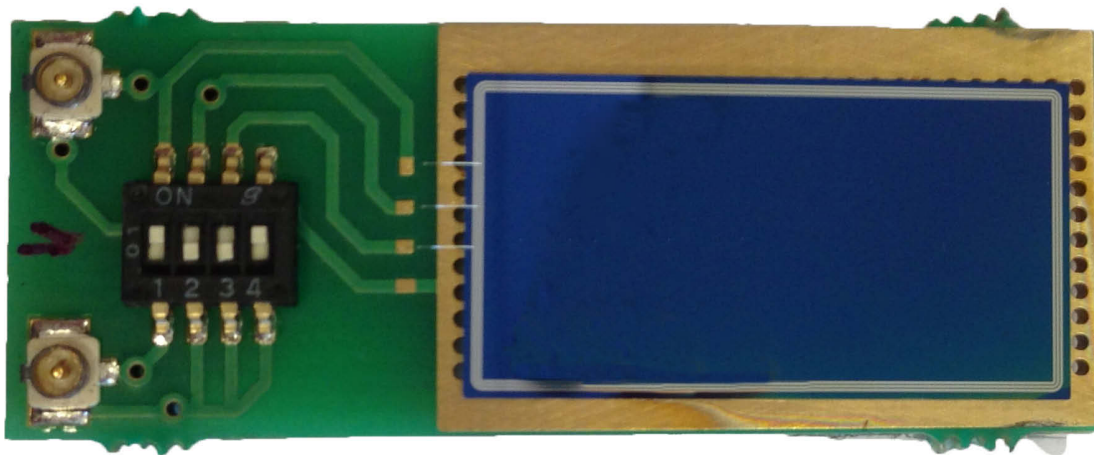


Figure 2.18: Custom made induced junction photodiode on a printed circuit board to be incorporated into a Predictable Quantum Efficient Detector.

PQED the external quantum deficiency  $\Delta$  was calculated to obtain a figure of merit which only varies slowly with the wavelength.

The predicted external quantum deficiency  $\Delta_p$  of the PQED is obtained from the relation:

$$\Delta_p = 1 - (1 - r_{\text{PQED}}(\lambda))(1 - iQD(\lambda)) \approx r_{\text{PQED}}(\lambda) + iQD(\lambda) \quad (2.12)$$

with  $r_{\text{PQED}}(\lambda)$  the reflectance of the PQED and  $iQD(\lambda)$  the calculated internal quantum deficiency of the PQED.

For the work presented here the reflectance of the PQED was calculated by matrix based method. This method can be used to calculate the reflectance for an arbitrary set of thin dielectric layers (see for instance [77]). The results obtained with this method are within the uncertainty of the calculation determined in [18] identical with the results obtained by MIKES. The reflectance  $r_{\text{PQED}}$  of the PQED, taking into account an additional water or ice layer on top of the photodiodes, is given by:

$$r_{\text{PQED}} = \frac{r_{12}e^{2i(\beta_1+\beta_2)} + e^{2i\beta_1}r_{12}r_{23}r_{34} + e^{2i\beta_2}r_{23} + r_{34}}{e^{2i(\beta_1+\beta_2)} + e^{2i\beta_1}r_{23}r_{34} + e^{2i\beta_2}r_{12}r_{23} + r_{12}r_{34}} \quad (2.13)$$

with  $r_{12}$  the fresnel reflection coefficient for the interface air-H<sub>2</sub>O,  $r_{23}$  the fresnel reflection coefficient for the interface H<sub>2</sub>O-SiO<sub>2</sub>,  $r_{34}$  the fresnel reflection coefficient for the interface SiO<sub>2</sub>-Si, and  $\beta_{1,2} = 2\pi/\lambda \cdot d_{1,2} \cdot n_{\text{H}_2\text{O},\text{SiO}_2} \cdot \cos \alpha_{1,2}$  describing the phase shift and propagation in the H<sub>2</sub>O and SiO<sub>2</sub>-layer. The parameters entering  $\beta$  are:  $\lambda$  the wavelength of the radiation,  $d_{1,2}$  the thickness of the H<sub>2</sub>O and SiO<sub>2</sub>-layer,  $n_{\text{H}_2\text{O},\text{SiO}_2}$  the refractive index of the H<sub>2</sub>O and SiO<sub>2</sub>-layer and  $\alpha_{1,2}$  the propagation angle in the H<sub>2</sub>O and SiO<sub>2</sub>-layer. Figure 2.19 shows the calculated reflectance of the PQED for a configuration as described above. The optical parameters for Si were taken from [78], the optical parameters for SiO<sub>2</sub> were taken from [79] and [80]. The optical parameters for water ice that may occur on the photodiode surface when the PQED is operated at the temperature of liquid nitrogen (see below) were taken from [81]. The source of the water ice can be a leakage in the cryostat or water that is desorbed from the cryostat walls. The refractive index of the air is assumed to be unity as the PQED is operated under vacuum. However, there are no optical parameters for these materials available that have been obtained traceable to the SI and that state uncertainties. The parameter for the reflectance calculations shown in Figure 2.19 were:

- SiO<sub>2</sub>-layer thickness of the upper photodiode: 301.4 nm (hit first by radiation)
- SiO<sub>2</sub>-layer thickness of the lower photodiode: 220.5 nm (hit second by radiation)
- Angle between the upper and lower photodiode: 15°
- Angle of incidence upper photodiode hit by radiation: 45°
- Number of reflections inside the trap: 7
- Polarisation state of radiation: p-polarised
- Temperature: 298 K

## 2 Improving Radiant Power Scales

- Water or ice on the surface of the photodiodes: no

The optical losses of the PQED operated at room temperature are below 50 ppm for wavelengths larger than 450 nm. If the PQED is operated at the temperature of liquid nitrogen (77 K) the reflectance losses are about 10 ppm higher than those at room temperature. In addition, the optical parameters, especially the absorption coefficient of silicon, are flawed with higher uncertainties determined from the difference of values in [82, 83, 84]. For cryogenic temperatures, the reflectance of the PQED increases by 7 ppm at 532 nm and by 10 ppm at 760 nm. Furthermore, a growing water ice layer may occur on the PQED photodiodes that changes the reflectance. This reflectance change is dependent on the wavelength of the radiation and the growth rate of the ice layer. The reflectance change can reach values up to 50 ppm, caused by icing, at a wavelength of 760 nm, for ice layer thicknesses between 100 nm and 200 nm (see Figure 2.20). This has to be taken into account for future applications of the PQED and for the construction of new PQED-cryostats. To achieve the desired ultra low uncertainty of the PQED the vacuum quality has to be better than  $10^{-8}$  mbar to avoid ice growing on the surface of the photodiodes. However, during the validation measurements measurements of the PQED at CRCF no temporal oscillation of the measured spectral responsivity of the PQED was observed. The expanded uncertainty ( $k=2$ ) of the calculated PQED reflectance has been determined by the “Candela” partner MIKES [18] to be 4 ppm at a wavelength of 532 nm and 15 ppm at a wavelength of 760 nm at room temperature (see Table 2.3). The term expanded uncertainty  $k = 2$  means that the standard uncertainty multiplied with the coverage factor  $k = 2$  is stated. It has been determined in accordance with the “Guide to the Expression of Uncertainty (GUM)”. The value of the measurand then

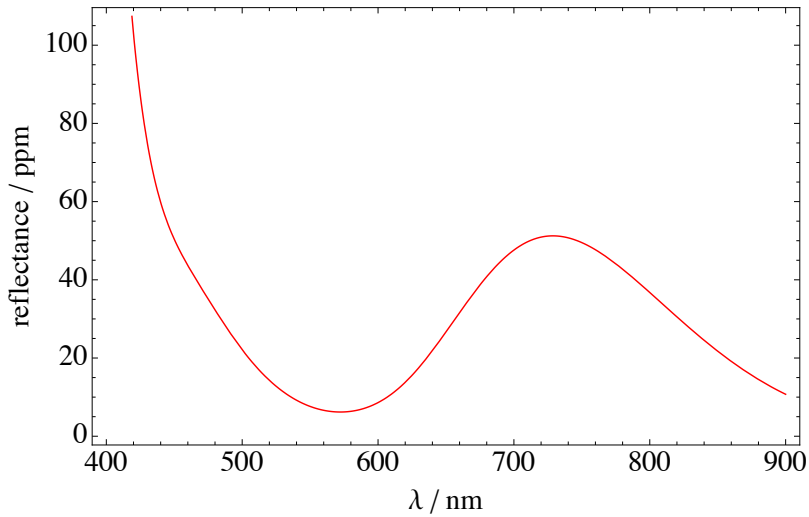
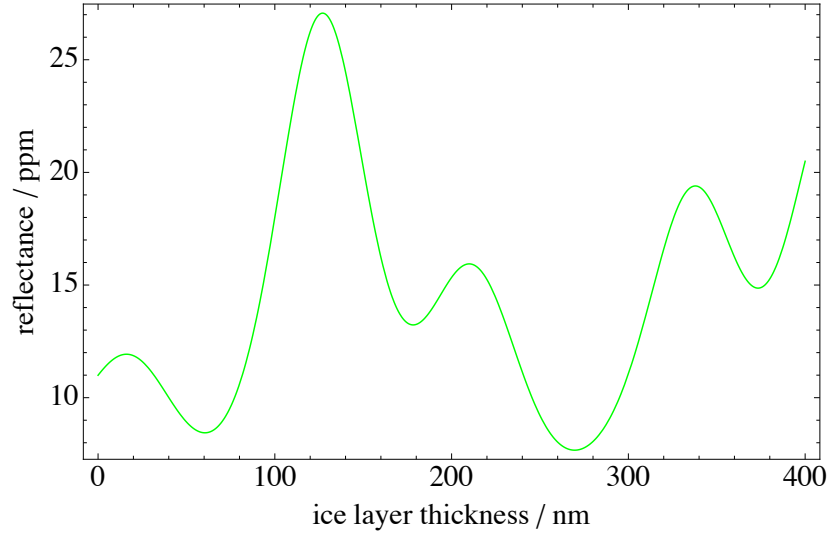
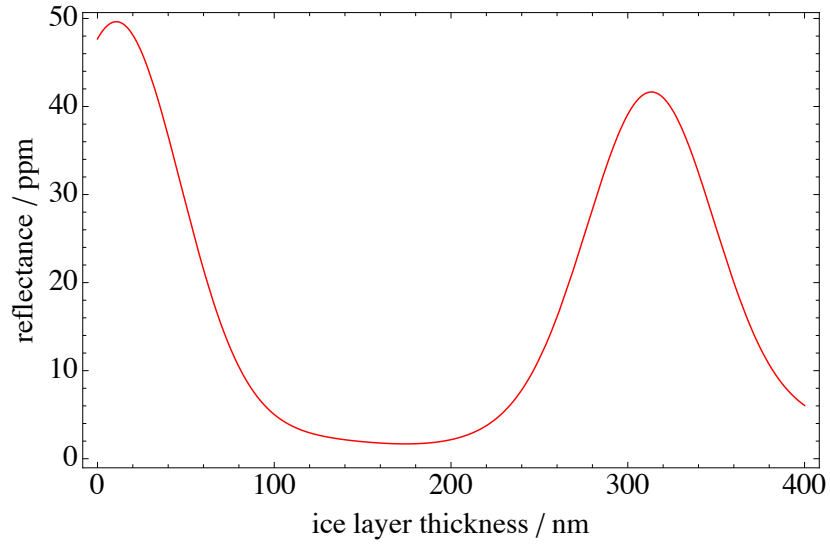


Figure 2.19: Calculated reflectance of the PQED operated at room temperature for p-polarised radiation.



(a)



(b)

Figure 2.20: Calculated reflectance of the PQED at a temperature of 77 K plotted over the ice layer thickness for wavelengths of 532 nm (Figure 2.20(a)) and 760 nm (Figure 2.20(b)). The reflectance was calculated according to (2.13). The change of reflectance due to ice growth contributes to the uncertainty budget of the PQED at 77 K because the possibility of ice growth cannot be counted out with the present cryostats.

normally lies, with a probability of approximately 95%, within the attributed coverage interval.

At the temperature of liquid nitrogen, the uncertainty of the calculated reflectance increases to 10 ppm at a wavelength of 532 nm and 35 ppm at a wavelength of 760 nm. This increased uncertainty is caused by the higher uncertainty of the values of the optical parameters used for the calculation and the influence of the possible ice layer on the photodiode surface on the calculated reflectance. The internal losses, i.e. the internal quantum deficiencies, have been calculated in [17]. For this purpose the one dimensional software “PC1D” [85] has been used. This software is able to solve the drift-diffusion-equations in a semiconductor in one dimension with high accuracy [32]. The parameters that entered into the simulation and how they have been obtained is also described in [17]. To determine the reliability of this modelling method, the results have been compared with a three-dimensional software that has been provided by VTT, the manufacturer of the PQED photodiodes. This comparison shows up to a factor of 10 higher internal quantum deficiencies than PC1D. However, the three-dimensional software was not available within the “Candela” project. The uncertainty of the simulation with PC1D is multiplied with a constant factor of 10 [17] as upper uncertainty boundary to take into account the comparison with the three-dimensional software. Even though the simple one dimensional software is not quantitatively correct, it is capable of explaining the changes in the internal quantum deficiency with wavelength, reverse bias voltage and temperature at longer wavelengths. At a temperature of 78 K, 5 V reverse bias voltage and for a wavelength of 760 nm, the uncertainty of the prediction of the internal quantum deficiency is increased as compared to the other predicted conditions. Under this conditions, a fraction of the radiation penetrates beyond the depletion layer. The charge carriers that are created there, are not driven by an electric field and, thus, move slower due to diffusion and are more likely trapped by recombination centres. This issue can be resolved by the application of a higher bias voltage that extends the depletion layer deeper into the bulk volume of the photodiode (see Table 2.3 and Figure 2.27).

The predicted external quantum deficiency of the PQED,  $\Delta_p$ , for the comparison conditions at the new cryogenic radiometer facility of PTB (see chapter 2.3.1) is given in Table 2.3.

### 2.4.2 Validating the Predictable Quantum Efficient Detector

To validate the characteristics of the assembled PQED, single induced junction photodiodes, as they are applied in the PQED, have been tested in terms of uniformity and linearity of the spectral responsivity. The dependence of these properties on the applied bias voltage was also tested. Finally, the prediction of the spectral responsivity of the PQED was validated by measuring the external quantum deficiency of the PQED obtained at the new cryogenic radiometer of PTB and comparing this experimental result with the predicted external quantum deficiency  $\Delta_p$  (see (2.12)).

$\lambda$ / nm	T / K	$U_{\text{bias}}$	$r_{\text{PQED}}$ / ppm	$iQD(\lambda)$ / ppm	$\Delta_p$ / ppm
532	298	5	$11 \pm 4$	$7_{-2}^{+144}$	$18_{-5}^{+144}$
532	78	5	$18 \pm 10$	$1 \pm 2$	$19 \pm 10$
760	298	5	$48 \pm 15$	$6_{-2}^{+128}$	$54_{-15}^{+128}$
760	78	5	$58 \pm 35$	$28_{-6}^{+688}$	$86_{-36}^{+689}$
760	78	20	$58 \pm 35$	$2_{-2}^{+126}$	$60_{-35}^{+131}$

Table 2.3: Predicted reflectance  $r_{\text{PQED}}(\lambda)$ , predicted internal quantum deficiency  $iQD(\lambda)$ , and predicted external quantum deficiency  $\Delta_p$  for the comparison conditions at the new CR-facility of PTB. The uncertainties are stated with a coverage factor  $k = 2$  (see text). For asymmetric uncertainty boundaries, the lower and upper boundaries are indicated by the subscript and superscript, respectively. The uncertainties of  $r_{\text{PQED}}$  and  $iQD(\lambda)$  are added quadratically to obtain the uncertainty of  $\Delta_p$ . The values of  $iQD(\lambda)$  are taken from [17] and the estimation of the uncertainty of  $r_{\text{PQED}}(\lambda)$  is taken from [18].

### Uniformity of the Spectral Responsivity of PQED Photodiodes

A dedicated setup was established to determine the uniformity of the spectral responsivity (uniformity) and the influence of the additional production step to apply the back electrode on this quality (see Figure 2.21). The PQED photodiodes under test were mounted inside a cryostat. The PQED photodiodes inside the cryostat were irradiated through a fixed Brewster-window by the power stabilised DFB-laser with a wavelength of 760 nm described in chapter 2.2. However, the laser power irradiating the photodiodes had to be kept below  $2.5 \mu\text{W}$  to prevent any non-linearity effect (see chapter 2.4.2) on the measured uniformity. To decrease the wanted radiant power, in addition to the laser radiation used to stabilise the laser power, the monitor detector and the single photodiodes were irradiated with radiation that is decoupled with wedged glasses with an angle of incidence of  $45^\circ$ . This setup improves the long term stability of the laser power at the expense of wanted radiant power and is shown in Figure 2.22. The reflectance of these glass elements is approximately 8% under these conditions. Thus, about 80% of the radiant power are deposited in the beam dump. This setup is advantageous, in comparison to using an attenuator to reduce the radiant power, because each of the radiant power measuring devices in this setup is irradiated with radiation that is in an

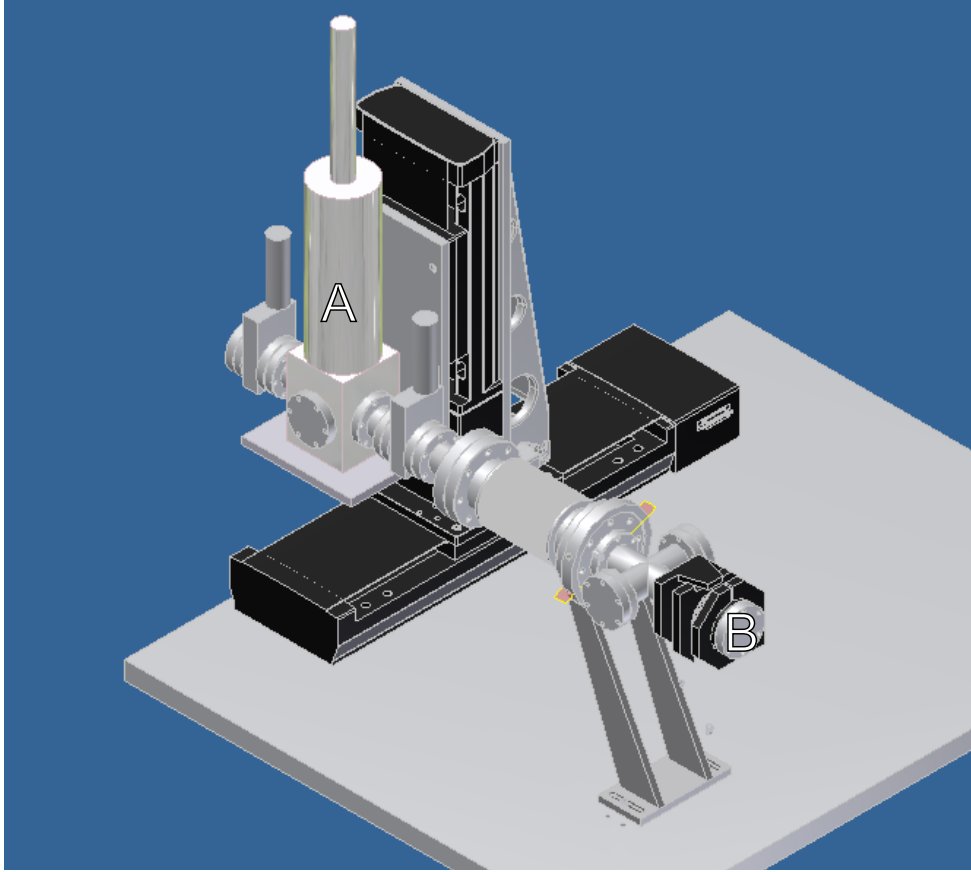


Figure 2.21: CAD-drawing of the setup to determine the uniformity of the spectral responsivity. The PQED-photodiodes are mounted in a cryostat (A) to provide clean room like ambient conditions and the possibility to change the temperature down to approximately 80 K. The single PQED photodiode is irradiated by a power stabilised DFB-laser with a wavelength of 760 nm through a fixed Brewster-window at position B (not shown) and mounted inside a cryostat on an x-y-translation stage to scan the uniformity of the spectral responsivity. The laser spot size was approx. 0.5 mm and the laser power was lower than  $2.5 \mu\text{W}$  to suppress any non-linearity while measuring. The photodiode temperature was  $25^\circ\text{C}$ .

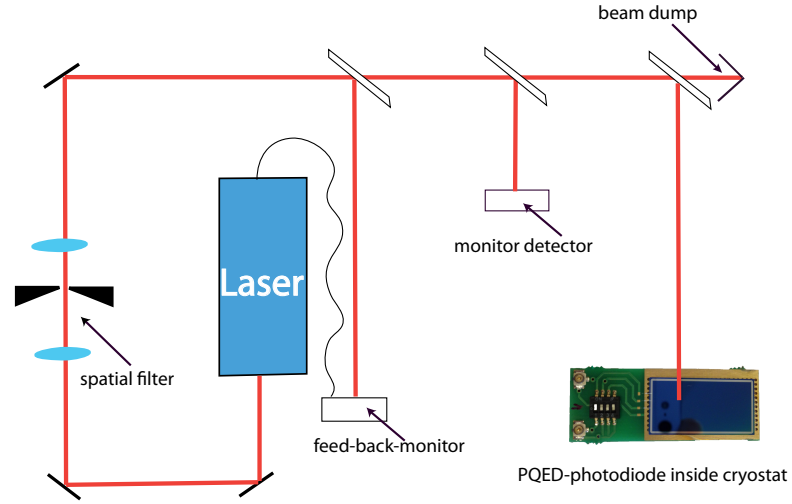


Figure 2.22: Schematic of the power stabilised laser source, adopted to enhance the long-term stability. The PQED-photodiodes, the monitor detector, and the feed-back-monitor for the power stabilisation are irradiated by radiation that is decoupled in an identical way. This setup reduces the influence of a change of the polarisation state of the laser radiation at the expense of wanted radiant power.

almost identical composite of polarisation states. Thus, this setup is more robust since a possible polarisation dependence of the power stabilisation system, that may occur when the ambient conditions are changing, is heavily reduced. The cryostat and, consequently, the photodiodes under test could be moved via an x-y-translation stage. The moveable cryostat and the fixed Brewster-window are connected via a flexible bellow. With this setup, it is possible to measure the uniformity without the influence of the uniformity of the Brewster-window. Building the facility from ultra high vacuum components satisfies the PQED requirements on the cleanness of the ambient conditions of the PQED photodiodes and gives the possibility to change the temperature of the photodiodes from room temperature down to about 78 K in a controlled way. The laser spot had a measured diameter at half maximum of 0.5 mm.

The uniformity was scanned starting in the upper left corner of the photodiodes and was moved sequentially, row by row, in 0.5 mm steps. At each measurement point the response of the photodiode was recorded for different applied bias voltages of 0 V, 5 V and 10 V. The stabilised laser power was monitored by a trap detector to correct the measured photocurrent for drifts in the laser power. To correct for any influence other than changes in the laser power and to determine the reproducibility of the measurements, the photocurrent was measured at the central point of the photodiodes after each scanned row. The reproducibility of these measurements, determined from the relative standard deviation of the reference measurements, was of the order of 70 ppm.

Thickness of SiO <sub>2</sub> -oxide layer	Back electrode	Uniformity	$u(\text{Uniformity})$
220 nm	Not included	0.045%	0.003%
220 nm	Included	0.054%	0.004%
302 nm	Not included	0.060%	0.006%
302 nm	Included	0.095%	0.004%

Table 2.4: Measured relative uniformity of the spectral responsivity of a randomly chosen photodiode of each type produced. The measurements were performed at a wavelength of 760 nm. The uniformity is given as the standard deviation of the measured points normalised by the monitor detector, the reference point and the mean of the photocurrent measured at the positions inside the electrode ring (see Figure 2.14(a) and Figure 2.18).

The measurements were performed at room temperature only. An imperfect vacuum caused by the cryostat led to a slowly growing ice layer on the photodiodes at temperatures below the freezing point of water and, therefore, prevented reliable measurements at a temperature of 80 K. At room temperature the vacuum system removed the humidity layer on the photodiode surface and no temporal change of the reflectance of the tested photodiodes was observed. However, the results obtained at room temperature are sufficient to evaluate the uniformity of the photodiodes. The results of the uniformity measurements at a reverse bias voltage of 10 V are given in Table 2.4. This reverse bias voltage was chosen to maximise the internal quantum efficiency. The relative change of the spectral responsivity is smaller or equal to 0.060% for clean photodiodes. A change of the responsivity of 0.060% corresponds to a local change of the SiO<sub>2</sub>-oxide thickness of  $\approx 0.8$  nm. As an example, the measurement result of a 300 nm SiO<sub>2</sub>-oxide-photodiode is shown in Figure 2.23. The results shown in Table 2.4 suggest that there is no dependence of the uniformity on the SiO<sub>2</sub>-layer, though the results for the 220 nm SiO<sub>2</sub>-oxide photodiodes are slightly better. The photodiode with the 300 nm SiO<sub>2</sub>-oxide layer with additional back electrode shows the highest non-uniformity. This photodiode was investigated after the measurement campaign was finished and it became obvious that this photodiode has not been properly cleaned by the manufacturer. Finally, it was not possible to counter measure this type of photodiode because the spare sample got damaged while incorporating it in the measurement facility. The data obtained so far show no significant influence of the additional production process to apply the back-side electrode on the uniformity of the spectral responsivity. The very low non-uniformity is covered by the seven reflection trap design of the PQED. A change of the reflectance of a single photodiode by 0.1% would change the reflectance of the PQED by about 0.2% and, thus, is negligible.

### Linearity of the Spectral Responsivity of PQED Photodiodes

The linearity of a detector is a key feature for every detector used in radiometry. The linearity has been studied for several types of photodiodes [50, 51, 68, 86]. The response

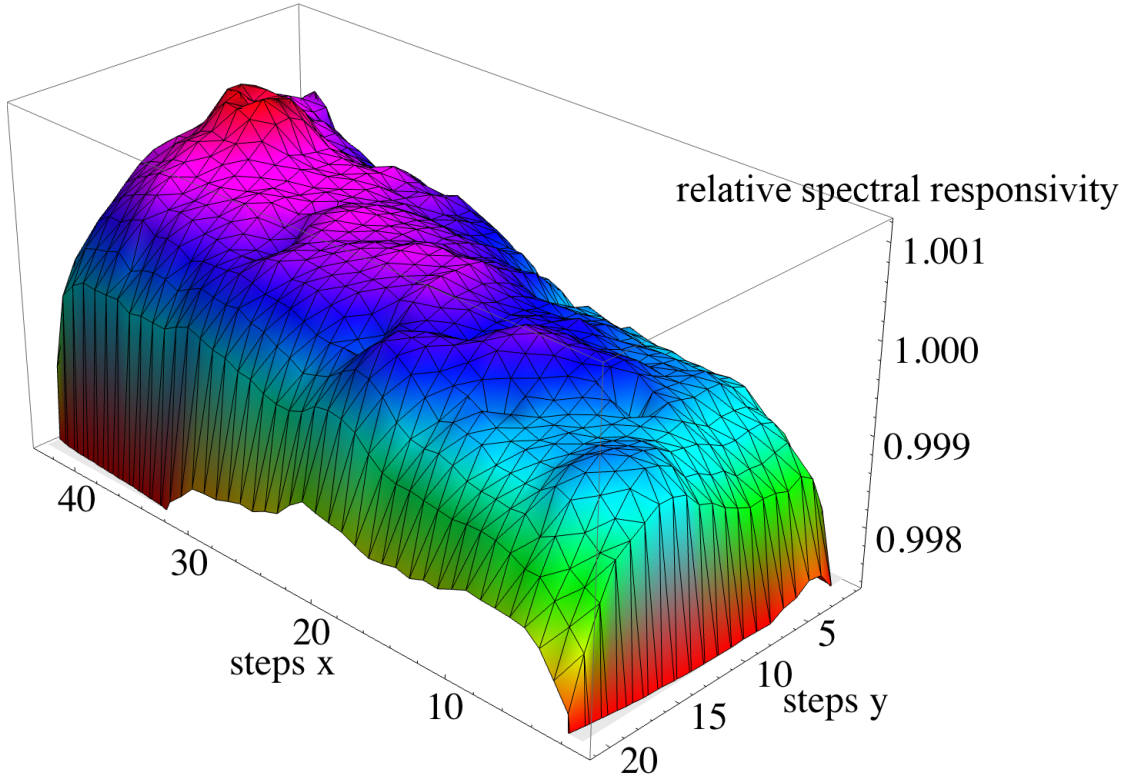


Figure 2.23: Uniformity of the spectral responsivity of a photodiode with a SiO<sub>2</sub>-oxide layer of 300 nm. The figure shows the deviation from the mean of the central photodiode area. The measurement was performed at a wavelength of 760 nm, at room temperature, with a step size of 0.5 mm, and with a reverse bias voltage of 5 V.

of a photodiode to optical radiation can be described with an equivalence circuit containing a voltage source, a diode connected in parallel, a series resistance and a load resistance. The shunt resistance and the capacitance of the photodiode are neglected for this discussion (see Figure 2.24) because they have no influence on the linearity. The output of an illuminated photodiode is given by [86, 87]:

$$I_T = I_L - I_0 \left[ \exp\left(\frac{eV_d}{nkT}\right) - 1 \right] \quad (2.14)$$

with  $I_T$  the output current,  $I_L$  the radiation generated current,  $V_d$  the forward voltage across the photodiode,  $I_0$  the reverse saturation current,  $n$  the photodiode-ideality factor to consider recombination losses that occur in the junction,  $k$  the Boltzmann constant,  $e$  the elementary charge and  $T$  the temperature of the photodiode. This equation can

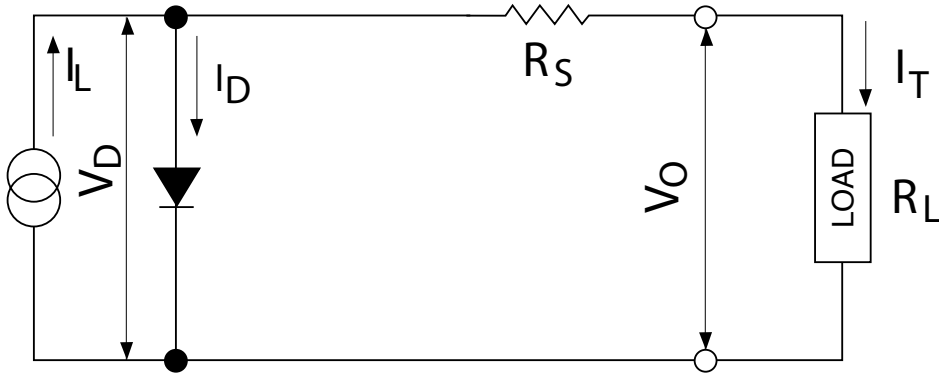


Figure 2.24: Equivalence circuit of a photodiode in series with a resistance  $R_S$ . The symbols are:  $I_T$  the radiation generated photocurrent,  $V_D$  the forward voltage across the photodiode,  $I_D = I_0[\exp(\frac{eV_D}{nkT}) - 1]$  the current through the diode,  $R_S$  the series resistance,  $V_O$  the output voltage,  $R_L$  the load resistance and the output current  $I_T$ . The shunt resistance and capacitance of the photodiode are not shown as the influence on the linearity of the photodiode of these parameters can be neglected.

be written in terms of series resistance  $R_S$  and the load resistance  $R_L$ :

$$I_T = I_L - I_0[\exp(\frac{eI_T}{nkT})(R_S + R_L) - 1] . \quad (2.15)$$

If the photodiode is illuminated,  $I_T$  can become large and produces a noticeable voltage drop across  $R_S$  and causes forward injection to occur in the photodiode that reduces the resulting current to the load. From (2.15) it can be seen that the linear range is determined by the series resistance and load resistance. The shunt resistance does not have to be taken into account for this estimation as the shunt resistance is of the order of several  $M\Omega$  to  $G\Omega$  and, therefore, much higher than  $R_S$  and  $R_L$  which are typically below 1  $k\Omega$ .

The influence of the series resistance on the linearity is of special importance for induced junction photodiodes as they are applied in the PQED. The series resistance of this type of photodiode is directly connected to the induced charges at the n-p-junction and a change in the linearity at high optical radiant power levels is caused by a degradation of this junction [88]. Thus, linearity measurements can provide a helpful instrument for a self-calibration procedure for the PQED, i.e. to detect a possible change of the quality of the n-p-junction by purely optical measurements.

The linearity was measured with a setup as described in [66] and [57], adopted to use the power stabilised DFB-laser working at 760 nm (see chapter 2.2) and the cryostat containing the PQED photodiodes. The maximum available laser power was of the order of 300  $\mu W$  limited by the losses in the laser stabilisation and the optical path including

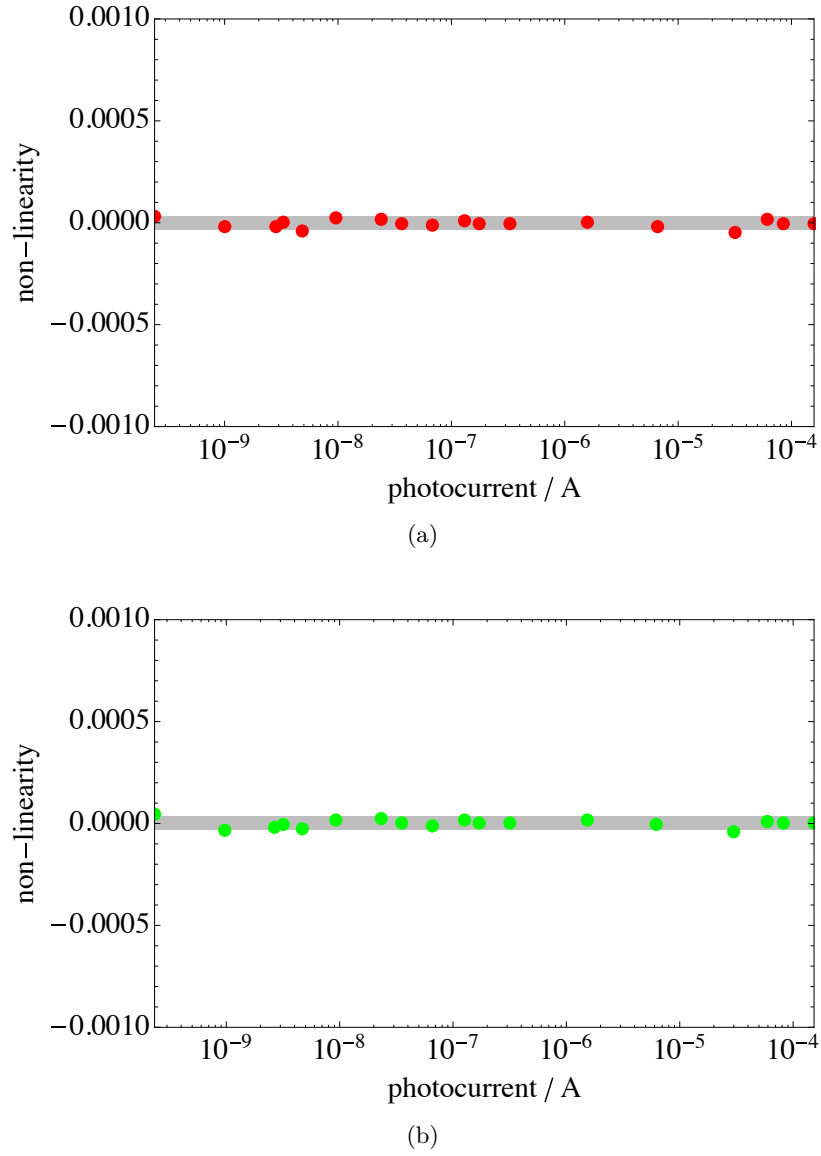


Figure 2.25: Non-linearity of sample PQED photodiodes with a 300 nm  $\text{SiO}_2$ -oxide layer (Figure 2.25(a)) and a 220 nm  $\text{SiO}_2$ -oxide layer (Figure 2.25(b)). No non-linearity was detected within the uncertainty of the measurements of  $3 \cdot 10^{-5}$  (marked as grey shaded area in the figures) up to a radiant power level  $300 \mu\text{W}$  at a wavelength of 760 nm, a bias voltage of 5 V and room temperature.

## 2 Improving Radiant Power Scales

the beam profile preparation. The spot diameter was about 2.5 mm at half maximum. These parameters are typical at the laser-based cryogenic radiometer of PTB.

To determine the linearity, the stabilised laser beam is divided into two parts going two different optical paths, path A and path B, and are then superimposed on the detector (see also [66]). The two paths A and B can be individually blocked. The non-linearity  $NL$  is then given by:

$$NL(I_{A+B}) = 1 - (I_A + I_B)(I_{A+B})^{-1} \quad (2.16)$$

with the resulting photocurrents  $I_A$  for only path A,  $I_B$  for only path B, and  $I_{A+B}$  for both paths A and B and adjusted so that  $I_A \approx I_B$ . Two photodiodes were tested in terms of linearity, one 300 nm SiO<sub>2</sub>-oxide layer photodiode and one 220 nm SiO<sub>2</sub>-oxide layer photodiode. Up to the maximum available laser power on the detector of approximately 300  $\mu$ W, the results (see Figure 2.25) show no non-linearity within the uncertainty of these measurements of  $u(NL) = 3 \cdot 10^{-5}$ . In addition, a measurement was performed without laser stabilisation to provide an increased laser power of the order of 1 mW. Due to the unstable laser power higher uncertainties of  $8 \cdot 10^{-5}$  occurred. The detector output became sub-linear at a photocurrent of 450  $\mu$ A due to the series resistance of the photodiode i.e.  $NL(450 \mu A) = -1.5 \cdot 10^{-3}$  (see Figure 2.26). Thus, the PQED can be used to obtain reliable measurements of the radiant power up to a radiant power of approximately 750  $\mu$ W.

### Characterisation of the Predictable Quantum Efficient Detector

The assembled PQED was compared with the CRCF. P-polarised laser radiation at wavelengths of 760 nm and 532 nm was used for the comparison. To validate the PQED, the predicted external quantum deficiency (2.12) was compared with the experimentally determined external quantum deficiency. The latter is given by

$$\Delta_m(\lambda) = 1 - \frac{S_m(\lambda)}{S_0(\lambda)} . \quad (2.17)$$

Where  $S_m(\lambda)$  is the measured spectral responsivity,  $S_0(\lambda) = e\lambda/hc$  is the spectral responsivity of an ideal quantum detector, assuming that each absorbed photon generates exactly one electron-hole-pair, defined by  $h$  the Planck constant,  $c$  the speed of light in vacuum,  $e$  the elementary charge and  $\lambda$  the vacuum wavelength of the laser radiation. The spectral responsivity is obtained from the relation

$$S_m(\lambda) = \frac{I_{\text{phot}}(\lambda)}{P(\lambda)} \quad (2.18)$$

which connects the measured photocurrent of the PQED  $I_{\text{phot}}(\lambda)$  and the radiant power  $P(\lambda)$  measured with the CRCF.

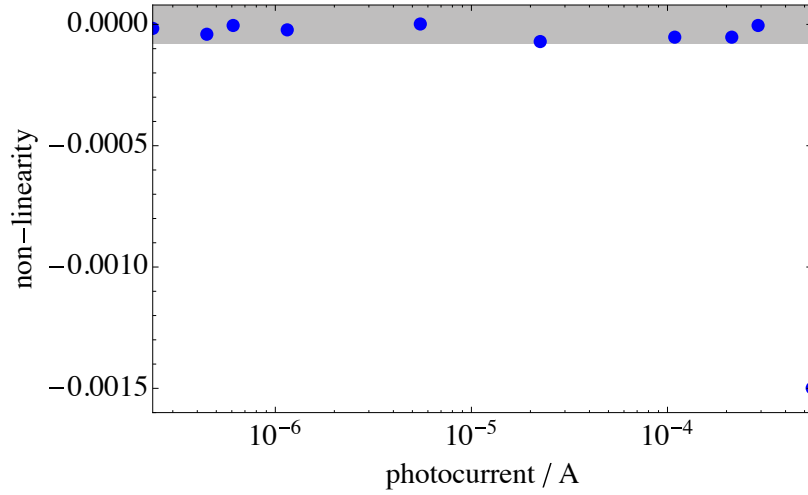
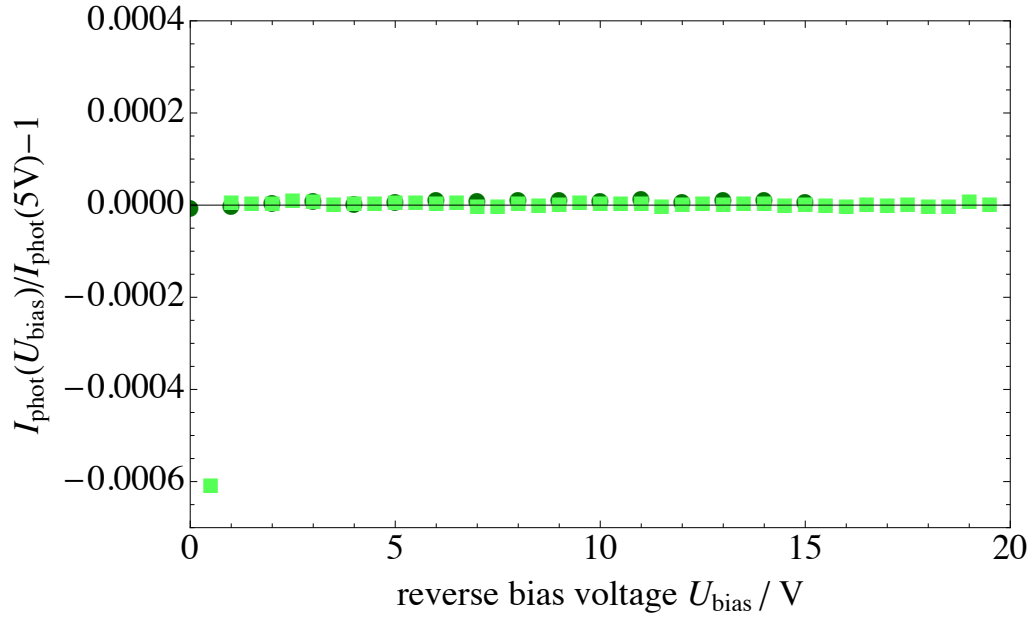


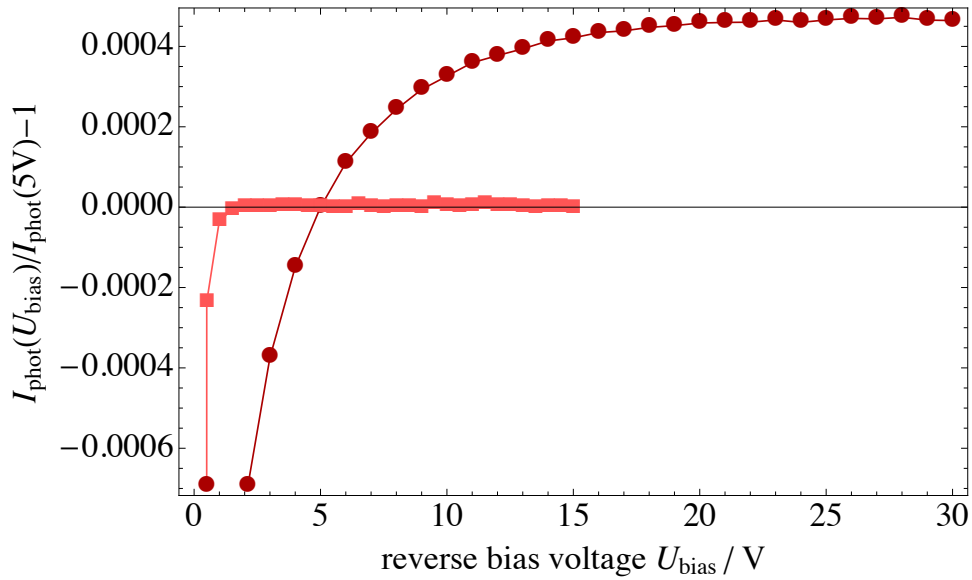
Figure 2.26: Non-linearity of a 220 nm SiO<sub>2</sub>-oxide layer photodiode up to a laser power of 450  $\mu$ W. To reach the higher radiant power level the laser stabilisation had to be removed which led to higher scatter of the measurement points. At a photocurrent of 450  $\mu$ A sub-linearity occurs due to the series resistance of the photodiodes (see text). The non-linearity could not be measured at higher photocurrents due to the limited available laser power. The uncertainty of the measurements of  $8 \cdot 10^{-5}$  is marked as grey shaded area.

### Responsivity of the PQED as a Function of Bias Voltage

To determine the necessary reverse bias voltage where the internal quantum efficiency saturates, the dependence of the photocurrent on the bias voltage was measured. An increasing reverse bias voltage extends the depletion region of the photodiodes. As shown in Figure 2.4, the internal quantum efficiency is assumed to be unity in the depletion zone. If the photocurrent does not further increase with higher reverse bias voltages, all the radiation is absorbed in the depletion zone. Hence, the saturation of the internal quantum efficiency is assumed to be a measure of the eliminated internal losses of the PQED [17]. This investigation was performed at the wavelengths of 532 nm and 760 nm and at the temperatures of  $T_{\text{LN}_2} \approx 78$  K and at  $T_{\text{room}} \approx 298$  K. Two different power stabilised laser, with wavelengths of 532 nm and 760 nm wavelength, and an additional monitor detector were used to minimise the influence of power fluctuations on the signal. The results (see Figure 2.27) show that the reverse bias voltage where the internal quantum efficiency saturates, i.e. where the photocurrent becomes independent of the applied reverse bias voltage, is a function of temperature and wavelength of the radiation. Furthermore, these measurements have been used to enhance the accuracy of the simulation of the internal quantum efficiency with PC1D [17] by fitting input parameters of PC1D such as charge carrier lifetime, to fit the predicted reverse bias dependence of the photocurrent with the experimental results. At lower temperatures, the absorption



(a)



(b)

Figure 2.27: Measured deviation of the bias dependent photocurrent from the value at 5 V bias of the PQED plotted over the bias voltage for a laser wavelength of 532 nm (Figure 2.27(a)) and 760 nm (Figure 2.27(b)). The photocurrent  $I_{\text{phot}}$  was determined by subtracting the bias dependent dark current from the output under illumination. The squares show results at room temperature and circles show the results at the temperature of liquid nitrogen.

coefficient is decreased and, thus, a significant fraction of photon-generated electron-hole-pairs may appear in the bulk volume of the photodiodes. Here, the charge-carrier collection is not as efficient as close to the n-p-junction. To reduce the recombination losses for wavelengths longer than 700 nm at temperatures around 78 K a reverse bias voltage of 20 V or higher has to be applied (see Figure 2.27(b)). However, at room temperature and at temperature of about 78 K for 532 nm, a reverse bias voltage of 5 V was sufficient to reach the maximum internal quantum efficiency (see Figure 2.27(a) and 2.27(b)).

### Determination of the External Quantum Efficiency of the PQED

The determination of the external quantum efficiency of the PQED was performed at the CRCF (see chapter 2.3.1 and [19]). The spectral responsivity of the PQED was measured at the wavelengths 532 nm and 760 nm and the temperatures  $T_{LN_2} \approx 78$  K and  $T_{room} \approx 298$  K. The laser power was power stabilised to better than 5 ppm and monitored by a Si-photodiode based trap detector to correct for the remaining fluctuations of the laser power. The spectral responsivity of the PQED is obtained according to (2.18). The most relevant contributions to the uncertainty budget are given in Table 2.5. The measurement of the transmittance of the Brewster-window does not contribute since all the detectors are measured behind the same window. The stray light is measured in the vicinity of the apertures of the PQED and the cryogenic radiometer as both have a similar diameter. For this purpose, a stray light detector was built into the CRCF. This detector is made from a Hamamatsu S1337 photodiode that is covered by a blackened metal-plate that has a circular aperture with an additional disc in the centre (see Figure 2.28) to measure the stray light around the edges of the apertures of the CRCF and the PQED. To perform the stray light correction, the diameter of the detector apertures have to be known. The diameters were measured by scanning with the laser beam over the detector area in vertical and horizontal direction starting at the centre. From the positions where the photocurrent of the detectors dropped to 50% of the initial value, the diameter of the detector apertures can be calculated.

The laser wavelength was measured with a wave-meter before and after each comparison with an uncertainty of 0.001 nm. The results of the comparison of the PQED with the CRCF is shown in Table 2.6. The measurements were performed in a time span of 6 months. The validation of the prediction of the external quantum efficiency of the PQED was performed by comparing the experimental result  $\Delta_m(\lambda)$ , determined according to (2.17), with the predicted external quantum deficiency  $\Delta_p(\lambda)$ . The latter was calculated from the PQED reflectance and the calculated internal quantum deficiency  $iQD$  and is given in Table 2.6 for the comparison conditions, i.e. for wavelengths of 532 nm and 760 nm, temperatures of 78 K, and 298 K, and bias voltages of 5 V and 20 V. The experimentally determined external quantum deficiency  $\Delta_m(\lambda)$  is also listed in Table 2.6. The uncertainty bars of the predicted and measured external quantum deficiency overlap at the 95% confidence level, but the measured values seem to be systematically larger than the predicted values (see Figure 2.29). The combined relative standard uncertainty of the measured PQED responsivity achieved within this validation is of the order of



Figure 2.28: Photograph of the stray light detector. The cover is made from blackened metal and has a circular aperture slightly larger than the apertures of the detectors used and a blackened metal disc in the centre with a diameter slightly smaller than the apertures of the detectors. This detectors measures the stray light in the vicinity of the apertures of the cryogenic radiometer and the PQED.

source of uncertainty	Uncertainty / ppm
radiant power measurement with the CRCF	18.6
wavelength	2
stray light*	20
typical laser stability	4
photocurrent measurement	10
combined rel. standard uncertainty	29

Table 2.5: Main contributions to the uncertainty budget of the PQED validation measurements. Relative standard uncertainties are stated. \*The stray light uncertainty contains the positional error of the detectors and the difference of the apertures in front of the detectors.

$T/\text{K}$	$\lambda/\text{nm}$	$U_{\text{bias}}/\text{V}$	$\Delta_p(\lambda) / \text{ppm}$	$\Delta_m(\lambda)/\text{ppm}$
298	532	5	$18^{+144}_{-5}$	$85 \pm 60$
298	760	5	$54^{+128}_{-15}$	$167 \pm 58$
78	532	5	$19 \pm 10$	$85 \pm 56$
78	760	5	$86^{+689}_{-36}$	$656 \pm 56$
78	760	20	$60^{+131}_{-35}$	$207 \pm 58$

Table 2.6: Comparison of predicted and measured external quantum deficiency of the PQED at different temperatures  $T$ , wavelengths  $\lambda$ , and reverse bias voltages  $U_{\text{bias}}$ . The uncertainties are given at 95% confidence level. For the asymmetric uncertainty boundaries of  $\Delta_p(\lambda)$ , the lower and upper boundaries are indicated by the subscript and superscript, respectively.

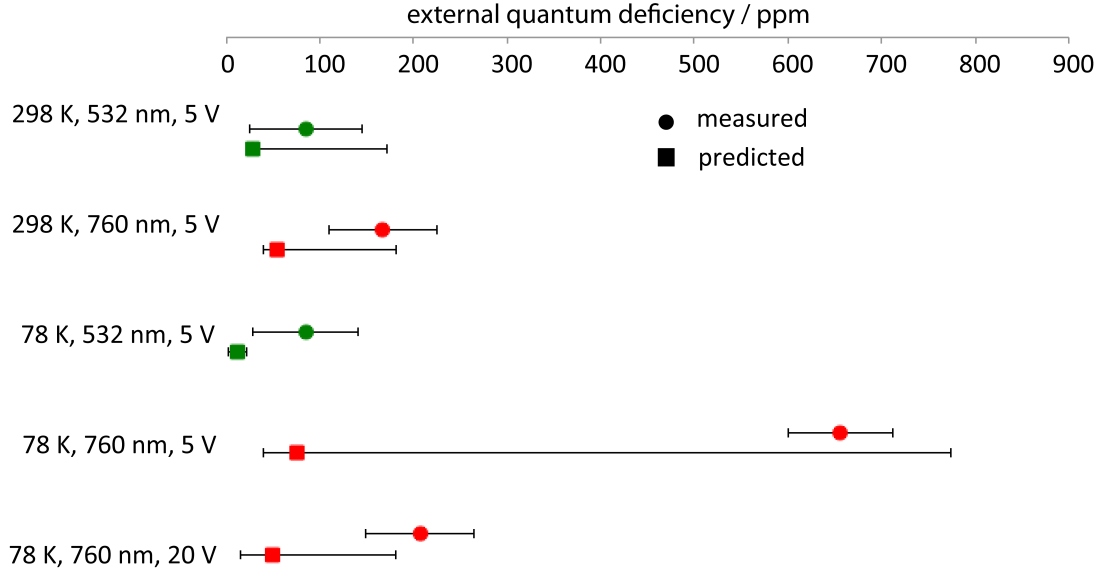


Figure 2.29: Comparison of measured (circles) and predicted (squares) external quantum deficiency of the PQED for the wavelengths 532 nm and 760 nm. The uncertainty of the predicted external quantum deficiency for the 760 nm, 78 K and 5 V reverse bias voltage is highly increased as compared to the other values. At this condition a higher fraction of photons is absorbed behind the n-p-junction, where the collection efficiency is decreased (see text).

30 ppm. This is an improvement of a factor  $> 3$  of the new cryogenic radiometer facility compared with its predecessor [24]. The main advantage of the new cryogenic radiometer facility is the absence of the Brewster window correction which is the major contribution to the uncertainties of most of the laser-based cryogenic radiometer facilities used at National Metrology Institutes.

### Comparison with Current State of the Art Transfer Standards

Trap detectors are the “working horses” in photometry and radiometry. They are widely used as they provide properties that make possible the low uncertainty dissemination of radiant power scales. As described in chapter 2.1.3, trap detectors are commonly calibrated at certain laser lines traceable to a cryogenic radiometer. Thus, the spectral responsivity has to be interpolated for wavelengths in between the wavelengths where the trap is calibrated with laser radiation. The two most important parameters for the interpolation of the spectral responsivity of trap detectors are the internal quantum deficiency, that is linked to the collection efficiency in (2.4), and the reflectance. To show the feasibility of using PQED-based working or transfer standards, i.e. to be used as a high quality detector that has been calibrated against a primary standard, the internal quantum deficiency and reflectance of the PQED operated at room temperature was compared with state-of-the-art trap detectors made from Hamamatsu S1337 photodiodes.

The internal quantum deficiency of the PQED, that was obtained from the measurements

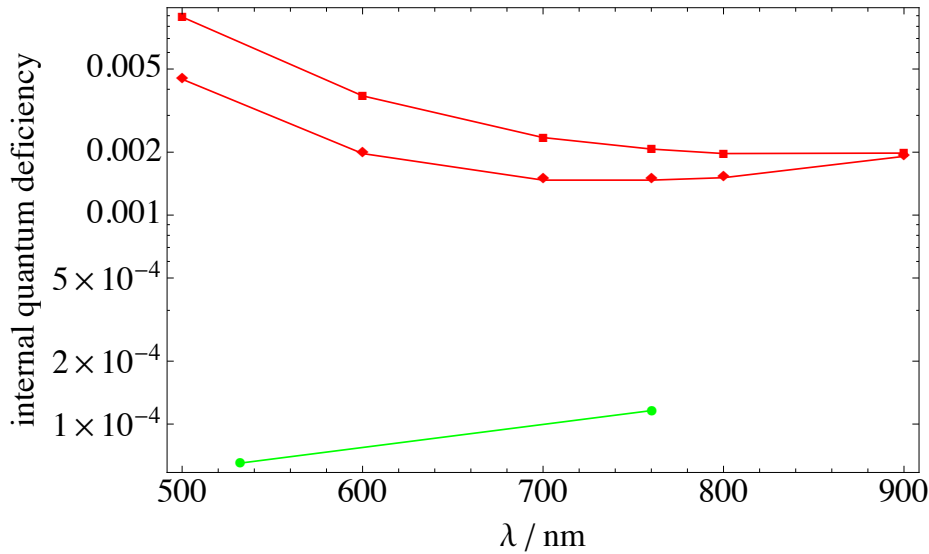


Figure 2.30: Comparison of the measured internal quantum deficiency of two trap detectors made from Hamamatsu S1337 photodiodes (red) that are used at PTB as transfer standards and of the PQED (green) plotted over the wavelength.

with the CRCF (see above) at the wavelengths 532 nm and 760 nm is plotted with the measured internal quantum deficiency of two trap detectors, that are used at PTB as transfer standards, in Figure 2.30. The internal quantum deficiency of the Hamamatsu S1337 photodiodes is two orders of magnitude larger at 532 nm and still one order of magnitude larger at 760 nm (see Figure 2.30). This is in agreement with the simulation of the internal quantum deficiency [17] that predicts an increasing internal quantum deficiency for wavelengths above 600 nm for the PQED. These low internal losses may reduce the uncertainties associated with the interpolation of the spectral responsivity. By solving the drift-diffusion-equations for the PQED, lower uncertainties in the determination of the spectral responsivity may occur when the systematical under estimation of the internal quantum deficiency is resolved.

While the reflectance of the traps, under ideal conditions, is polarisation independent

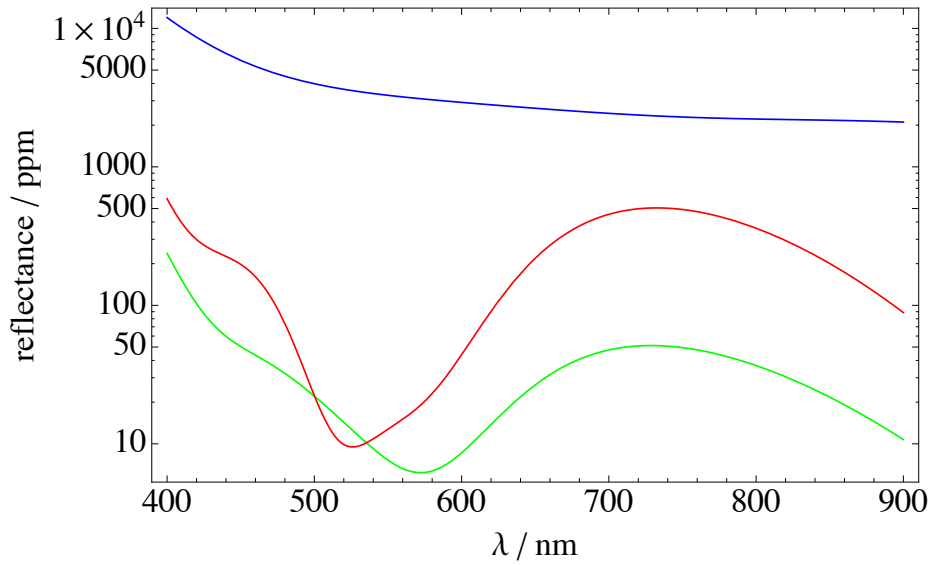


Figure 2.31: Comparison of the calculated reflectance of a three-element trap detector made from Hamamatsu S1337 photodiodes (blue) and of the PQED for p-polarised (green) and s-polarised (red) radiation plotted over the wavelength.

(blue line in Figure 2.31), the reflectance of the PQED has a distinct polarisation dependence. The comparison of the reflectance of the PQED and the traps is shown in Figure 2.31. If unpolarised radiation or radiation with an unknown state of polarisation is observed, the design of the PQED has to be adjusted to increase the number of reflections inside the PQED to remove the polarisation sensitivity of the PQED. However, the reflectance losses of the PQED are, depending on wavelength of the radiation, between 10 to 1000 times smaller than those of classical three-element trap detectors (see Figure 2.31).

Thus, the PQED is a great improvement for purposes where silicon photodiode based trap detectors are used in the wavelength range from 400 nm to 800 nm.

### 2.5 Conclusions

The goal to set up a cryogenic radiometer facility as a primary detector standard for optical radiant power capable for the operation at the 10 ppm level was achieved. The combined standard uncertainty of the measurement of radiant power behind the entrance aperture of the cryogenic radiometer cavity is 18.6 ppm. However, when the cavity absorptance has been measured traceable to the SI, the combined standard uncertainty may be reduced to 13 ppm, assuming a relative standard uncertainty of the measured cavity absorptance  $u(c_{ca})$  of 2 ppm. The results shown here are the best published so far. The comparison of two, at that time state of the art cryogenic radiometer [47], showed an uncertainty budget with a combined uncertainty of 26 ppm [47] for the LaseRadII and the NPL cryogenic radiometer. The improved setup presented here allows calibrations of ultra-high quality detectors like the PQED with a combined standard uncertainty of the order of 30 ppm (see Table 2.5). This low uncertainty is rendered possible in particular by the employment of a shared Brewster window for all detectors within the facility, the possibility to measure with the cryogenic radiometer and the DUTs at the same position relative to the beam with similar apertures, and the use of a stray light detector (see chapter 2.4 and Table 2.5).

The electro-optical characterisations described here provided crucial input for the development of the PQED. The characterisation of the induced junction photodiodes, custom-made for the PQED, proved favourable features. The measurement of the linearity of the photodiodes proved a linearity range from the sub-nanowatt radiant power range to about 400  $\mu\text{W}$  radiant power, thus making it the only potential primary radiometric detector standard that allows linear radiant power measurements over seven orders of magnitude of radiant power.

The results on the measured uniformity of the PQED photodiodes indicate that the measured low non-uniformity of a maximum of 0.06% for clean photodiodes is caused by local  $\text{SiO}_2$ -oxide thickness variations. This issue is solved by the trap design of the PQED.

The validation of the predictability of the PQED was performed with the new cryogenic radiometer with uncertainties better than 30 ppm (see chapter 2.4). The PQED offers ultra-low external and internal losses and, thus, a significantly smaller external quantum deficiency as compared to conventional trap detectors.

At room temperature, the predicted and measured external quantum deficiencies of the PQED agree within their 95% confidence intervals. This proves the possibility to use silicon photodiode based detectors as absolute detectors with uncertainties commonly achieved with cryogenic electrical substitution radiometers. However, the measured external quantum deficiency is always larger than the predicted external quantum deficiency.

At the temperature of liquid nitrogen and at short wavelengths in the visible, the un-

certainty of the predicted external quantum deficiency is an order of magnitude smaller than at room temperature. However, the overlap of the uncertainty bars of predicted and measured external quantum deficiency is reduced as compared to the room temperature results. Furthermore, the predictability of the internal losses decreases steeply for wavelengths longer than 700 nm at the temperature of liquid nitrogen. This is caused by the high uncertainty of the available data for the absorption coefficient of silicon at this temperature. However, PQED operation at low temperatures may achieve unrivalled low uncertainties by using improved detector designs and modelling techniques of the predicted responsivity.

Nevertheless, the difference between predicted and measured results indicates a systematic nature of the deviation. This systematic underestimation of the internal quantum deficiency is most probably caused by the one-dimensional modelling of the internal quantum deficiency [17]. By using a three-dimensional software, these issues are expected to be resolved by taking into account the recombination losses at the higher doped regions, where the ohmic contacts are located.

To be used as a primary detector standard, the temporal stability of the photodiodes has to be investigated, especially for wavelengths around 400 nm, where most photodiodes show temporal drifts in this wavelength range which is relevant for photometric applications. When these pre-conditions are given, the PQED satisfies the requirements for a primary detector standard.

Thus, the PQED is an ultra-high quality detector that combines ultra-low internal and reflectance losses. The polarisation sensitivity of the PQED (see Figure 2.31) is a drawback that can be overcome by a higher number of reflections inside the PQED. The low losses of the PQED make it a potential primary detector standard and transfer standard for inter-comparisons and the dissemination of radiant power scales with very low uncertainties.

The ultra-low measurement uncertainty of the cryogenic radiometer facility in conjunction with the ultra-high quality detectors validated in this work will allow the dissemination of the radiant power scale of PTB to stakeholders and other NMIs with unrivalled low uncertainties. This will be achieved by the lower uncertainty of the interpolation of the spectral responsivity of the PQED-based transfer standards between the laser lines where the detector was calibrated (see chapter 2.1.3).

However, to render possible the use of the QED as a primary detector standard for visible radiation, several efforts will be necessary. Most of them are object of research in the joint research project of the European Metrology Research Programme: “New primary standards and traceability for radiometry” starting in October 2013. Within this project three aspects of the PQED are addressed: The improvement of the prediction of the spectral responsivity, the experimental validation of this prediction with lower uncertainties and the integration of the PQED into applications such as photometers to shorten the traceability chain. To improve the modelling of the PQED a three-dimensional software will be used while the current prediction is based on one-dimensional modelling.

However, the development of the PQED and especially the modelling of the responsivity was an iterative process. The electro-optical characterisation of the photodiodes revealed that, at temperatures of 80 K, the optical parameters of the silicon heavily affect the

## *2 Improving Radiant Power Scales*

response of the PQED. This input was crucial for the development of the prediction of the spectral responsivity with a one dimensional software. Furthermore, the comparison of the PQED and the CRCF with extremely low uncertainties exposed a systematical underestimation of the internal quantum deficiency. Indeed, the measurements proved that one-dimensional modelling of the response of the PQED is not sufficient to quantitatively predict the internal quantum deficiency.

Finally, the PQED is the major detector development in the recent years, aiming to reduce the uncertainties in radiant power measurements in the visible by one to two orders of magnitude down to the ppm level.

### 3 Bridging the Radiometric Gap

In this chapter, several ways to bridge the radiometric gap are discussed and a synchrotron radiation based method is introduced. The radiometric gap in the traceability chain occurs in the transition of radiant power measurements to the counting of photons with single photon detectors, i.e. between the classical radiometry and the few photon radiometry, where only high uncertainty calibrations of photodetectors are commonly available.

In the following sections four different calibration techniques for single photon detectors, that are traceable to the SI or that are primary methods, are described. The “spontaneous parametric down conversion” (SPDC) method, the “quantum cloning” method, the “substitution” method, and the “synchrotron radiation” method. Each of the methods has some drawbacks. For the substitution method, i.e. the measurement of the same radiant power with a calibrated classical reference detector and a single photon detector at high count rates, the single photon detector needs to be well characterised in terms of dead time which often depends on the measured count rate and on the single photon detector temperature. In addition, the linear response of the reference detector needs to be well known down to a very low radiant power level where precise measurements, especially linearity investigations of classical detectors, are hardly possible. If the SPDC is used, the losses in the optical path, the uniformity of the applied crystal, etc., need to be measured with high accuracy and limit the achievable uncertainty.

Finally, the synchrotron radiation method offers the highest flexibility in terms of radiant power and useable wavelengths but is not easily available for the stakeholders.

In section 3.1, the operation principle of the single photon detectors used in this work is briefly described and a definition of the terms used in this work to describe the performance of single photon detectors is given.

In section 3.2.1, two absolute methods to calibrate single photon detectors based on spontaneously decays in an optical parametric process and the so-called no-cloning-theorem are briefly described.

In section 3.2.2, the substitution method, a calibration method traceable to the SI, with own experimental results is briefly described.

In section 3.3, the calibration method based on synchrotron radiation is introduced and described in detail and experimental results are given.

## 3.1 Single Photon Detectors

The few photon metrology is a rather new field of research. As a result of that, the terms necessary to describe single photon detectors used among different research groups have not been consolidated yet. To define the terms used in this work to characterise single photon detectors an introduction into the operation principle of the single photon detectors used within this work is given. Using these two examples, i.e. single photon avalanche diodes (SPADs) and superconducting nano-wire single photon detectors (SNSPDs), a set of definitions is provided that is used at PTB and NIST and sees growing application world-wide.

In the first part of this section the two types of single photon detectors used in this work are briefly described while the second part gives an overview of the key characteristics of single photon detectors.

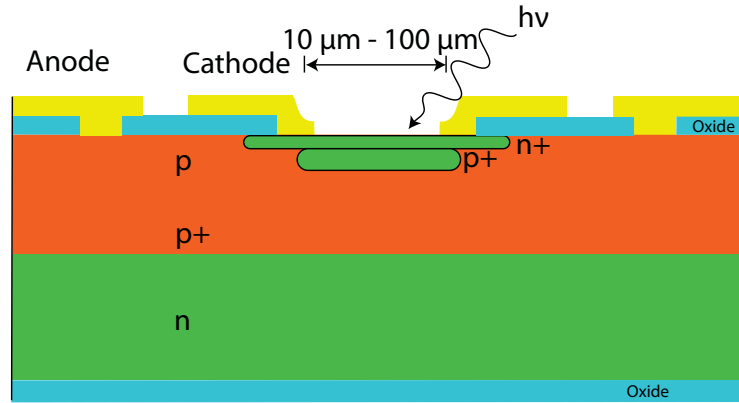
### 3.1.1 Types of Single Photon Detectors

The first detectors able to resolve single photons were photomultiplier tubes [89] developed in the 1930s.

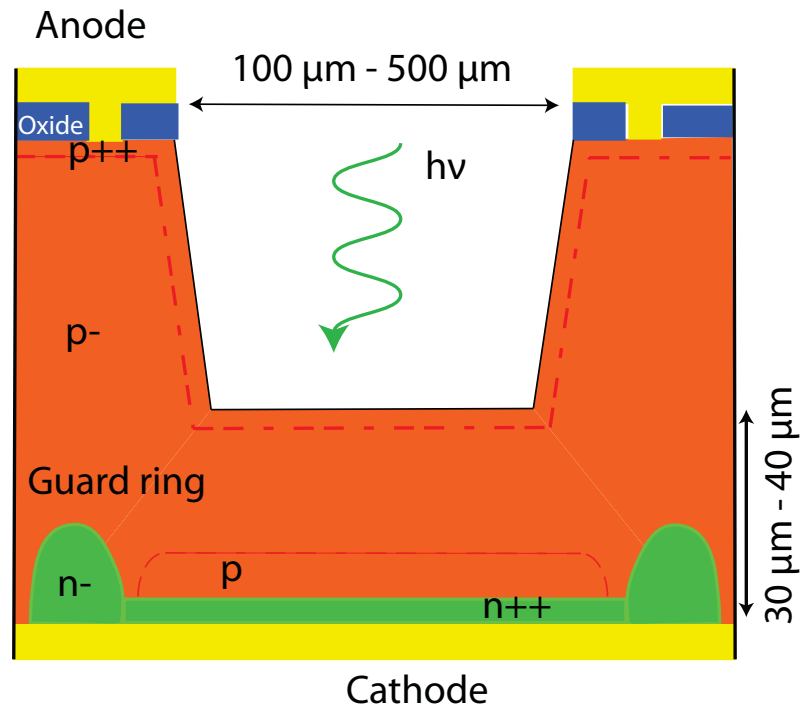
In the 1960s the first single photon detectors based on solids were introduced. In the visible, the, so-called, Geiger-mode avalanche photodiodes [90] offer high quantum efficiency and low noise as compared to analog detectors. Avalanche photodiodes, specially designed and fabricated to detect single photons, will be named as single-photon avalanche photodiodes (SPADs) in this work. SPADs can also be tailored to work in the near infrared (NIR). In the NIR it is very difficult to combine high quantum efficiency and low noise operation. Thus, devices working in the NIR are inferior to devices designed to operate in the visible in all characteristics. Especially the wavelengths of 1310 nm and 1550 nm, the so-called telecom wavelengths, are important for many applications of single photon detectors and, thus, a lot of effort is put into enhancing NIR-SPADs [91]. Two recent reviews of single photon detectors and their technologies can be found in [92] and [93]. Within this work, free space SPADs were used for the experiments in the visible and fibre-coupled superconducting nano-wire single photon detectors (SNSPDs) were used at the telecom wavelengths. The operation principle of these types of single photon detectors is briefly described below.

#### Single Photon Avalanche Photodiodes

The SPAD is the “working horse” for single photon experiments and measurements in the visible wavelength range. Most experimenters prefer, so-called, single photon counting modules, where the SPAD is coupled with some electronics to provide stable operation conditions and a standardised response to photons. SPADs can be divided into two groups, “thick” and “thin” SPADs, which refers to the depletion layer of the p-n-junction [94]. The figures 3.1(a) and 3.1(b) show typical cross sections of “thick” and “thin” devices. The thin-SPADs have a depletion layer thickness of about 1  $\mu\text{m}$  while the depletion layer of thick-SPADs can have extensions from 20  $\mu\text{m}$  to 150  $\mu\text{m}$ .



(a) Cross section of a typical “thin” junction single photon avalanche photodiode.



(b) Cross section of a typical “thick” junction single photon avalanche photodiode.

Figure 3.1: Cross sections of “thin” and “thick” single photon avalanche photodiodes.

### 3 Bridging the Radiometric Gap

Thin-SPADs have breakdown voltages between 20 V to 50 V, small active areas from  $20\text{ }\mu\text{m}$  to  $50\text{ }\mu\text{m}$  and a maximum detection efficiency of about 45% at 500 nm declining at longer wavelengths. Thick-SPADs, the kind of SPAD used in this work, have breakdown voltages of 200 V to 500 V, large active areas of up to  $500\text{ }\mu\text{m}$  and high detection efficiencies of more than 50% in the visible wavelength range, but are very costly devices. A SPAD is, in principle, a p-n-junction biased at a voltage above the breakdown voltage. If a single charge carrier is injected into the depletion layer the high electric field triggers a self-sustaining avalanche [95]. Thus, a macroscopic current rises with a sub-nanosecond rise-time, to a steady value in the milliampere range. The leading edge of avalanche pulse marks the arrival time of the absorbed photon. To prevent damage to the SPAD this high avalanche current has to be quenched by reducing the bias voltage below the breakdown value. A description of the quenching methods, i.e. active and passive quenching, can be found, for instance, in reference [95]. Afterwards the voltage has to be restored to become sensitive again. Most SPADs can be gated to reduce the noise level of the devices. The maximum count rate of SPADs is limited by the deadtime, the maximum gating frequency, if the gating function is used, and the maximum energy dissipation which can be in the 10 W range. In this work two single photon counting modules manufactured by Perkin-Elmer [96] were used.

#### Superconducting Nanowire Single Photon Detectors

Though it is known since the early 1970s that superconductivity [97] can be destroyed by optical radiation [98], it took another 25 years until superconducting nano-wire single photon detectors (SNSPDs) were proposed by Kadin et al. [99]. The first simulations of the response of a SNSPD to optical radiation were performed by Semenov et al. [100] shortly before the first experimental results were available by Gol'tsman et al. [101]. A review of the theory and applications of hotspot-based detectors can be found in [102]. SNSPDs are made from a NbN-nanowire of a thickness of about 5 nm and strip widths from 80 nm to 200 nm. The wire usually has a meander structure with dimensions in the range from  $5 \times 5\text{ }\mu\text{m}^2$  to  $10 \times 10\text{ }\mu\text{m}^2$  to create a practical sensitive area and to achieve a higher detection efficiency. Some considerations regarding the layout and processing of these detectors can be found in [103].

The superconducting energy gap  $2\Delta$ , the superconducting equivalent to the band-gap in semiconductors, is two to three orders of magnitude smaller than in a semiconductor. Thus, the sensitivity of these devices is much higher than that of photodiode based systems and extends the wavelengths detectable far into the infrared [104].

The mechanism that leads to the detection of a photon is shown in Figure 3.2. The detector is current biased to typically 90% of its critical current. Around this bias value there is a good trade-off between detection efficiency and noise of the detector. When a photon with an energy  $\hbar\omega \gg 2\Delta$  is absorbed, a non-superconducting hotspot is formed (Figure 3.2(a)) with dimensions of the thermalisation length  $2\lambda_T$ . The resistive hotspot grows due to the diffusion of hot electrons out of its centre (Figure 3.2(b)). This extension of the “hot-spot” forces the supercurrent to flow in the “sidewalks” between the hot-spot and the edges of the nano-wire (Figure 3.2(c)). If the hot-spot reaches a

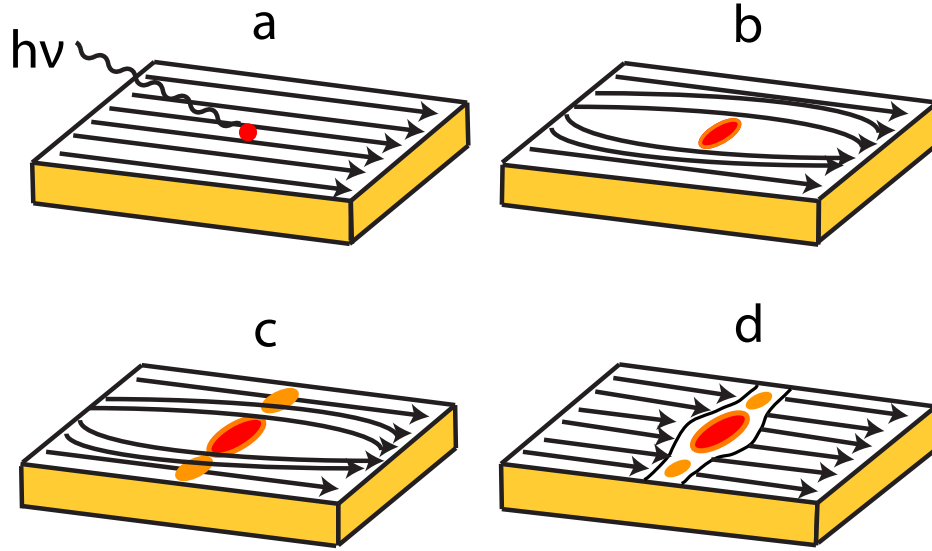


Figure 3.2: Schematics of the supercurrent-assisted hotspot formation mechanism in an ultra-thin and narrow superconducting strip, kept far below the critical temperature are shown (see text). The arrows indicate the direction of the supercurrent flow.

sufficient size in conjunction with the bias current, the critical current density is exceeded in the sidewalks and a resistive barrier is formed (Figure 3.2(d)). This gives rise to the output of a short voltage pulse that can be amplified and detected with standard counting equipment. The time span between the absorption of a photon and the cooling of the hotspot, restoring the superconducting state, is of the order of 30 ps [101]. The maximum detection rate of these devices is limited by the kinetic inductance [105] that increases linearly with the length of the nano-wire. The output pulse has a kinetic-inductance-caused length of typically 4 ns to 10 ns. This time can be adjusted at the time of manufacturing by changing the size of the detector or by connecting several SNSPDs in parallel as described, e.g., in [106]. The detection efficiency of fibre-coupled systems [107] at 1550 nm is of the order of 20% for high quality devices and can be increased to 57% for customised devices with integrated optical cavities and anti-reflective coating [108]. A major drawback of these systems is the strong dependence of the detection efficiency on the state of polarisation of the radiation incident on the detector [109, 110]. The reason of this behaviour has been investigated by Semenov et al. in [109]. They observed a different absorbance of the thin meander for radiation polarised parallel or perpendicular to the meander wires. The absorbance is, according to [109], approximately 50% higher for radiation polarised parallel to the meander wires. Hence, control of the polarisation state incident on the detector is required if stable detection efficiencies are necessary.

#### 3.1.2 Characteristics of Single Photon Detectors

An ideal detector has a unity quantum efficiency, no noise and can detect each photon independently and unaffected by the incident rate. In addition, the detector has to be able to resolve the number of incident photons. In reality, it is possible to find close to ideal detectors when only one quality is considered but the other qualities are often compromised. For example, so-called transition edge sensors [111, 112] reach almost unity quantum efficiencies at the expense of speed. Though single photon detectors are becoming a more and more mature technology, there is still a lack of a standardised set of parameters characterising the performance of these devices or terms like detection efficiency and quantum efficiency (see below) are used without definition. The parameters used in this work are described below. In addition, the typical values of these parameters for SPADs and SNSPDs are given.

**Quantum efficiency** is the probability that an absorbed photon is transferred into an electrical output signal.

**Detection efficiency** is the probability that an incident photon causes an electrical output signal taking into account all losses associated with the detector such as coupling losses for fibre-coupled devices or the protective glass in front of SPADs. “Thick”-SPADs can reach detection efficiencies of up to 85% at the “red” wavelengths. High quality fibre-coupled SNSPDs have detection efficiencies of up to 25% at 1550 nm.

**Dark count rate** is the count rate of the detector in the absence of any light and equates to the noise of the detector. The dark count rate of SPADs can be better than 10 Hz for selected devices with small active areas. The dark count rate of SNSPDs is usually below 10 Hz for bias currents of 90% of the critical current.

**Dead time** is the smallest time duration after which the detection is unaffected by the previous photon detection and limits the maximum detectable photon rate. The dead time includes transition processes as they occur in SNSPDs as well as the time necessary to recover the bias voltage in SPADs. SPADs have typical dead times in the range from 25 ns to 50 ns. SNSPDs have nano-wire layout dependent dead times of usually 1 ns to 10 ns.

**Afterpulse probability** is the probability that the detector gives an electrical output signal after the initial photon detection without being triggered by further photon. This probability should be given for a certain time period after the initial time after photon absorption or as a function of that time. The after-pulse probability of SPADs is count rate dependent and typically of the order of 0.5%. SNSPDs have a afterpulse probability of zero.

**Timing jitter** is the uncertainty of the timing latency between photon detection and the electrical output signal. The jitter of free space detectors can be reduced by focussing the radiation to be detected on a certain place on the active detector

area. The timing jitter for “thick”-SPADs is of the order of 800 ps and can be as small as 40 ps for devices with a small active area. The timing jitter of SNSPDs is typically better than 55 ps.

This is a non-exhaustive enumeration that can be extended if necessary. In addition, it is important to state how these characteristics have been measured. If the characteristics are count rate dependent their value should be extrapolated to zero count rate.

## 3.2 Current Methods for Single Photon Detector Calibrations

In this section, the present state-of-the-art for single photon detector calibrations in terms of detection efficiency is briefly described. First, methods that are primary are briefly introduced and second, a method that is traceable to a primary standard is discussed.

### 3.2.1 Calibration Methods of Single Photon Detectors Without Referencing to a Primary Standard

Usually detectors are calibrated traceable to a primary detector standard, i.e. in radiometry, traceable to cryogenic radiometers. Primary calibration methods for single photon detectors, i.e. their accuracy is high enough and its value is accepted without reference to other standards of the same quantity, have gathered a lot of interest in the recent years. The latter is of special importance because many NMIs and stakeholders don't have cryogenic radiometers which is the most important primary detector standard in radiometry. The main advantage of the methods described here, i.e. the spontaneous parametric down conversion method and the quantum cloning method, is the adoption to the radiant power levels commonly used in the few photon radiometry. SPDC is accepted as a primary method.

#### Spontaneous Parametric Down Conversion

Spontaneous Parametric Down Conversion (SPDC) offers some unique possibilities, especially for traceable detector calibrations in terms of detection efficiency, that will be briefly discussed here. The SPDC has been described first by Klyshko [20] in 1967 and experimentally verified in the same year by several groups such as Magde et al. [113]. The idea to use SPDC as a radiant standard goes back more than 30 years ago [21]. It is now widely used to calibrate photodetectors in the photon counting regime. The application of this method for the calibration of classical detectors has been recently shown in [114, 115] by Brida et al. at the NMI of Italy, INRIM.

Because the SPDC is not used within the framework of this thesis, only a brief introduction is given here. For a more detailed description of SPDC, reference [116] by Hong and Mandel is recommended. The SPDC can only be described in the framework of the quantum theory as shown by Klyshko et al. [20]. In SPDC, monochromatic pumping radiation of frequency  $\omega_0$  spontaneously decays in an optical parametric process into a pair of signal (frequency  $\omega_1$ ) and idler (frequency  $\omega_2$ ) photons obeying energy and momentum conservation:

$$\hbar\omega_0 \rightarrow \hbar\omega_1 + \hbar\omega_2 . \quad (3.1)$$

The maximum decay efficiency is achieved when the phase matching condition is preserved, i.e.:

$$\Delta\mathbf{k} \equiv \mathbf{k}_1 + \mathbf{k}_2 - \mathbf{k}_0 = 0 \quad (3.2)$$

### 3.2 Current Methods for Single Photon Detector Calibrations

with the wave vector  $\Delta \mathbf{k}$  of the phase detuning,  $\mathbf{k}_0$ ,  $\mathbf{k}_2$ , and  $\mathbf{k}_1$  the wave vectors of the pumping photon, the signal photon and the idler photon, respectively. To create a bi-photon field at the output, i.e. the flux of correlated photons, the frequencies of  $\omega_1$  and  $\omega_2$  have to be in the transparency range of the scattering medium. Although the time of the creation of the photon pair is random, the two photons are created simultaneously. The polarisation states of the photon pairs are correlated, and are either the same or orthogonal, depending on the particular down conversion process employed. However, the two photons are created simultaneously and having different but fixed directions, hence, they are a great tool for the calibration of single photon detectors. If two detectors, one called “signal detector” the other called “idler detector”, are placed along the propagation direction of the photon pair, the detection of an event by one detector guarantees the presence of a photon at the conjugate detector within a given time interval  $T_g$ . For a total number of events  $N$ , the number of events recorded by the signal detector  $N_s$ , and the number of events recorded by the idler detector  $N_i$  within the time interval  $T_g$  the following relationships holds:

$$N_s = \eta_s N \quad (3.3)$$

$$N_i = \eta_i N \quad (3.4)$$

with  $\eta_{s,i}$  the detection efficiencies of the signal and of the idler detector. Then the measured number of coincidences  $N_c$  is then given by:

$$N_c = \eta_i \eta_s N . \quad (3.5)$$

The detection efficiencies of the two detectors can then be derived from:

$$\eta_s = N_c / N_i \quad (3.6)$$

$$\eta_i = N_c / N_s \quad (3.7)$$

These relations show that single photon detectors can be calibrated with this method without reference to a calibrated detector and, hence, that this method is primary. These relations only hold for an ideal setup, i.e. there are no losses in the optical path from where the photon pair is created to the detectors and that unity coupling efficiency is achieved. To calibrate single photon detectors with this method the losses in the optical path have to be measured with low uncertainties.

The uncertainties associated with the SPDC decreased from approx. 20% in 1970 to smaller than 0.20% in 2006 as described in [8]. An overview of the contributions to the uncertainty budget of a calibration of single photon detector using SPDC can be found, for instance, in [8, 117, 118, 119]. The dominant source of uncertainty of this calibration method is the determination of the optical losses.

However, progress of improving the accuracy of SPDC as a primary detector calibration has slowed down in the past years. Only a few groups, mainly at national metrology institutes, are still working on the improvement of this method while the application of this method is widely adopted among the national metrology institutes. The lowest

uncertainty when calibrating single photon detectors with SPDC has been achieved by Migdall et al. in 2007 [119] with  $u_{\text{SPDC}} = 0.18\%$ .

#### Quantum-Cloning for Absolute Radiometry

Sanguinetti et al. recently proposed a method [120] to establish a radiometric standard based on the no-cloning theorem [121]. Classical information can be perfectly copied independently on the initial quantity. This is in contrast to cloning in the quantum domain. In quantum mechanics, an arbitrary unknown quantum state cannot be copied with a fidelity of unity. In fact, the fidelity of quantum cloning is always less than unity. In the framework of quantum information, a special class of quantum states are referred to as quantum bits or qubits as the fundamental units of quantum information. Depending on the quantity of information to be cloned, the quality of quantum cloning increases with growing dimensions. It has been proved by Gisin et al. [122] that the fidelity  $\mathfrak{F}$  of cloning  $N$  to  $M > N$  identical qubits for an ideal quantum cloning machine can be derived ab initio [122] to be

$$\mathfrak{F}_{N \rightarrow M} = \frac{1 + 1/M + 1/N}{1 + 2/N} . \quad (3.8)$$

The fidelity  $\mathfrak{F}_{N \rightarrow M}$  increases rapidly to 1 for a growing number of input qubits  $N$ . This can be explained by the initial quantum information becoming classical for large  $N$ . This relation can be used to perform an absolute radiance measurement by exploiting the quantum to classical transition of  $\mathfrak{F}_{N \rightarrow M}$ . As shown in [120], the number of input photons per mode  $\mu_{\text{in}}$  is then given by

$$\mu_{\text{in}} = \frac{2\mathfrak{F} - 1}{1 - \mathfrak{F}} . \quad (3.9)$$

The radiant power can be obtained from (3.9) by measuring the number of modes per unit time. For an optimal quantum cloning machine of input polarisation photonic qubits  $\mathfrak{F}$  is given by the overlap between input and output polarisations [120]:

$$\mathfrak{F} = P_{\parallel} / (P_{\parallel} + P_{\perp}) \quad (3.10)$$

where  $P_{\parallel}$  and  $P_{\perp}$  are the output radiant power of the radiation polarised parallel and perpendicular to the input polarisation. Hence,  $\mathfrak{F}$  can be obtained from purely relative measurements. The radiometer developed by Sanguinetti et al. works in the range from single photons to  $10^{11}$  photons per second and can be build as an all-fibre radiometer [123]. At this time the “quantum cloning” method suffers from achievable uncertainties in the small percentage range limited by the uncertainty contribution of the measurement of the polarisation states [120]. The feasibility of this method is investigated at PTB in the division of optics to possibly become a radiometric standard in the few photon regime.

### 3.2.2 Calibration Method of Single Photon Detectors Referencing to a Primary Standard

Cryogenic radiometers, the most advanced primary detector standards in radiometry, are not suitable for measurements in the few photon regime when other properties than the mean radiant power are of interest because they operate at time scales of minutes. As described in chapter 2, the electrical substitution principle is more suitable for radiant powers in the  $\mu\text{W}$  regime or higher. The difference in the heater power necessary to maintain a constant cavity temperature with and without optical radiation, measured to obtain the radiant power, decreases with the radiant power. This leads to increased uncertainties caused by electrical noise as both heater power levels decrease and become more and more equal with reduced photon fluxes. However, the high temporal stability and scalability of the detectable radiant power makes cryogenic radiometers promising candidates for primary detector standards in the few photon regime as well. Low radiant power cryogenic radiometers are subject of research at the National Physics Laboratory (NPL) [124] and the National Institute of Standards and Technologies (NIST) [125]. In the group of John Lehman at NIST, absorbers for cryogenic radiometers based on carbon nanotubes have been tested at radiant power levels below 10 nW [126]. Absorbers based on carbon nanotubes can be tailored to the desired optical specifications and reflectances as low as 0.045 % have been reported [127, 128]. With these optical properties, smaller absorber structures can be used that provide higher sensitivity to expand the feasibility of thermal detectors into the few photon regime. However, the most common calibration method of single photon detectors traceable to a primary standard is the substitution method described below.

#### The Substitution Method

The substitution method is the classical calibration method for single photon detectors. Here, the radiant power, and, thus, the photon rate, is measured at a low photon flux with a reference detector traceable to a primary detector standard. At the same photon flux the count rate of the single photon detector, i.e. the DUT, is measured in order to obtain the detection efficiency of the DUT. The photocurrent of the reference detector, usually based on photodiodes, is amplified by several orders of magnitude with a transimpedance amplifier. Usually tungsten halogen lamps with a current stabilised power supply are used as radiation sources. The desired wavelength can be chosen with interference filters and the attenuation of the radiant power, down to the few photon regime, can be performed with neutral density filters. An integrating sphere can be included to provide a uniform patch of light at the outputs of the integrating sphere. The detection efficiency of the DUT can be obtained from the radiant power measured with the calibrated detector and the count rate of the DUT using the relation:

$$DE_{\text{DUT}}(\lambda) = \frac{S(\lambda) \cdot G \cdot CR}{V_{\text{out}}} \cdot E_{\text{phot}} \quad (3.11)$$

### 3 Bridging the Radiometric Gap

with  $DE_{\text{DUT}}(\lambda)$  the detection efficiency of the DUT at the wavelength  $\lambda$ ,  $S(\lambda)$  the spectral responsivity of the calibrated reference detector,  $G$  the gain of the transimpedance amplifier,  $CR$  the count rate of the DUT,  $V_{\text{out}}$  the output voltage of the transimpedance amplifier, and  $E_{\text{phot}}$  the photon energy. A detailed description of calibrations of single photon detectors with the substitution method can be found in [12] and [129].

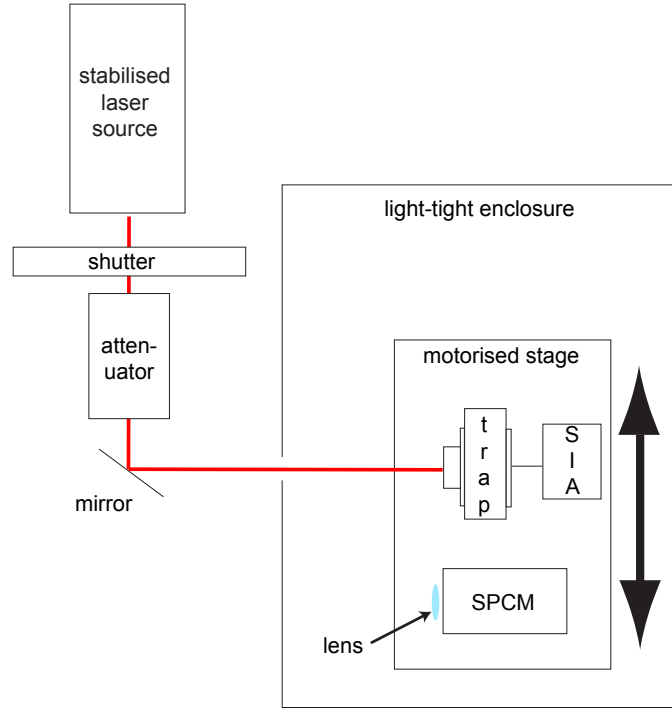
Within the “Candela” project, a Perkin-Elmer single photon counting module (SPCM), which uses a SPAD as detecting element, has been calibrated with the substitution method as a corporation between colleagues from INRIM, providing the SPCM, PTB, providing the high stable laser source described in chapter 2.2 and the measurement facility, CMI, providing a new type of transimpedance amplifier called switched integrator amplifier [130], NPL, providing the calibrated trap detector, and METROSERT, providing a high quality optical attenuator [131, 132]. A schematic of the calibration setup is shown in Figure 3.3. The laser radiation was attenuated with a newly developed ten-element transmission trap detector [131, 132] down to a power level of approximately 1 pW. This detector was also used to monitor the laser power. The radiant power of the laser was then measured with the calibrated and cooled trap detector and sequentially the count rate of the SPCM was measured. Cooling the trap detector to a temperature of  $\approx 15^\circ\text{C}$  reduces the noise floor of the detector by several orders of magnitude. A measurement sequence included the measurement of the detector output of the reference trap detector and SPCM with and without laser radiation. The result of a measurement run is shown in Figure 3.4. The output voltage and the count rate have been obtained by subtracting the detector output without laser radiation.

The most dominant contributions to the uncertainty budget of the calibration of a SPCM by means of the substitution method are the standard deviation of the photocurrent of the reference detector and the uncertainties associated with the different detector sizes of reference detector and SPCM. The high count rates introduce a high thermal load to the SPCM which affects the afterpulse and dark count probability as well as the dead time. These parameters need to be measured with a low uncertainty in order to achieve a low combined relative standard uncertainty of the detection efficiency of the DUT.

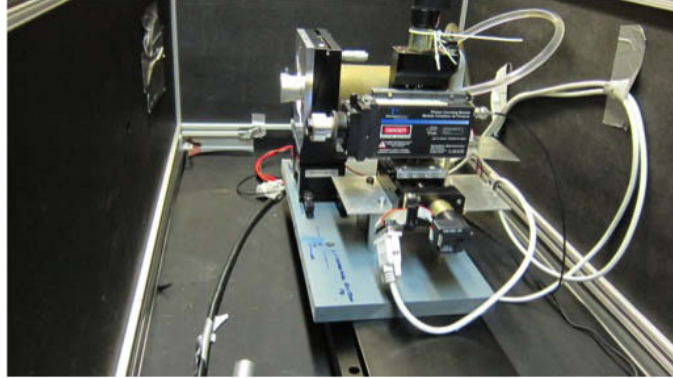
The active areas of typical classical detectors like photodiodes are usually several millimetres in diameter while single photon detectors are very small in comparison with classical detectors. A typical SPAD has an active diameter of 100  $\mu\text{m}$  or less. Assuming a gaussian intensity distribution, the extension of the optical field is infinite. Hence, considerations of the influence of the detector sizes on the measured detection efficiency are mandatory. If a single photon detector is calibrated by comparing, e.g., the photocurrent of a 10 mm diameter photodiode and the count rate of a 100  $\mu\text{m}$  active diameter single photon detector one has to assure that the whole radiation that was detected with the large classical detector is also detected by the single photon detector. Three approaches to overcome the detector size issue are commonly followed:

1. Using calibrated lenses in front of the single photon detector [133].
2. Calibrating a unit of single photon detector and lens. This approach was followed in this work to apply the substitution method [134].

### 3.2 Current Methods for Single Photon Detector Calibrations



(a)



(b)

Figure 3.3: Schematic of the setup (Figure 3.3(a)) and photograph of the inside of the light-tight enclosure (Figure 3.3(b)) used to calibrate a Single Photon Counting Module (SPCM) with attenuated laser radiation. Both detectors, trap detector (trap) in connection with the switch integrator amplifier (SIA) and SPCM, are mounted on a translation stage that allows the irradiation of the detectors at the same position with the same radiant power. The lens in front of the SPCM is necessary to achieve an under-filling of the active area of the SPCM with the laser radiation.

3. Correcting for the optical losses when the single photon detector is not perfectly under-filled. This approach was followed to calibrate free space single photon detectors by means of synchrotron radiation [13] as described in chapter 3.3.1.

A standard uncertainty of 0.2% has been achieved [134] for the calibration of the SPCM in conjunction with a lens in front of the active area by means of the substitution method within the “Candela” project. However, a detailed uncertainty budget could not be compiled for this thesis because the uncertainty contributions of the devices provided by the partners were not available. A brief description of the results and a comparison with calibration results of the same SPCM obtained with the SPCM method can be found in reference [134]. The resulting uncertainty was limited by the standard deviation of the photocurrent measured with the reference trap detector [134]. Most remarkable in this experiment was the employment of a switched integrator current amplifier [130] which is capable of measuring the photocurrent from  $3 \times 10^5$  photons per second with an uncertainty of 0.1% [129]. Furthermore, the measured detection efficiency agreed with the result obtained from a calibration by means of the SPDC within the uncertainty of the SPDC calibration of 0.3% [134]. The lowest uncertainty for a calibration using the substitution method has been achieved by Polyakov et al. with 0.17% [12].

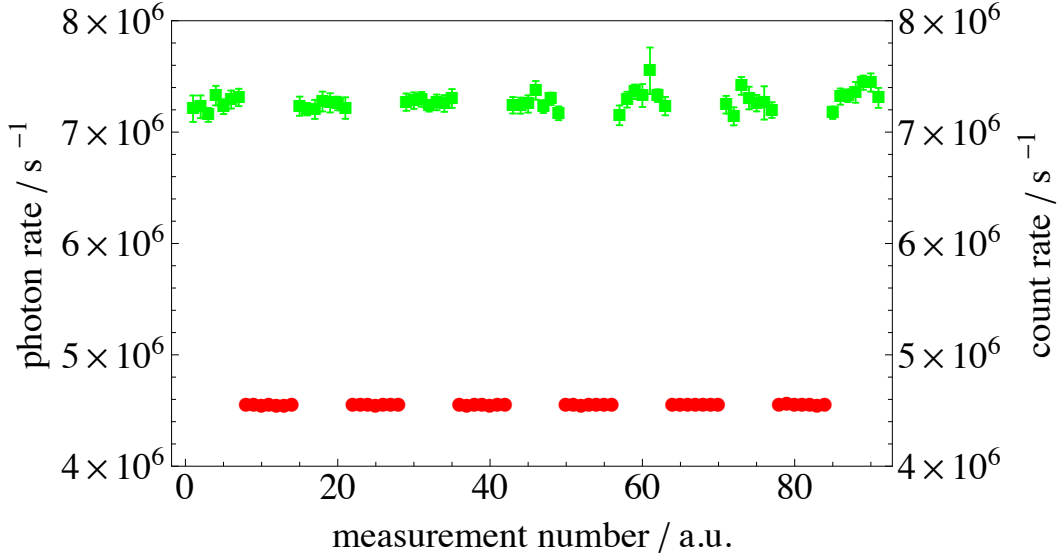


Figure 3.4: Result of a measurement sequence containing several measurements of the photon rate with the reference trap detector (green squares) and several photon counting measurements with the SPCM (red circles). The uncertainty bars of the photon counting measurements are smaller than the red circles.

### 3.3 Bridging the Radiometric Gap with Synchrotron Radiation

The efforts within the “Candela” project to create photon based standards for the few photon radiometry inspired the involved people at PTB, to use the unique possibilities of the division “7. Temperature and Synchrotron Radiation” to bridge the radiometric gap by exploiting the properties of synchrotron radiation. In the division 7, primary detector standards for radiant power measurements, i.e. cryogenic radiometer, are operated as well as the primary source standard Metrology Light Source, which has the necessary equipment for this task installed, with a dynamic range of the emitted spectral radiant power of 11 orders of magnitude. The strict proportionality of emitted radiation and the number of stored electrons of an electron storage ring provides a unique possibility to bridge the radiometric gap by means of synchrotron radiation [15, 16]. With these two tools, a calibration chain traceable to the CR can be established that can be used to validate the SPDC and substitution method. This synchrotron radiation based method can be applied to free space and fibre-coupled detectors. The development of the fibre-coupled setup was done within the framework of the European Metrology Research Programme joint research project “Metrology for Industrial Quantum Communication Technologies” (MIQC) aiming to establish standards for quantum key distribution systems.

#### 3.3.1 Introduction to Synchrotron Radiation based Source Standards

There are, at this time, about 70 synchrotron radiation sources in operation. The operation principle of electron storage rings dedicated for producing synchrotron radiation is, for instance, described in [135]. The spectral photon flux  $\Phi_E$  through an aperture can be calculated from storage ring parameters and geometrical quantities by means of the so-called Schwinger equation [136]. The feasibility of electron storage rings to serve as calculable radiation sources, i.e., as primary source standards, was recognised in 1959 [137]. The three most important synchrotron radiation based primary source standards in operation today, given in alphabetical order, are:

- BESSY II is a third generation storage ring located in Berlin-Adlershof where the PTB operates a radiometry laboratory [138]. The operation of BESSY II started in 1998. BESSY II covers the short-wavelength spectral ranges from the EUV to the X-ray range.
- Metrology Light Source (MLS) is the electron storage ring (third generation) of the PTB dedicated to metrology [138] located in Berlin-Adlershof in operation since spring 2008. The MLS covers the spectral range from the far infrared / THz to the extreme ultraviolet (EUV). The MLS has been used in this work to bridge the radiometric gap in the transition from the classical radiometry to the few photon radiometry.
- SURF III is a dedicated electron storage ring [139, 140] of the National Institute

### 3 Bridging the Radiometric Gap

of Standards and Technology (NIST) located in Gaithersburg, MD USA. It has been upgraded from SURF II to SURF III in 1998.

The term “third generation” describes dedicated facilities that were built to support the implementation of, so-called, insertion devices such as wigglers and undulators. Synchrotron radiation covers a tremendously larger spectral range than blackbody radiation sources. Figure 3.5 shows the calculated spectral radiant powers of the primary source standards BESSY II, the MLS and a blackbody with a temperature of 3000 K which is close to the upper temperature limit of blackbodies. Although the MLS has not been used as an absolute source standard in this work, a part of the instrumentation, necessary for the operation as a primary source standard, was required to bridge the radiometric gap with synchrotron radiation. To operate a synchrotron radiation source

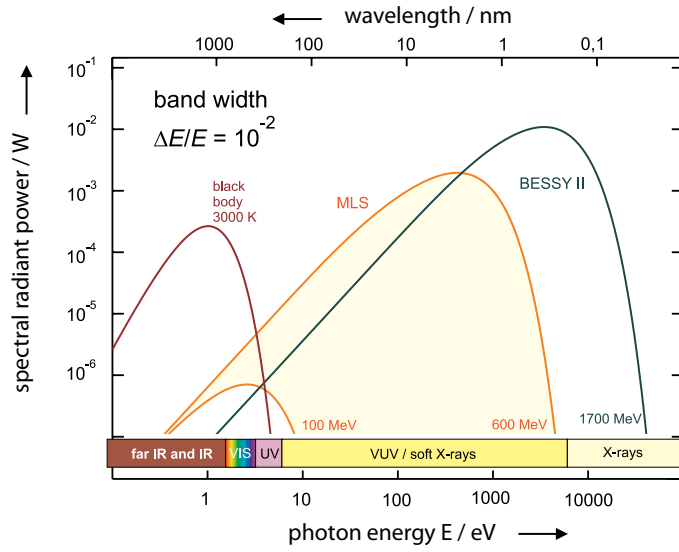


Figure 3.5: Calculated spectral radiant power of synchrotron radiation sources used by PTB as primary source standards with different characteristic photon energies compared with a blackbody radiator [138].

as primary source standard all parameters entering the Schwinger equation have to be known. The operation of the Metrology Light Source as a primary source standard is described in detail in [22].

The emitted radiation of an electron storage ring can be calculated analytically with the Schwinger theory [136] when the operation parameters of the electron storage ring are known. The spectral radiant power  $\Phi_{\lambda}^{\text{Schwinger}}$  for a photon wavelength  $\lambda$  can be expressed as [22]:

$$\Phi_{\lambda}^{\text{Schwinger}} = \Phi_{\lambda}(E, W, B, I, \Sigma_y, \Psi, d, a, b) \quad (3.12)$$

with the parameters:  $W$  the electron energy,  $B$  the magnetic induction at the radiation source point,  $I$  the electron current in the ring,  $\Sigma_y$  the effective vertical source size,  $\Psi$  the vertical emission angle, and the distance between the radiation source point and

### 3.3 Bridging the Radiometric Gap with Synchrotron Radiation

the photon flux defining aperture with dimensions  $a \times b$ . How these parameters are determined at the MLS is shown in [22] and at BESSY II in [141].

For  $N$  stored electrons the emitted spectral radiant power can be written as

$$\Phi_\lambda(\lambda, N) = N\Phi_\lambda^{Schwinger}(\lambda, 1e^-)(1 + \varepsilon(\lambda)) \quad (3.13)$$

where the number of stored electrons  $N$  is linked to the ring current  $I_{ring} = Ne^-\nu$ , with  $e^-$  the elementary charge and  $\nu$  the revolution frequency of the electrons. The factor  $\varepsilon$  accounts for the vertical source size of the stored electron bunches. This parameter considers the spread of the stored electrons and the resulting deviation from a perfect circular orbit. The stored electrons show a small deviation from a perfect orbit with space related standard widths of  $\sigma_x$  and  $\sigma_y$  and angular deviations of  $\sigma_{x'}$  and  $\sigma_{y'}$  [22]. Due to the tangential observation, the horizontal spread is of no importance but the vertical spread leads to an effective divergence  $\Sigma_{y'}$  at the aperture stop in front of the experiment. This has to be taken into account as a convolution over the vertical emission angle  $\Psi$ . This correction factor is smaller than  $10^{-4}$  for wavelengths longer than 200 nm at the MLS. A detailed description of this correction is given in [142, 143, 144]. However, this parameters had to be taken into account when the electron bunches were imaged on small single photon detectors and optical fibres.

The direct proportionality of the number of stored electrons  $N$  and emitted spectral radiant power is valid as long as the emitted wavelengths are shorter than the stored electron bunches. At the Metrology Light Source, the ring current can be varied from  $\approx 1$  pA (one stored electron) to about 200 mA, i.e. by eleven orders of magnitude, in a controlled way without changing spectral distribution of the emitted spectrum [22]. The biggest challenge is the precise measurement of the ring current and, thus, the number of stored electrons over 11 orders of magnitude. At the Metrology Light Source the ring current is grouped into three categories, the high, the mid, and the low ring current range. In the high ring current range, i.e. above 1 mA, two parametric current transformers (PCTs, made by Bergoz, Crozet, France) are used to measure the ring current. With these devices, the ring current can be measured with an uncertainty as low as  $\approx 0.02\%$ .

In the low ring current regime, i.e. below 1 nA, the ring current is determined by counting the stored electrons. To count the stored electrons, the photocurrent of two cooled windowless Si-photodiodes, that are irradiated with the synchrotron radiation, is measured continuously. When one or more electrons are dropped out of the ring, step-like drops of the photocurrent appear (see Figure 3.10). After the experiment, the ring current is slowly reduced until all stored electrons are removed. The number of stored electrons during the experiments can then be determined by counting the steps in the photocurrent of the photodiodes. The uncertainty of the ring current measurement in the low current regime is dominated by the uncertainty of the measurement of the revolution frequency which is about  $1 \times 10^{-7}$ .

In the mid current range, i.e. between 1 mA, and 1 nA, windowless Si photodiodes with filters in front of the active area are used to measure the ring current. The calibration factors of these photodiodes are obtained from the measurements of the ring current

in the low and high ring current range. The uncertainty achievable in the mid current range is limited by the linearity of the photodiodes and is of the order of 2%. However, close to 1 mA and 1 nA, i.e. close to the overlap of the high and mid current range and the mid and low current range, uncertainties smaller than 2% of the measurement of the ring current with the photodiodes can be achieved.

Furthermore, the uncertainty of the ring current measurement in the high and mid current range is dependent on the actual experimental conditions. A detailed description of the ring current measurement of the Metrology Light Source can be found in [145].

The unique properties of the synchrotron radiation from the Metrology Light Source [22, 138, 145] are used in this work to perform the calibration of two single photon avalanche diodes (SPADs) (further named SPAD1 and SPAD2) and a superconducting nanowire single photon detector (SNSPD) traceable to a cryogenic electrical substitution radiometer.

#### 3.3.2 Determination of the Photon Statistics of the Metrology Light Source

As mentioned before, the response of single photon detectors to photons is different from that of classical detectors. Especially as classical detectors give an output proportional to the radiant power averaged over the observation time while single photon detectors give an output signal for each event caused by the absorption of one or more photons. In most cases, the output signal of single photon detectors, related to a particularly detected event, is independent of the number of absorbed photons. Thus, a classical detector measures the radiant power while single photon detectors count events containing one or more photons. The single photon detectors to be calibrated here are non-photon number resolving detectors, i.e., since the Metrology Light Source is no single photon source the measured count rate has to be corrected for detected events that contained two or more photons. However, the probability that a pulse emits more than 3 photons is negligible in the low ring current regime. Hence, the correction factor  $c_{st}$  can be approximated by  $c_{st} = 1 + (p_2 + p_3)p_1^{-1}$ , with the probabilities  $p_1$ ,  $p_2$ ,  $p_3$  that the pulses contain one, two or three emitted photons. However, the photon statistics has to be known to obtain  $c_{st}$ . The photon statistics of synchrotron radiation has been investigated, especially for X-rays, for instance in [146, 147, 148, 149, 150]. The photon statistics of the emitted synchrotron radiation has been determined to obey a thermal distribution, Poisson distribution or a mix of the both distributions depending on the experimental conditions. To identify the appropriate correction terms for the photon statistics, the photon count distribution is briefly derived. A detailed derivation can be found in [151]. If radiation of intensity  $I(t)$  falls on a photon counter the probability  $\Delta p$  that a count occurs is given by

$$\Delta p(t) = \alpha I(t) dt \quad (3.14)$$

with the sensitivity of the detector  $\alpha$  that depends on the area of the detector and the wavelength. For the case that there are no random fluctuation in the intensity  $I(t)$  the probability that no count occurs in the time interval  $dt'$  at time  $t'$  is given by  $1 - \Delta p(t')$ . If we use the assumption that photo-counts in different time intervals are independent

### 3.3 Bridging the Radiometric Gap with Synchrotron Radiation

it can be shown [151] that the probability to detect  $n$  photons in the time interval  $t$  to  $t + T$  is given by

$$P_n(t, T) = \frac{1}{n!} [\alpha T \bar{I}(t, T)]^n \exp[-\alpha T \bar{I}(t, T)] , \quad (3.15)$$

with the mean intensity during the counting interval

$$\bar{I}(t, T) = \frac{1}{T} \int_t^{t+T} I(T') dt' . \quad (3.16)$$

As the intensity  $\bar{I}(t, T)$  may vary from one counting interval to another it is more useful to use the time average  $P_n(T)$  of  $P_n(t, T)$  over a large number of different starting times.  $P_n(T)$  can be expressed as [152]

$$P_n(T) = \langle P_n(t, T) \rangle \quad (3.17)$$

$$= \left\langle \frac{[\alpha \bar{I}(t, T) T]^n}{n!} \exp[-\alpha \bar{I}(t, T) T] \right\rangle . \quad (3.18)$$

In the case of constant intensity  $\bar{I}(t, T) = I$  no averaging is necessary and

$$P_n(T) = \frac{\bar{n}^n}{n!} \exp(-\bar{n}) , \quad (3.19)$$

and

$$\bar{n} = \alpha I T . \quad (3.20)$$

This is a Poisson distribution for which the variance  $V(n)$  is equal to  $\bar{n}$ .

For fluctuating intensities, i.e. thermal radiation, as it occurs for synchrotron radiation, (3.15) can be simplified in the limit that the counting time  $T$  is short compared to the time where the intensity changes due to losses of electrons inside the storage ring. If  $I(t)$  remains reasonably constant during the time interval  $T$  then

$$\bar{I}(t, T) = \bar{I}(t) . \quad (3.21)$$

As derived in [151] (3.18), can be written as

$$P_n(T) = \int_0^\infty \frac{[\alpha \bar{I}(t) T]^n}{n!} e^{-\alpha \bar{I}(t) T} p(\bar{I}(t)) d\bar{I}(t) . \quad (3.22)$$

The probability distribution of the intensity of a thermal radiation field is given by

$$p(I) = \frac{1}{I_0} \exp\left(\frac{-I}{I_0}\right) , \quad (3.23)$$

with  $I_0$  the average intensity and moment  $\langle I^n \rangle = n! I_0^n$ . The variance and mean of the photon count distribution are  $V(n) = \bar{n}(1 + \bar{n})$  and  $\bar{n} = \alpha T I_0$ .

### 3 Bridging the Radiometric Gap

The photon count distribution then becomes

$$P_n(T) = \frac{1}{(1 + \bar{n})} \left( \frac{\bar{n}}{1 + \bar{n}} \right)^n . \quad (3.24)$$

With these photon count distributions of coherent and thermal radiation given in (3.19) and (3.24) the measured count rate can be corrected if the photon statistic of the Metrology Light Source for the measurement condition is known. As shown in Figure 3.6, the photon statistics correction  $[p(2)+p(3)]p(1)^{-1}$  can heavily influence the calibration result. Furthermore, for rates above 500000 photons/s, it would become the major uncertainty contribution for this calibration method if the photon statistic is unknown.

To obtain the photon count distribution of the synchrotron radiation for the given experi-

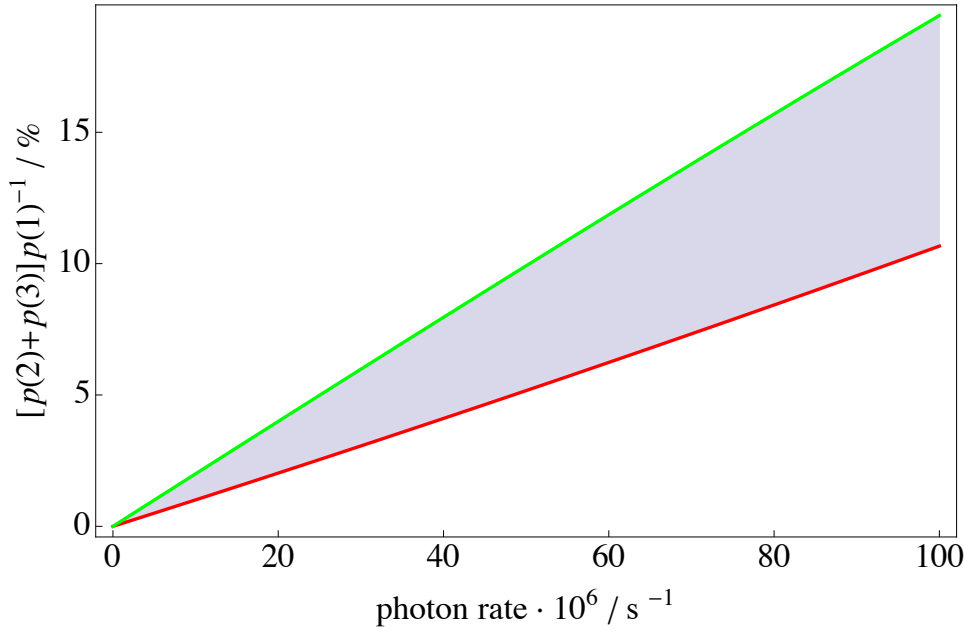


Figure 3.6: Photon statistic correction  $[p(2) + p(3)]p(1)^{-1}$  plotted over the photon rate of the Metrology Light Source for the assumptions, thermal radiation (green line) and coherent radiation (red line).

mental conditions, the  $g^{(2)}$ -function, i.e. the intensity correlation function of the Metrology Light Source, was measured with SNSPDs (see chapter 3.1). The  $g^{(2)}$ -function is derived for instance in [151] where the approach of Glauber [153] is followed. To describe intensity correlation measurements, it is necessary to define higher-order correlation functions. The  $n^{th}$ -order correlation function for electromagnetic fields is defined as [151]

$$G^{(n)}(x_1 \dots x_n, x_{n+1} \dots x_{2n}) = Tr\{\rho \hat{E}^{(-)}(x_1) \hat{E}^{(+)}(x_n) \times \hat{E}^{(-)}(x_{n+1}) \hat{E}^{(+)}(x_{2n})\} . \quad (3.25)$$

### 3.3 Bridging the Radiometric Gap with Synchrotron Radiation

Here,  $\hat{E}^{(+)}$  and  $\hat{E}^{(-)}$  are operators that represent the positive/negative frequency part of the quantised electro-magnetic field. Thus, the correlation of the field at the space-time point  $x = (\mathbf{r}, t)$  and the field at the space-time point  $x' = (\mathbf{r}', t')$  can be written as the correlation function

$$G^{(1)} = Tr\{\rho \hat{E}^{(-)}(x) \hat{E}^{(+)}(x')\} . \quad (3.26)$$

The density operator  $\rho$  defined as

$$\rho = \sum_i P_i |i\rangle \langle i| \quad (3.27)$$

with probabilities  $P_i$  and the discrete basis functions  $|i\rangle$ . With the first-order correlation function for the radiation field, classical interference experiments can be explained. The possibility to produce interference fringes when two optical fields are superposed is given when  $G^{(1)}(x_1, x_2) > 0$  and, thus, the larger  $G^{(1)}(x_1, x_2)$  gets the more the interference fringes become visible. The maximum magnitude of  $G^{(1)}(x_1, x_2)$  is given by the relation

$$|G^{(1)}(x_1, x_2)| \leq [G^{(1)}(x_1, x_1) G^{(1)}(x_2, x_2)]^{1/2} . \quad (3.28)$$

With the normalised correlation function

$$g^{(1)}(x_1, x_2) = \frac{G^{(1)}(x_1, x_2)}{[G^{(1)}(x_1, x_1) G^{(1)}(x_2, x_2)]^{1/2}} \quad (3.29)$$

and  $\mathbf{r}(x_1) = \mathbf{r}(x_1)$  and  $\tau = (t_2 - t_1)$  the coherence can be defined as

$$|g^{(1)}(\tau)| = \begin{cases} 1 & \text{coherent.} \\ 0 < \dots < 1 & \text{partially coherent.} \\ 0 & \text{incoherent.} \end{cases} \quad (3.30)$$

While  $g^{(1)}(0) = 1$  for all fields, the time  $\tau$  where  $|g^{(1)}(\tau)|$  equals one is named coherence time  $\tau_c$ .

The second-order correlation function  $G^{(2)}$  is given by

$$G^{(2)}(\tau) = \langle \hat{E}^{(-)}(t) \hat{E}^{(-)}(t + \tau) \hat{E}^{(+)}(t + \tau) \hat{E}^{(+)}(t) \rangle \quad (3.31)$$

$$= \langle : \hat{I}(t) \hat{I}(t + \tau) : \rangle \quad (3.32)$$

with  $:$  indicating normal ordering and the intensity  $\hat{I}(t)$ . To evaluate this quantity, the normalised second-order correlation function is used

$$g^{(2)}(\tau) = \frac{G^{(2)}(\tau)}{|G^{(1)}(0)|^2} . \quad (3.33)$$

For coherent states  $g^{(2)}(\tau)$  holds:

$$g^{(2)}(\tau) = 1 \quad (3.34)$$

### 3 Bridging the Radiometric Gap

for all times  $\tau$ . Thus, the photons are uncorrelated which is in agreement with the probability distribution of coherent states being a Poisson distribution. In addition, this result shows that coherent states don't show intensity fluctuations. For fluctuating classical fields it is useful to introduce a probability distribution  $P(\varepsilon)$  which describes the probability that the classical field  $E^{(+)}(\varepsilon, t)$  has the amplitude  $\varepsilon$

$$E^{(+)}(\varepsilon, t) = - \left( i \frac{\hbar \omega}{2\varepsilon_0 V} \right)^{1/2} \varepsilon e^{i\omega t} \quad (3.35)$$

with the  $V$  the mode volume.

For zero time delay,  $\tau = 0$ , the single-mode field can be written as

$$g^{(2)}(0) = 1 + \frac{\int P(\varepsilon)(|\varepsilon|^2 - \langle |\varepsilon|^2 \rangle)^2 d^2\varepsilon}{(\langle |\varepsilon|^2 \rangle)^2} . \quad (3.36)$$

As the probability distribution  $P(\varepsilon)$  is positive for classical fields it follows that  $g^{(2)}(0) \geq 1$ .

For fields obeying a Gaussian distribution with zero mean amplitude (3.32) becomes

$$G^{(2)}(\tau) = G^{(1)}(0)^2 + |G^{(1)}(\tau)|^2 \quad (3.37)$$

which is equal to

$$g^{(2)}(\tau) = 1 + |g^{(1)}(\tau)|^2 \quad (3.38)$$

Here  $G^{(1)}(\tau)$  is the Fourier transform of the spectrum of the field (Wiener-Khintchine-Theorem [154, 155])

$$S(\omega) = \int_{-\infty}^{\infty} d\tau e^{-i\omega\tau} G^{(1)}(\tau) . \quad (3.39)$$

For a field with a Lorentzian spectrum  $g^{(2)}(\tau)$  becomes

$$g^{(2)}(\tau) = 1 + e^{-\gamma\tau} \quad (3.40)$$

and for a field with a Gaussian spectrum

$$g^{(2)}(\tau) = 1 + e^{-\gamma^2\tau^2} . \quad (3.41)$$

For  $\tau \gg \tau_c$  the correlation time of radiation  $g^{(2)}(\tau) \rightarrow 1$ . For  $\tau \ll \tau_c$  the value of  $g^{(2)}(\tau)$  for chaotic light is increased over coherent light

$$g^{(2)}(0)_{\text{chaotic}} = 2 \cdot g^{(2)}(0)_{\text{coherent}} \quad (3.42)$$

due to the intensity fluctuations in the chaotic radiation field. This was first experimentally observed by Hanbury-Brown and Twiss [156]. In the photon interpretation of electromagnetic fields, classical intensity fluctuations are referred to as photon bunching. Thus, the photon statistic of the Metrology Light Source can be directly derived from a measurement of  $g^{(2)}(0)$ . To correct for the photon statistics of the Metrology Light

### 3.3 Bridging the Radiometric Gap with Synchrotron Radiation

Source, a thermal statistic is assumed [157]. However, the thermal behaviour of the emitted radiation is expected to be weakened because the pulse width of the synchrotron radiation is longer than the longitudinal coherence length of the beam. In addition, the cross section of the beam is larger than the transverse coherence length. Taking these effects into account, the estimated value  $g_e^{(2)}(0)$  for  $g^{(2)}(0)$  is given by [157]

$$g_e^{(2)}(0) = 1 + F(\pi^{1/2}d_x/l_x)F(\pi^{1/2}d_y/l_y)\tau_c/\tau_p \quad (3.43)$$

with  $l_x$  and  $l_y$  the transverse coherence widths in vertical and horizontal direction,  $d_{x,y}$  the dimensions of the entrance optics of the fibre coupling setup for the SNSPDs,  $\sigma_{x,y}$  the standard deviation of the Gaussian source size,  $\lambda$  the wavelength,  $D$  the distance between source and detector,  $\tau_c$  the coherence time of the beam,  $\tau_p$  the pulse width of the synchrotron radiation with  $\tau_c \ll \tau_p$  and

$$F(b) = (2/b) \int_0^b e^{-u^2} du - (1 - e^{-b^2})/b^2, \quad (3.44)$$

$$l_{x,y} = \lambda D / 2\pi^{1/2} \sigma_{x,y}. \quad (3.45)$$

For both wavelengths, 1.55  $\mu\text{m}$ , where the photon statistics was measured and the SNSPD was calibrated, and 650 nm, where the SPADs were calibrated, (3.43) gives  $g_e^{(2)}(0) = 1.006$ .

The measurement of the photon statistic was performed at a wavelength of 1.55  $\mu\text{m}$  and not at 650 nm because a possible thermal behaviour of the emitted radiation is expected to be more easily detectable at longer wavelengths. To measure  $g^{(2)}(0)$  the synchrotron radiation was monochromatised with an interference filter with a central wavelength of 1551.97 nm and was coupled into an optical fibre. A fibre-coupled beam splitter with a splitting ratio of 50/50 was used to irradiate two SNSPDs with the synchrotron radiation (see Figure 3.7(a)). The two SNSPDs were connected with the start and stop input of a coincidence counter (Picoharp 300, Picoquant), respectively. This setup was used to measure the coincidences in a certain time window. To reduce the influence of the dead time of the detectors and the coincidence counter as well as to increase the separation of the measured coincidence peaks the number of electron bunches has been reduced from eighty to ten, i.e., the temporal separation of the bunches has been increased from 2 ns to 16 ns. Figure 3.7(b) shows the resulting coincidences. Synchrotron radiation is non-stationary. The systematical temporal evolution due to the bunched structure contributed to a large amount of trivial correlation [148] in the measurement of  $g^{(2)}(\tau)$  as shown in Figure 3.7. The measured value of  $g^{(2)}(0)$  without normalisation is 1.13 (see also Figure 3.7(b)), i.e. the thermal behaviour of the radiation is enhanced by a factor of about 20 as compared to the estimated value  $g_e^{(2)}(0) = 1.006$ . Thus, the measured coincidences have to be normalised by using a synchrotron radiation pulse from the same electron bunch to start trigger the initial coincidence measurement and the normalisation coincidence measurement using an additional coincidence counter (Picoharp 300, Picoquant) delayed by one revolution of the ring [157] as shown in Figure 3.8(a). The measured value with normalisation of  $g^{(2)}(0)$  of  $1.0049 \pm 0.0008$  (see Figure 3.8(b)) is

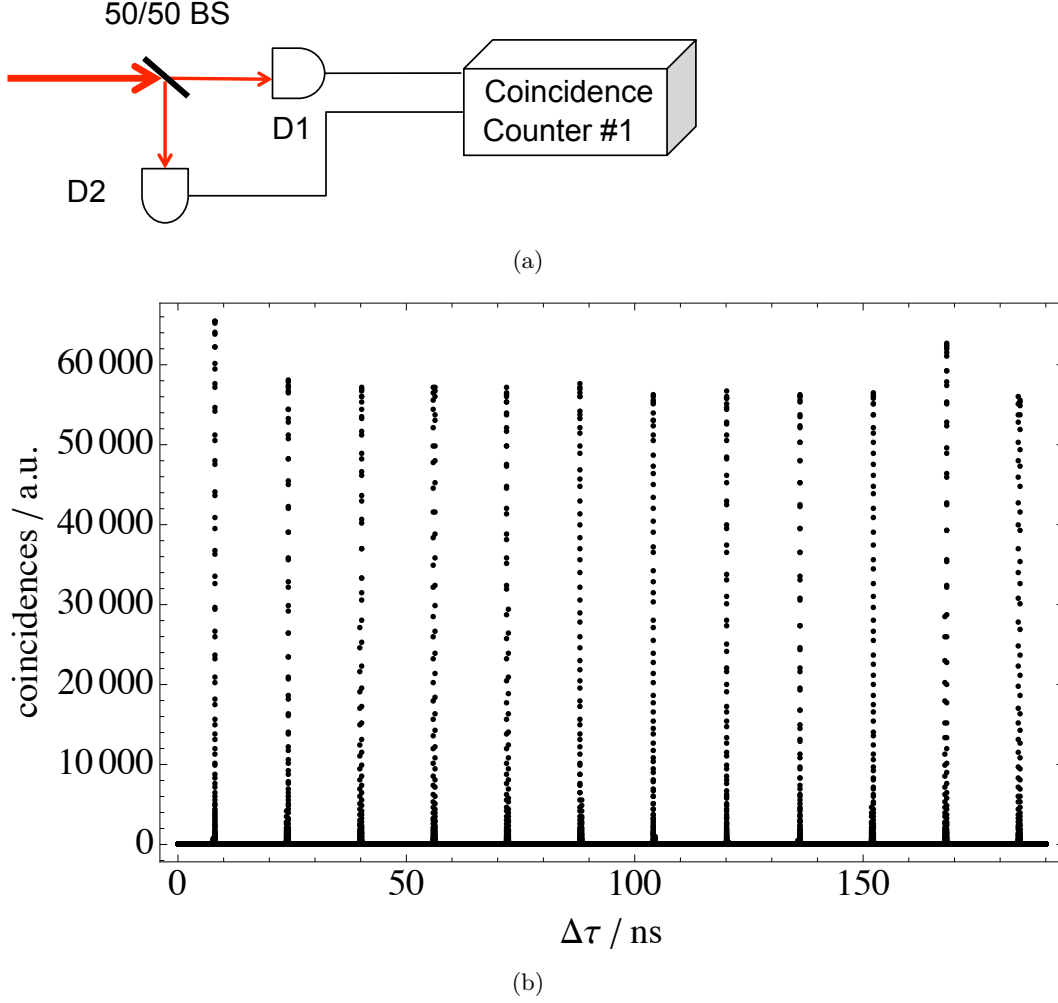


Figure 3.7: Schematic of the setup to measure the coincidence rate of the synchrotron radiation (Figure 3.7(a)) and the resulting number of coincidences (Figure 3.7(b)). The spectrally filtered radiation of the Metrology Light Source has been fed into a fibre-coupled Hanbury-Brown and Twiss setup (HBT) [156] with the detectors D1 and D2. The schematic shows the fibre-coupled beamsplitter with a splitting ratio of 50/50 (50/50 BS), the two SNSPDs (D1 and D2), and the coincidence counter. The systematical temporal evolution of the bunch structure of the synchrotron radiation introduces a high amount of, so-called [150], trivial correlation. The measured value of  $g^{(2)}(0)$  without normalisation is 1.13, i.e. significantly higher than the estimated value  $g_e^{(2)}(0) = 1.006$ .

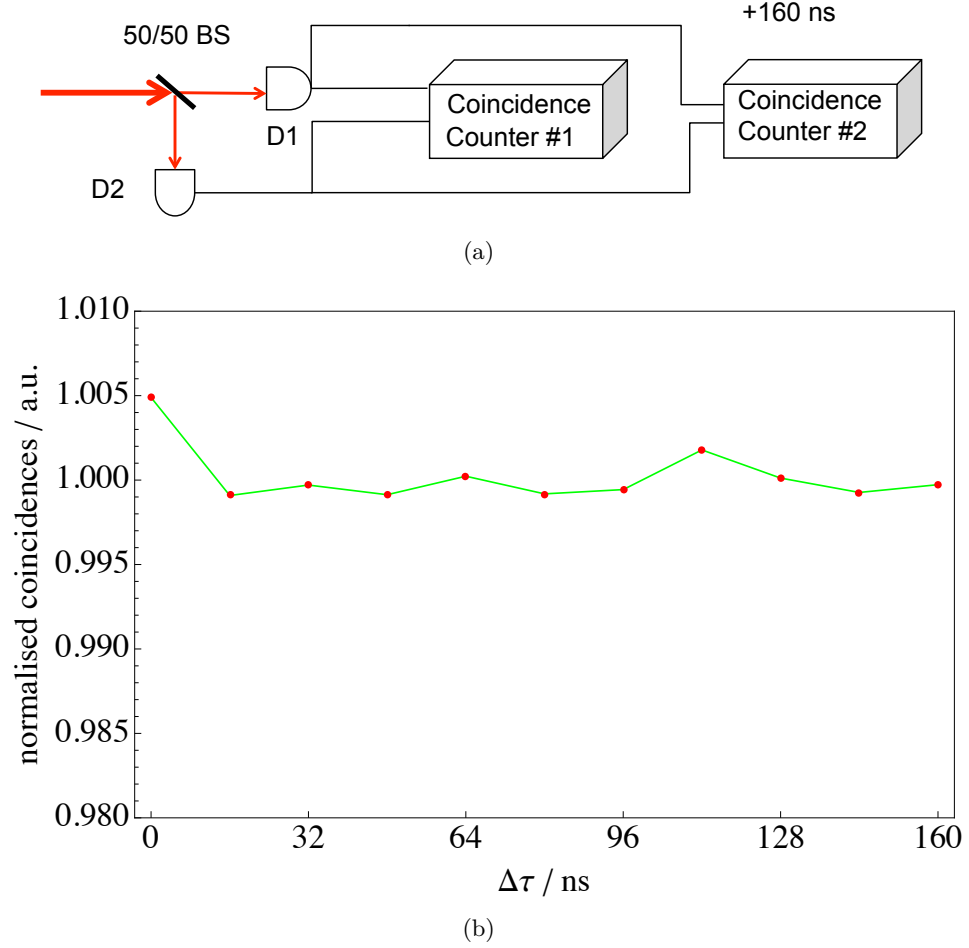


Figure 3.8: Schematic of the extended setup of that shown in Figure 3.7(a) to measure the photon statistics of the Metrology Light Source (see Figure 3.8(a)) to take into account the trivial coincidences due to the electron bunch structure (see Text) and the resulting normalised coincidences (Figure 3.8(b)). The measured value of  $g^{(2)}(0)$  of  $1.0049 \pm 0.0008$  is close to the estimated value  $g_e^{(2)}(0) = 1.006$ .

### *3 Bridging the Radiometric Gap*

close to the estimated value  $g_e^{(2)}(0) = 1.006$ .

Hence, the Poissonian statistics has to be used to perform the correction for the influence of the statistical fraction of pulses from a single electron bunch that contained two or more photons.

### 3.3.3 Traceable Calibration of Free Space Single Photon Avalanche Diodes

Two free space Si single photon avalanche diodes (SPADs) produced by Perkin&Elmer [96], further named SPAD1 and SPAD2, were calibrated in order to determine the detection efficiency by means of synchrotron radiation. To perform the calibration, the synchrotron radiation was monochromatised by a filter with a central wavelength of 651.34 nm, spatially filtered by an aperture with a free diameter of 50 mm and focussed sequentially on a trap detector, as the reference detector, and the SPAD (see schematic of the setup in Figure 3.9). The beam focus had a FWHM of 40  $\mu\text{m}$ . The absolute photon rate per

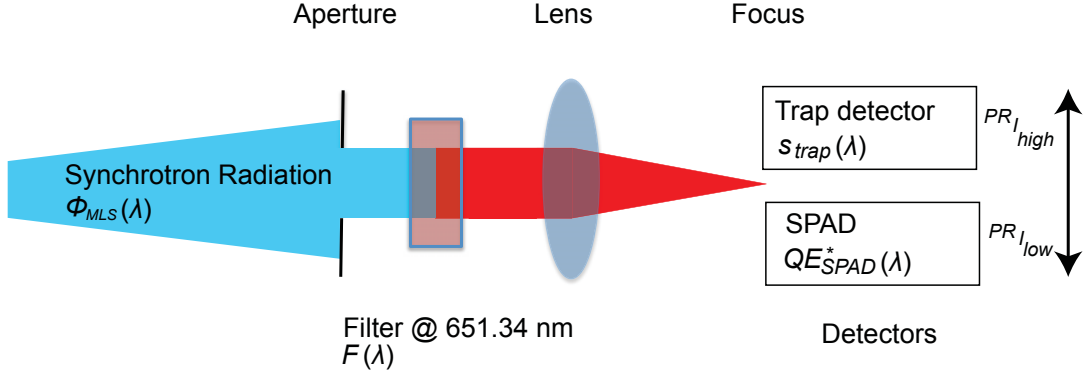


Figure 3.9: Schematic of the setup used to calibrate Single Photon Avalanche Diodes (SPADs). The photon rate ( $PR_{I_{\text{high}}}$ ) in the high ring current range was measured in the focus of the synchrotron radiation by a calibrated trap detector using its known responsivity  $s_{\text{trap}}(\lambda)$ . In a second step the count rate of the SPAD  $CR_{\text{SPAD}}$  was measured in the low ring current range. The uncorrected detection efficiency of the SPAD  $DE_{\text{SPAD}}^*$  can then be calculated according to equations (3.46) to (3.50).

stored electron in the focus was determined at a ring current  $I_{\text{high}}$  of about 140 mA using the trap detector that was calibrated traceable to a cryogenic radiometer of PTB. At this level the ring current was measured with a relative standard uncertainty of  $4.8 \cdot 10^{-4}$  by parametric current transformers. The ring current was then reduced to several hundred pA ( $I_{\text{low}}$ ), i.e. several hundred stored electrons. At this level, the ring current  $I_{\text{low}}$  was calculated as the product of the revolution frequency in the storage ring and the number of stored electrons which was determined via counting every electron loss with cooled monitor diodes [145] until no electrons were left in the ring. Given the fact that the emitted number of photons per stored electron is independent of the ring current, the broad dynamic range of the Metrology Light Source is used to bridge the gap between the radiant power level used in classical radiometry and the level of a few photons/s. Using

### 3 Bridging the Radiometric Gap

this calibration method, no attenuators, that would have to be characterised, are needed and the linearity of the transfer detection system, trap detector and amperemeter, has to be known only in the  $\mu\text{W}$  power regime. The count rate of the SPADs per stored

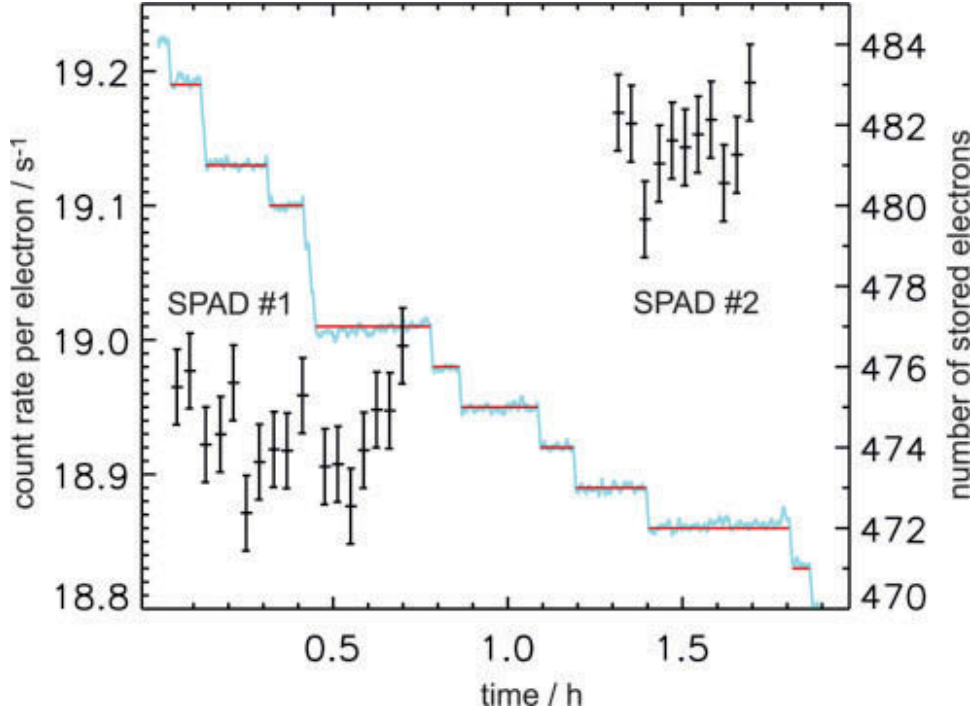


Figure 3.10: Count rate of SPAD1 and SPAD2 (black crosses) per stored electron (left scale) and number of stored electrons (blue line measured electron number, red line guidance for the eye, right scale) vs. measurement time. The discrete steps in the red and blue line are due to electron losses (figure taken from [13]).

electron was measured for different electron numbers. Figure 3.10 shows the results of these measurements. The determined count rates of the SPAD per stored electron (left axis) and the number of stored electrons (right axis) are plotted over measurement time. Higher count rates per stored electron result in higher detection efficiencies. Thus, the uncorrected detection efficiency of the SPAD  $DE_{\text{SPAD}}^*$  is determined from the count rate of the SPAD  $CR_{\text{SPAD}}$  and the photon rate in the low ring current regime  $PR_{I_{\text{low}}}$  by the following relation:

$$DE_{\text{SPAD}}^* = \frac{CR_{\text{SPAD}}}{PR_{I_{\text{low}}}} \quad (3.46)$$

### 3.3 Bridging the Radiometric Gap with Synchrotron Radiation

Using the relations:

$$PR_{I_{\text{low}}} = PR_{I_{\text{high}}} \frac{N_{I_{\text{low}}}}{N_{I_{\text{high}}}} \quad (3.47)$$

$$PR_{I_{\text{high}}} = \frac{i_{\text{trap}}}{S_{\text{trap}} \cdot E_{\text{phot}}} \quad (3.48)$$

$$N_{I_{\text{high}}} = \frac{I_{\text{high}}}{e^-} \cdot \tau \quad (3.49)$$

(3.46) can be expressed as follows:

$$DE_{\text{SPAD}}^* = \frac{CR_{\text{SPAD}}}{N_{I_{\text{low}}}} \cdot \frac{S_{\text{trap}} \cdot E_{\text{phot}} \cdot I_{\text{high}} \cdot \tau}{e^- \cdot i_{\text{trap}}} \quad (3.50)$$

with  $CR_{\text{SPAD}}$  the measured count rate of the SPAD,  $S_{\text{trap}}$  the spectral responsivity of the trap detector,  $E_{\text{phot}}$  the photon energy,  $I_{\text{high}}$  the measured ring current in the high current range,  $\tau$  the revolution time of a stored electron of 160 ns,  $e^-$  the elementary charge,  $PR$  the rate of the photons emitted by the Metrology Light Source and collected by the setup shown in Figure 3.9,  $N_{I_{\text{high}}, I_{\text{low}}}$  the number of stored electrons for high ( $I_{\text{high}}$ ) and low ( $I_{\text{low}}$ ) ring current and  $i_{\text{trap}}$  the measured photocurrent of the calibrated trap detector.  $DE_{\text{SPAD}}^*$  is a first approximation of the detection efficiency. Several corrections are still needed to get the correct detection efficiency of the SPAD and its uncertainty.

#### Corrections and Uncertainties

$DE_{\text{SPAD}}$  was determined for SPAD1 and SPAD2. All necessary corrections and relevant sources of uncertainty are given below. The DE was calculated according to (3.51) from the measured  $DE_{\text{SPAD}}^*$  and the correction factors:  $c_s$  for the influence of the different detector sizes,  $c_{\text{bw}}$  for the bandwidth of the used filter,  $c_{\text{ap}}$  for the afterpulsing probability,  $c_{\text{dt}}$  for the SPAD dead time and  $c_{\text{st}}$  for the photon statistics of the synchrotron radiation.

$$DE_{\text{SPAD}} = c_s c_{\text{bw}} c_{\text{ap}} c_{\text{dt}} c_{\text{st}} DE_{\text{SPAD}}^* \quad (3.51)$$

**Correction for Different Detector Sizes of SPAD and Trap Detector** Because of the different detector sizes, the SPAD may not detect all the radiation which is detected by the trap detector. To correct for the different detector sizes, a possible influence of the vertical source size (parameter  $\varepsilon$ , see above) on the calibration result was investigated and the transmission of the synchrotron radiation through the apertures of two pinholes, alternately placed in the focus of the synchrotron radiation, was measured with a single photodiode (see Figure 3.11). To estimate the dependence of  $\varepsilon$  on the ring current the stability of the signal of a photodiode with a pinhole of 196  $\mu\text{m}$  (see Figure 3.11) normalised to the ring current was measured for ring currents from 140 mA to 5 mA. The independence of the ratio of photocurrent and ring current on the ring current is a prerequisite for the correction of the different detector sizes of SPAD and trap detector. The result of this measurement is shown in Figure 3.12. As shown

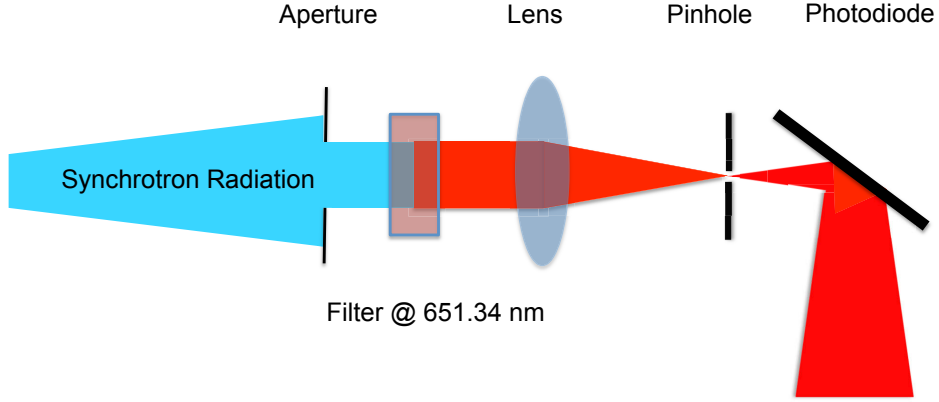


Figure 3.11: Schematic of the setup used to determine the correction factor for the different detector sizes of SPAD and trap detector. The photodiode signal was measured for three configurations, without pinhole and with pinholes with a diameter of  $149\ \mu\text{m}$  and  $196\ \mu\text{m}$ . The results are given in Table 3.1.

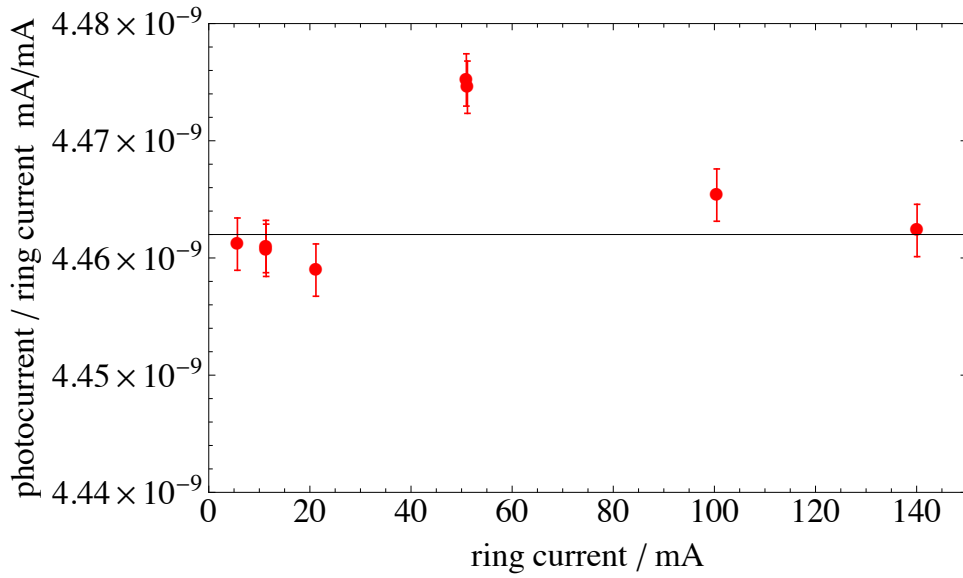


Figure 3.12: Stability of the transmission through a  $196\ \mu\text{m}$  pinhole and, thus, of the vertical source size  $\varepsilon$  of the synchrotron radiation. The relative standard uncertainty of the measurement is given by the uncertainty of the ratio of the photocurrent and the ring current  $u_{I_{\text{trapnorm}}} = 0.051\%$ . The spike at 50 mA ring current arises from a short instability of the cooling system of the Metrology Light Source and has been neglected.

### 3.3 Bridging the Radiometric Gap with Synchrotron Radiation

in Figure 3.12, the influence of a change of the electron beam size can be neglected for the given calibration conditions. However, for a pinhole diameter of 150  $\mu\text{m}$  the normalised photocurrent was depending on the ring current. These results are not shown here because they don't affect the calibration with the active diameter of the SPADS being larger than 196  $\mu\text{m}$  (as shown below).

Pinholes with a diameter of 196  $\mu\text{m}$  and 149  $\mu\text{m}$  were chosen for the setup shown in Figure 3.11, thus one being larger and one being smaller than the nominal diameter of the SPADs of 180  $\mu\text{m}$  as given in the data sheets. The photocurrent of the measurement without pinhole was compared with the photocurrents obtained with the two pinholes to determine the losses due to the different detector sizes. Table 3.1 shows the resulting losses with respect to the measurement without pinhole. Furthermore, the SPAD diameter was determined with low uncertainty by using an attenuated and focussed He-

Pinhole	Losses
$\infty$	0%
149 $\mu\text{m}$	4.63%
196 $\mu\text{m}$	3.71%
210 $\mu\text{m}$	3.44%*

Table 3.1: Measurement of the radiation losses associated with the two different pinholes and the linear extrapolated value\* for an active SPAD diameter of 210  $\mu\text{m}$ .

Ne-laser beam with a spot size smaller than 15  $\mu\text{m}$  and a wavelength of 633 nm. Three motorised translation stages were used to scan the laser focus over the SPAD area. The measurements resulted in SPAD diameters of  $(210 \pm 2)$   $\mu\text{m}$  for both SPADs (see Figure 3.13) which is considerably larger than the nominal value in the data sheets [96]. The transmittance through the pinhole was calculated for this experimentally determined diameter and gives a correction factor  $c_s = 1.0344 \pm 0.0009$ .

**Bandwidth Correction** To correct for the spectral dependence of the calculated emitted photon flux of the Metrology Light Source  $\Phi_{\text{MLS}}(\lambda)$ , of the transmittance of the used interference filter  $F(\lambda)$  and of the different spectral shapes of the responsivity of the trap detector  $S_{\text{trap}}(\lambda)$  and the detection efficiency of the SPADs  $\tilde{D}E_{\text{SPAD}}(\lambda)$  two correction factors were determined:

$$c_{\text{SPAD}} = \frac{\int_{\lambda} \Phi_{\text{MLS}}(\lambda) \cdot F(\lambda) \cdot \tilde{D}E_{\text{SPAD}}(\lambda) \cdot d(\lambda)}{\tilde{D}E_{\text{SPAD}}(651.34 \text{ nm}) \cdot \int_{\lambda} \Phi_{\text{MLS}}(\lambda) \cdot F(\lambda) \cdot d(\lambda)} \quad (3.52)$$

$$c_{\text{trap}} = \frac{\int_{\lambda} \Phi_{\text{MLS}}(\lambda) \cdot F(\lambda) \cdot S_{\text{trap}}(\lambda) \cdot E_{\text{phot}}(\lambda) \cdot d(\lambda)}{S_{\text{trap}}(651.34 \text{ nm}) \cdot \int_{\lambda} \Phi_{\text{MLS}}(\lambda) \cdot F(\lambda) \cdot E_{\text{phot}}(\lambda) \cdot d(\lambda)} \quad (3.53)$$

Only the relative spectral functions of the wavelength-dependent quantities (see Figure 3.14) are needed in (3.52) and (3.53). The relative spectral functions can differ from

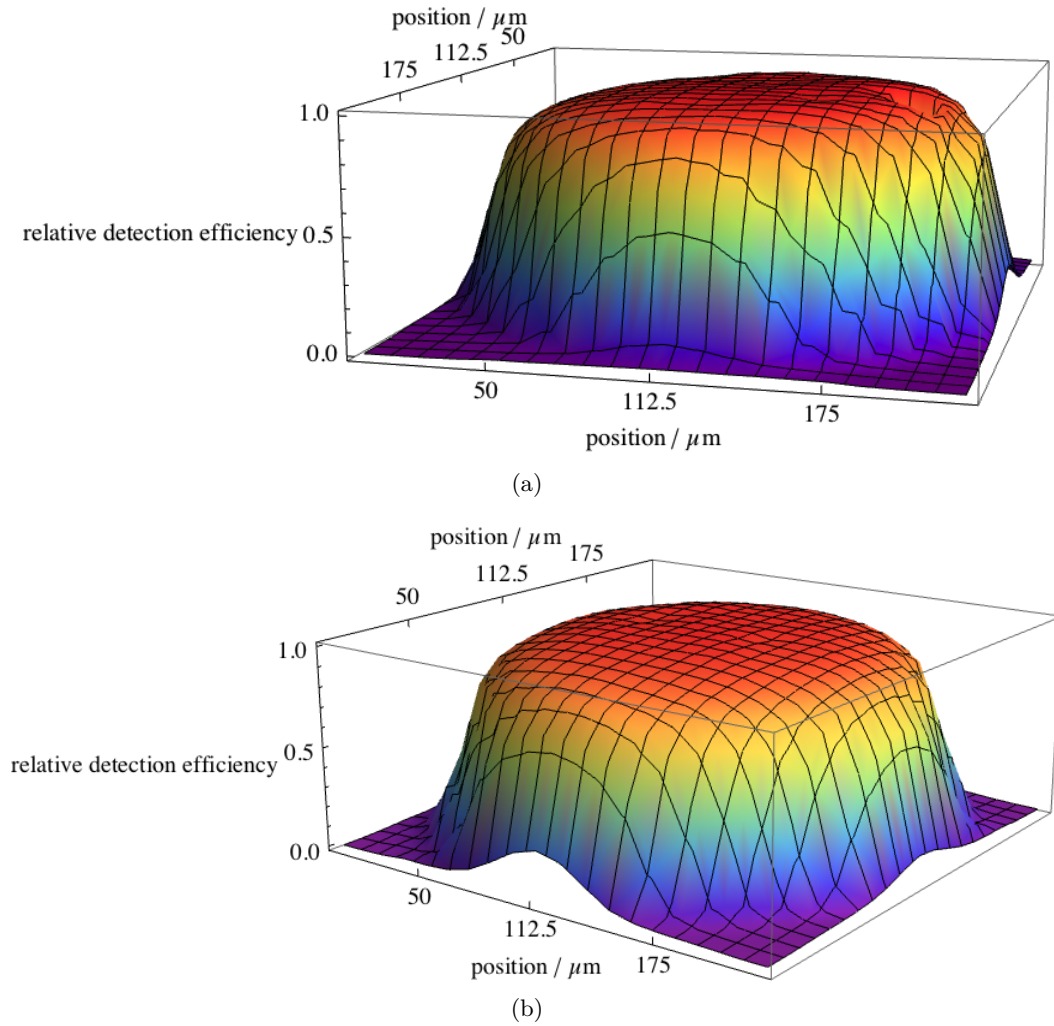


Figure 3.13: Uniformity of the two calibrated SPADs. Figure 3.13(a) shows SPAD1 and Figure 3.13(b) shows SPAD2. The measurements were performed with an attenuated He-Ne laser at a wavelength of 633 nm and a spot size smaller than 15  $\mu\text{m}$ . The active diameter, obtained from the full width at half maximum diameter, is 210  $\mu\text{m}$  for both devices.

### 3.3 Bridging the Radiometric Gap with Synchrotron Radiation

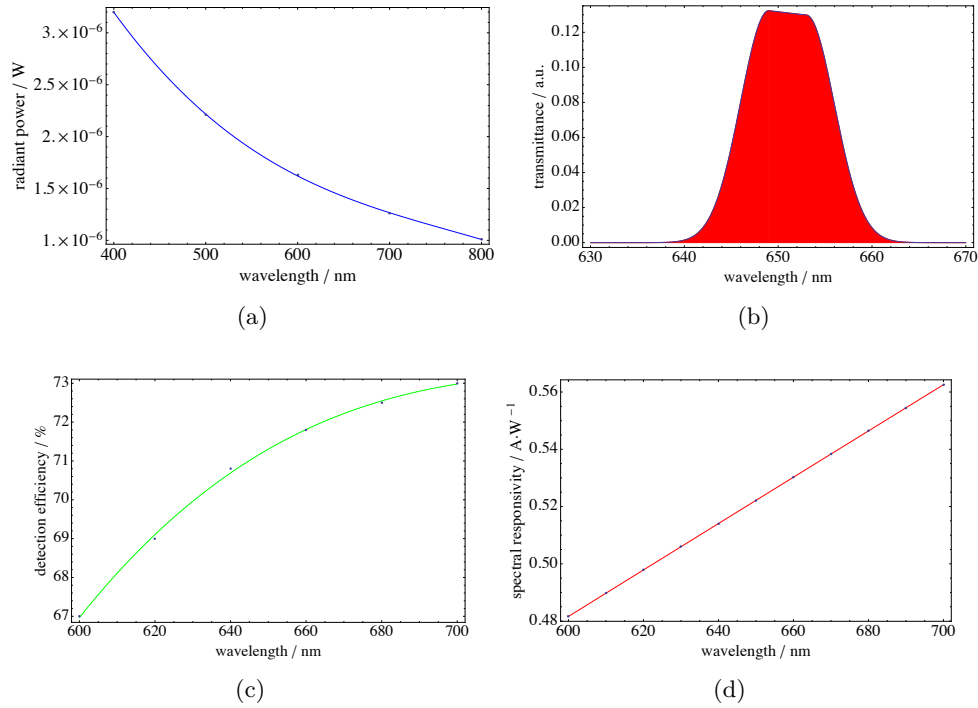


Figure 3.14: Visualisation of the input parameters for the equations (3.52), (3.53) (see text). The figures show the calculated spectral radiant power of the Metrology Light Source (Figure 3.14(a)), the transmittance of the interference filter (Figure 3.14(b)) taken from the data sheet, the detection efficiency of the SPADs (Figure 3.14(c)) taken from the data sheet [96], and the measured spectral responsivity of the reference detector (Figure 3.14(d)).

the corresponding quantity by a wavelength independent factor. Therefore the nominal detection efficiency of the SPAD taken from the data sheet  $\tilde{D}E_{\text{SPAD}}(\lambda)$  [96] was used for this correction and the same wavelength dependent photon flux of the Metrology Light Source has been used in (3.52) and (3.53). The correction is then calculated from the ratio of the bandwidth correction of the SPAD and of the trap detector and results in  $c_{\text{bw}} = c_{\text{SPAD}}/c_{\text{trap}} = 1.0004 \pm 0.00019$ .

**Correction for Afterpulse and Dead Time** An afterpulse of a SPAD is characterised not to be initiated by an incoming photon, but to appear statistically directly after the dead time after a photon absorption (see Figure 3.15). To measure the afterpulse probability a He-Ne-Laser at 633 nm was focussed on the SPADs and attenuated to give a SPAD count rate similar to the count rates while performing the calibration with synchrotron radiation because the afterpulse probability depends on the count rate of the detector [12]. The afterpulse probability was determined from the ratio of afterpulses to photon counts. For SPAD1 and SPAD2 10000 photon detections events were sampled

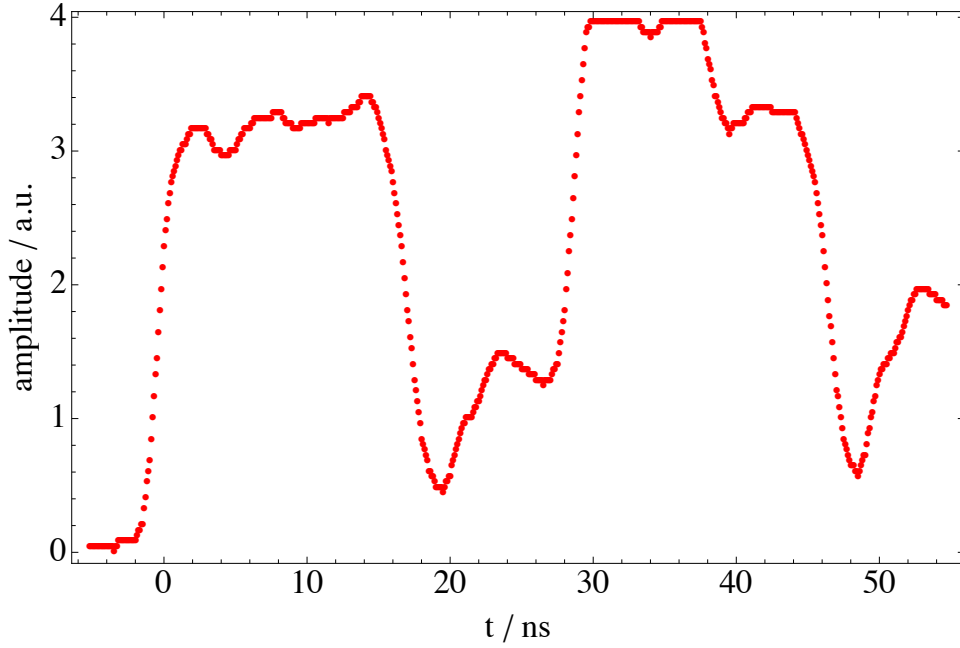


Figure 3.15: Output signal of SPAD1 measured with an oscilloscope. The photon induced output voltage pulse (time span 0 ns to 20 ns) is followed by a, so-called, afterpulse (time span 28 ns to 48 ns) directly after the end of the dead time of SPAD1 of 28 ns.

with an Agilent DSO1024A oscilloscope. The samples were then analysed to count the fraction of events where an additional pulse, the afterpulse, comes directly after the end of the dead time, i.e. in the time window of 27 ns to 29 ns after the initial output pulse. The resulting afterpulse probability is  $p_{\text{ap1}} = 0.14\%$  for SPAD1 and  $p_{\text{ap2}} = 0.07\%$  for SPAD2 at a count rate of about 9000 cps. The afterpulse correction factor is obtained by calculating  $c_{\text{ap1,2}} = 1 - p_{\text{ap1,2}}$ . The dead time  $dt$  has been determined from the shortest duration between two output pulses to be 28 ns for both SPADs at a count rate of about 9000 cps and introduces only a minor correction of  $c_{\text{dt}} = 1.00025 \pm 0.00002$  obtained from  $c_{\text{dt}} = (1 - dt \cdot CR)^{-1}$ .

**Correction for Photon Counting Statistics** To perform the correction for the photon counting statistics, the fraction of pulses that contains three or more photons has been neglected since  $p(3) \ll p(2)$ . The correction is calculated for the emission characteristics of the Metrology Light Source, i.e. a pulse rate of 500 MHz, and a photon rate of about  $13000 \text{ s}^{-1}$  at  $I_{\text{low}}$ , which gives a mean photon number per pulse of the order of  $\mu = 2.6 \cdot 10^{-5}$ . Assuming a Poisson statistics, as discussed in chapter 3.3.2, the probability that a pulse contains two photons is  $9 \cdot 10^{-6}$  and the correction factor  $c_{\text{st}} = 1 + p_2/p_1 = 1.000009 \pm 0.000009$ . Since the correction factor is almost unity, this correction has an uncertainty as the value of this correction.

**Uncertainty Budget** Table 3.2 shows the uncertainties arising from the measurements and of the applied corrections. The values given are relative standard uncertain-

Source of uncertainty		correction factor	SPAD1	SPAD2
count rate of SPAD	$u_{CR}$		0.045%	0.043%
ratio photocurrent to ring current ( $I_{high}$ ), type A	$u_{I_{trapnorm}}$		0.051%	0.051%
photocurrent trap	$u_{ampmeter}$		0.02%	0.02%
ring current ( $I_{high}$ )	$u_{I_{ring}}$		0.048%	0.048%
spectral responsivity trap	$u_{S_{trap}}$		0.045%	0.045%
positioning SPAD	$u_{pos}$		0.02%	0.02%
source size variation	$u_{ss}$		0.048%	0.048%
dead time	$c_{dt}$	1.00025	0.002%	0.002%
photon statistics	$c_{st}$	1.000009	0.0009%	0.0009%
bandwidth	$c_{bw}$	1.0004	0.019%	0.019%
afterpulsing of SPAD1	$c_{ap1}$	0.99857	0.098%	
afterpulsing of SPAD2	$c_{ap2}$	0.99933		0.071%
detector size	$c_s$	1.0344	0.09%	0.09%
combined relative standard uncertainty of the detection efficiency	$u$		0.17%	0.16%

Table 3.2: Relative standard uncertainties and correction factors contributing to the traceable calibration of the detection efficiency of two SPADs using synchrotron radiation.

ties. The uncertainty for the determination of the count rate of the SPADs contains the uncertainty of the measurement of the count rate and the uncertainty of the determination of the dark count rate and gives  $u_{CR_{SPAD1}} = 0.045\%$  and  $u_{CR_{SPAD2}} = 0.043\%$ . The uncertainty of the spectral responsivity of the transfer detector is  $u_{S_{trap}} = 0.045\%$ . Another source of uncertainty is the determination of the ratio of the photocurrent of the calibrated trap detector and the ring current at  $I_{high}$ . The values of the uncertainties connected to these measurements are the uncertainty of the measurement of the ring current  $u_{I_{ring}} = 0.048\%$ , the systematical uncertainty of the used amperemeter  $u_{ampmeter} = 0.02\%$  and the type A uncertainty of the measured ratio of the photocurrent of the trap detector and of the ring current  $u_{I_{trapnorm}} = 0.051\%$ .

Within the uncertainty of the ring current measurement  $u_{I_{ring}}$ , there was no dependence of the ratio of transmitted synchrotron radiation and ring current from the ring current, therefore, this uncertainty contributes with the uncertainty of the ring current measurement to the uncertainty budget (see Table 3.2), i.e.  $u_{ss} = u_{I_{ring}}$ , as an upper limit estimate. The uncertainties of the number of stored electrons  $N_{I_{low}}$  and of the revolution time  $\tau$  are below 0.001% and have not been listed. The uncertainty arising from the

### 3 Bridging the Radiometric Gap

positioning of the SPADs with respect to the synchrotron radiation focus with motorised stages is  $u_{\text{pos}} = 0.02\%$ .

The combined relative uncertainty of this calibration is  $u_{\text{SPAD1}} = 0.17\%$  for SPAD1 and  $u_{\text{SPAD2s}} = 0.16\%$  for SPAD2. The main contributions to these overall uncertainties are the uncertainties of the corrections for the different detector sizes  $c_s$  and for the afterpulsing probability  $c_{\text{ap}}$  (see Table 3.2). These results show that the uncertainties achieved with this method are slightly better than the lowest uncertainties achieved so far by means of the SPDC and the substitution method [119].

### 3.3.4 Traceable Calibration of Fibre-coupled Superconducting Single Photon Detectors

A fibre-coupled superconducting nanowire single photon detector (SNSPD) (see chapter 3.1), produced by SCONTEL, Russia, was calibrated traceable to a cryogenic radiometer by means of synchrotron radiation.

#### Measurement Principle

The measurement principle for fibre-coupled detectors is similar to the principle for the free space detectors. A schematic of the setup is shown in Figure 3.16. The detection efficiency of the SNSPD is polarisation dependent. Thus, a fibre-coupled polariser was used for this calibration. The polarisation has been adjusted to reach the maximum count rate of the SNSPD. The used ring current ranges are substantially different for

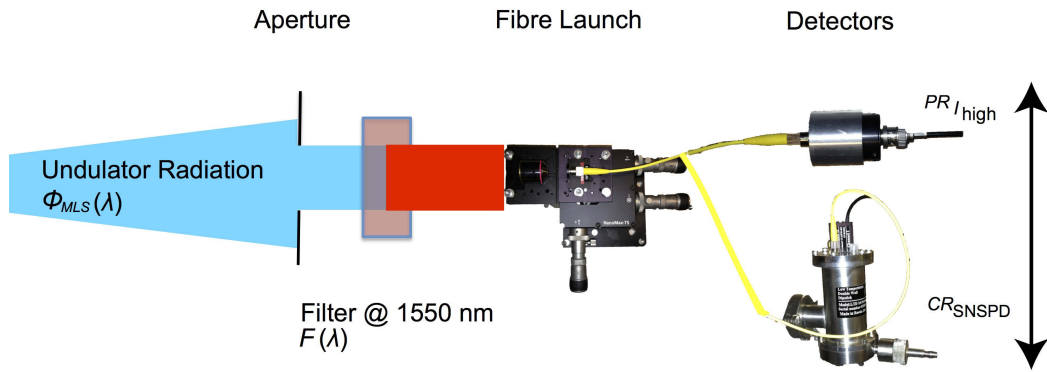


Figure 3.16: Schematic of the setup used to calibrate a fibre-coupled superconducting nanowire single photon detector (SNSPD). The photon rate ( $PR_{I_{high}}$ ) in the high ring current range is measured by a calibrated InGaAs reference detector using its known responsivity  $S_{IGA}(\lambda)$ . In a second step the count rate of the SNSPD  $CR_{SNSPD}$  is measured in the low ring current range. Both detectors are, depending on the ring current, alternately connected to the same optical fibre. The uncorrected detection efficiency of the SNSPD  $DE_{SNSPD}^*$  can then be calculated according to equations (3.46) to (3.50).

this calibration method as compared to the free space calibration described above. The vertical source size of the synchrotron radiation becomes a critical parameter and limits the maximum ring current to values of approximately 1 mA. At higher ring currents the coupling between the electrons in the circulating electron bunches is current dependent and, thus, changes the vertical source size. Thus, the coupling efficiency of the synchrotron radiation into the fibre is ring current dependent for ring currents above 1 mA.

### 3 Bridging the Radiometric Gap

Furthermore, the minimum ring current is limited to values not smaller than several nA to achieve sufficient count rates of the DUTs caused by the coupling losses into the optical fibre. To increase the available radiant power of the Metrology Light Source per stored electron, the undulator U180 [145] was used in this calibration campaign.

To perform the calibration of the SNSPD, the synchrotron radiation was monochromatised by a filter with a central wavelength of 1551.97 nm and fed into a single mode optical fibre (SMF-28) for a wavelength of 1550 nm. The fibre-coupled synchrotron radiation was then connected to the reference detector, a calibrated InGaAs photodiode, and the SNSPD sequentially (see schematic of the setup in Figure 3.16). The SNSPD was current biased to 90% of the critical bias current. The absolute photon rate per stored electron that was coupled into the fibre was determined at a ring current  $I_{\text{high}}$  of about 1 mA using an InGaAs detector that was calibrated traceable to a cryogenic radiometer of PTB. At this level the ring current could be measured with a relative standard uncertainty of  $5 \cdot 10^{-3}$  by cooled photodiodes with aluminium filters. The ring current was then reduced to approximately 5 nA. At this ring current  $I_{\text{low}}$ , corresponding to about five thousand stored electrons, the count rate of the SNSPD, normalised to the ring current, was measured. At this level, the ring current was measured by counting the electrons as described above. The uncertainty contribution of the measurement of  $I_{\text{low}}$  was below  $10^{-5}$  and was neglected. A detailed description of the ring current measurement of the Metrology Light Source can be found in [145]. The uncorrected detection efficiency of the SNSPD  $DE_{\text{SNSPD}}^*$  is, using the relation (3.50) with the count rate of the SNSPD  $CR_{\text{SNSPD}}$  and the photon rate in the low ring current regime  $PR_{I_{\text{low}}}$ , determined from:

$$DE_{\text{SNSPD}}^* = \frac{CR_{\text{SNSPD}}}{PR_{I_{\text{low}}}}. \quad (3.54)$$

The measured photon rate of the Metrology Light Source per stored ring electron and the measured count rate of the SNSPD is plotted in Figure 3.17. As for  $DE_{\text{SPAD}}^*$ ,  $DE_{\text{SNSPD}}^*$  is a first approximation of the detection efficiency. The corrections and uncertainties to get the precise detection efficiency of the SNSPD are given below.

#### Corrections and Uncertainties

**Correction for Photon Statistics** As described before, the Poissonian statistics was used to perform the correction for the influence of the statistical fraction of pulses from a single electron bunch that contained up to three photons. The correction was calculated for the emission characteristics of the Metrology Light Source, i.e. a pulse rate of 500 MHz, and a photon rate of about  $630000 \text{ s}^{-1}$  at  $I_{\text{low}}$ , which gives a mean photon number per pulse of the order of  $\mu = 0.001$ . This minor correction has a value of  $c_{\text{st}} = 1.0006$ . The relative uncertainty of the correction factor has been determined to be 50% of the correction, i.e.  $u(c_{\text{st}}) = 0.03\%$ .

**Correction for Dead Time** The dead time  $dt_{\text{SNSPD}}$  of the SNSPD was determined to be  $10 \pm 2 \text{ ns}$  by sampling the output pulse of the SNSPD with an oscilloscope and measuring the duration where the output pulse declined to 0 V. The dead time introduces

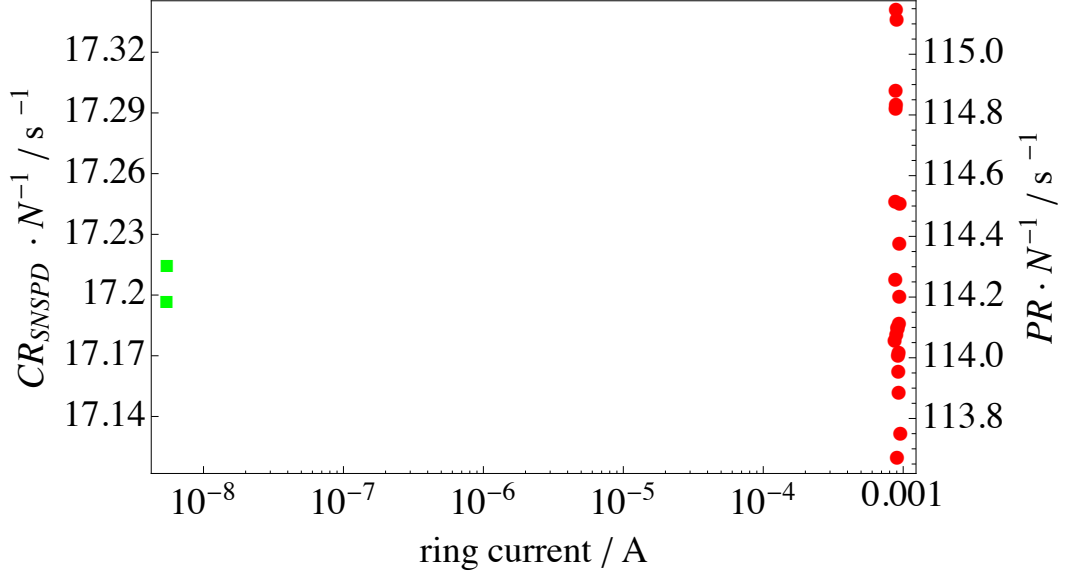


Figure 3.17: Ratio of the photon rate ( $PR$ ) to the number of stored electrons ( $N$ ) (red circles) and ratio of the count rate of the SNSPD ( $CR_{\text{SNSPD}}$ ) and the number of stored electrons ( $N$ ) (green squares) plotted over the electron ring current of the Metrology Light Source. The uncertainty of the measured ring current and, thus, of the measured ratios in the high ring current range was  $u_{I_{\text{InGaAsnorm}}} = 0.53\%$  and  $u_{\text{CR}} = 0.075\%$  in the low ring current regime.

a correction of  $c_{dt_{\text{SNSPD}}} = 1.00095$  obtained from  $c_{dt} = (1 - dt \cdot CR)^{-1}$ . Furthermore, the counting electronics has an additional dead time  $dt_{\text{counting}}$  of  $20 \pm 1$  ns which introduces a correction of  $c_{dt_{\text{counting}}} = 1.0019$ . The uncertainties of these correction are  $u(c_{dt_{\text{SNSPD}}}) = 0.02\%$  for the dead time correction of the SNSPD and  $u(c_{dt_{\text{counting}}}) = 0.01\%$  for the dead time correction of the counting electronics.

**Correction for Bandwidth of the Synchrotron Radiation** To correct for the spectral dependence of the calculated emitted photon flux of the undulator U180 of the Metrology Light Source  $\Phi_{\text{MLS}}(\lambda)$ , of the transmittance of the used interference filter  $F(\lambda)$  and the different spectral shapes of the responsivity of the reference detector  $S_{\text{InGaAs}}$  and the detection efficiency  $\tilde{D}E_{\text{SNSPD}}(\lambda)$  of the SNSPD two correction factors were determined:

$$c_{\text{SNSPD}} = \frac{\int_{\lambda} \Phi_{\text{MLS}}(\lambda) \cdot F(\lambda) \cdot \tilde{D}E_{\text{SNSPD}}(\lambda) \cdot d(\lambda)}{\tilde{D}E_{\text{SNSPD}}(1551.97 \text{ nm}) \cdot \int_{\lambda} \Phi_{\text{MLS}}(\lambda) \cdot F(\lambda) \cdot d(\lambda)} \quad (3.55)$$

$$c_{\text{InGaAs}} = \frac{\int_{\lambda} \Phi_{\text{MLS}}(\lambda) \cdot F(\lambda) \cdot S_{\text{InGaAs}}(\lambda) \cdot E_{\text{phot}}(\lambda) \cdot d(\lambda)}{S_{\text{InGaAs}}(1551.97 \text{ nm}) \cdot \int_{\lambda} \Phi_{\text{MLS}}(\lambda) \cdot F(\lambda) \cdot E_{\text{phot}}(\lambda) \cdot d(\lambda)} \quad (3.56)$$

As for the calibration of the SPADs only the relative spectral functions of the wavelength-dependent quantities are needed in (3.55) and (3.56). The nominal detection efficiency of the SNSPD was taken from the data sheet,  $\tilde{DE}_{\text{SNSPD}}(\lambda)$  was used for this correction and the same wavelength dependent photon flux of the Metrology Light Source was used in (3.55) and (3.56). The correction is then calculated as the ratio of the bandwidth correction of the SNSPD and of the reference detector and results in  $c_{\text{bwSNSPD}} = 0.9990$ . The uncertainty of  $c_{\text{bwSNSPD}}$  has been estimated to  $u(c_{\text{bwSNSPD}}) = 0.01\%$ .

**Correction for the Applied Bias Current** As described in chapter 3.1.1, SNSPDs are typically operated at a bias current of 90% of the critical bias current value. The minimum current increment that can be adjusted by the controller of the SNSPD system is  $0.1 \mu\text{A}$  with typical critical currents in the range from  $20 \mu\text{A}$  to  $30 \mu\text{A}$ . Hence, the accuracy of the determined critical bias current as well as the applied bias current are limited by the controller. The uncertainty contribution of the measurement of the critical bias current  $I_{\text{critical}}$  has been determined to  $u(I_{\text{critical}}) = 0.82\%$  using the dependence of the detection efficiency on the bias current (see also Figure 3.18). In addition, the measured detection efficiency was corrected to obtain the value for an applied bias current of 90% of the critical value. Figure 3.18 shows the measured detection efficiency

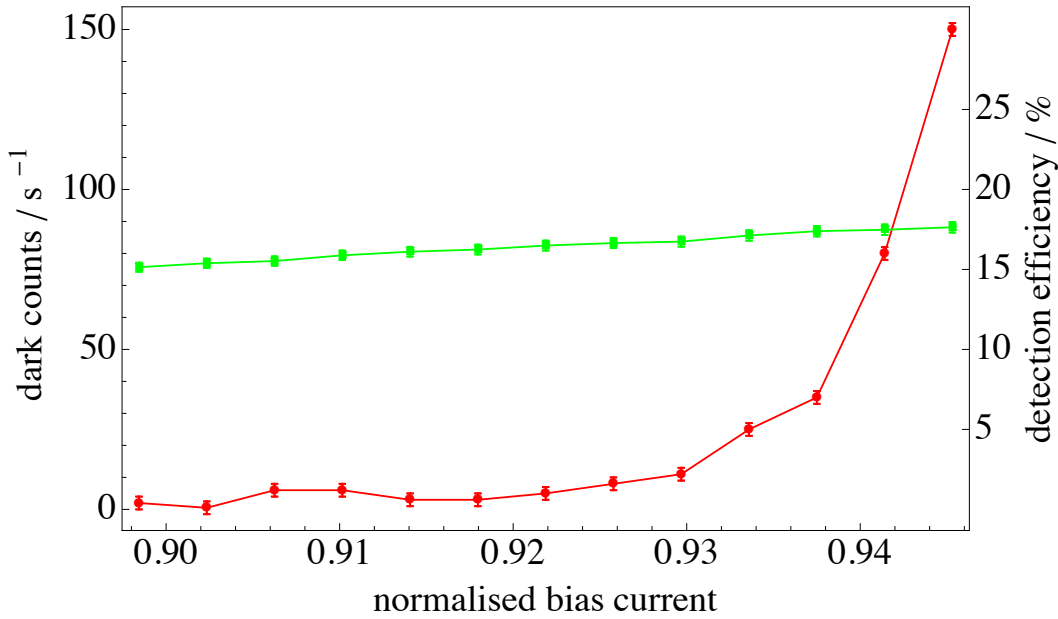


Figure 3.18: Measured detection efficiency (green squares) and dark count rate (red circles) of the SNSPD plotted over the bias current normalised to the critical bias current. The uncertainty bars of the measured detection efficiency are about the same size as the green markers.

and the dark count rate of the SNSPD versus the applied bias current normalised to the critical current. The actual applied bias current  $I_{\text{bias}}$  during the calibration was set

to  $I_{\text{bias}} = 0.901 \cdot I_{\text{critical}}$ . The correction for the applied bias current was determined from the dependence of the detection efficiency on the applied bias current, shown in Figure 3.18 to  $c_{\text{bias}} = 0.9952$  with  $u(c_{\text{bias}}) = 0.16\%$ .

**Polarisation Dependence of the Detection Efficiency** To determine the uncertainty contribution associated with the polarisation dependence of the detection efficiency of the SNSPD, the reproducibility of the polarisation adjustment was investigated with a laser source at a wavelength of approximately 1550 nm. A fibre-coupled polariser,

Number of measurement	Counts
1	391386681
2	405478987
3	395911617
4	396988365
5	401358925
6	390917877
7	392670740
8	401704623
relative standard uncertainty	1.35%

Table 3.3: Measurement of the repeatability of the polarisation adjustment of the radiation incident on the SNSPD. The counts were integrated over a period of 30 s.

that was connected with the laser and the SNSPD, was used to maximise the count rate of the SNSPD, i.e. to set the polarisation of the radiation incident on the SNSPD parallel to the meander wire. The count rate was integrated over a period of 30 s. The bias current was set to  $21.6 \mu\text{A}$ , i.e. to 90% of the critical bias current. The relative standard uncertainty associated with the polarisation dependence of the SNSPD was then obtained from the relative standard deviation of the measured counts (see Table 3.3) to  $u_{\text{pol}} = 1.35\%$ .

**Uncertainty Budget** Table 3.4 shows the uncertainties arising from the measurements and from the introduced corrections. The values given are relative standard uncertainties. The uncertainty for the determination of the count rate of the SNSPD contains the uncertainty in the measurement of the count rate, the uncertainty of the determination of the dark count rate and the uncertainty contribution of the counting electronics as well as the repeatability of the measurement and gives  $u_{CR_{\text{SNSPD}}} = 0.075\%$ . The uncertainty of the calibration of the reference detector is  $u_{S_{\text{InGaAs}}} = 0.15\%$ . Another source of uncertainty is the determination of the ratio of the photocurrent of the calibrated reference detector and the ring current at  $I_{\text{high}}$ . The values of the uncertainties connected to these measurements are the uncertainty of the measurement of

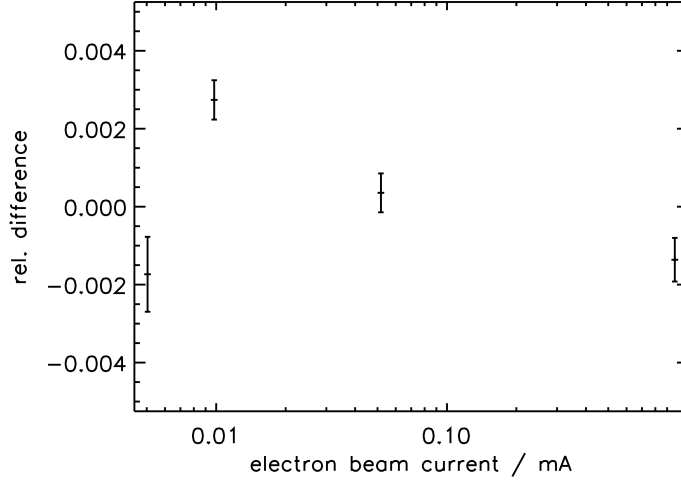


Figure 3.19: Relative change of the fibre-coupling efficiency of the synchrotron radiation of the Metrology Light Source into the optical fibre at  $1.55 \mu\text{m}$  plotted over the electron beam current. Within the uncertainties of the ring current measurement no systematical dependence of the coupling efficiency on the electron beam current has been detected for ring currents below 1 mA (figure taken from [158]).

the ring current  $u_{I_{\text{ring}}} = 0.5\%$ , the systematical uncertainty of the used amperemeter  $u_{\text{ampmeter}} = 0.05\%$  and the type A uncertainty of the measured ratio of the photocurrent of the reference detector and of the ring current  $u_{I_{\text{InGaAsnorm}}} = 0.53\%$ .

To check whether the finite vertical source size of the synchrotron radiation has an influence on the calibration result the change of the coupling efficiency into the optical fibre has been measured with the reference detector and has been normalised to the ring current. Figure 3.19 shows the measured change of the coupling efficiency plotted over the ring current. Within the uncertainty of the ring current measurement  $u_{I_{\text{ring}}}$  there was no dependence of the coupling efficiency into the fibre and ring current, for ring currents below 1 mA. Therefore, this uncertainty contributes with the uncertainty of the ring current measurement to the uncertainty budget, i.e.  $u_{\text{ss}} = u_{I_{\text{ring}}}$  as an upper limit estimate. The uncertainty arising from the reproducibility of the coupling efficiency into the fibre with respect to the synchrotron radiation is  $u_{\text{fc}} = 0.38\%$ . This uncertainty occurs for the reference detector as well for the SNSPD. The reproducibility of the connection of the optical fibre with the SNSPD contributes to the uncertainty budget with  $u_{\text{fibre}} = 0.38\%$ . The reproducibility of the polarisation adjustment in order to maximise the count rate of the SNSPD and, thus, the uncertainty contribution is  $u_{\text{pol}} = 1.35\%$ .

The combined relative uncertainty of this calibration of a SNSPD is  $u_{\text{SNSPD}} = 1.87\%$ . The main contribution to these overall uncertainties (see Table 3.4) is the uncertainty associated with the polarisation dependence of the detection efficiency of the SNSPD.

Source of uncertainty		correction factor	SNSPD
count rate of SNSPD	$u_{\text{CR}}$		0.075%
ratio photocurrent to ring current ( $I_{\text{high}}$ ), type A photocurrent	$u_{I_{\text{InGaAsnorm}}}$		0.53%
reference detector	$u_{\text{ampmeter}}$		0.05%
ring current ( $I_{\text{high}}$ )	$u_{I_{\text{high}}}$		0.5%
spectral responsivity InGaAs detector	$u_{S_{\text{InGaAs}}}$		0.15%
fibre-coupling reference detector	$u_{\text{fc}}$		0.38%
fibre-coupling SNSPDS	$u_{\text{fc}}$		0.38%
source size variation	$u_{\text{ss}}$		0.5%
polarisation	$u_{\text{pol}}$		1.35%
fibre connection	$u_{\text{fibre}}$		0.36%
critical bias current	$u_{\text{bc}}$		0.82%
applied bias current $c_{\text{bias}}$	$u_{\text{bias}}$	0.9952	0.16%
SNSPD dead time $c_{dt\text{SNSPD}}$	$u_{\text{dt}}$	1.00095	0.02%
photon statistics $c_{\text{st}}$	$u_{\text{st}}$	1.00062	0.031%
bandwidth $c_{\text{bw}}$	$u_{\text{bw}}$	0.9990	0.01%
combined relative standard uncertainty of the detection efficiency	$u_{\text{SNSPD}}$		1.87%

Table 3.4: Relative standard uncertainties and correction factors contributing to the traceable calibration of a SNSPD by means of synchrotron radiation.

### 3.4 Conclusions

Two types of single photon detectors, SPADs and a SNSPD, have been calibrated traceable to a primary detector standard, the cryogenic radiometer, by means of synchrotron radiation. The measured detection efficiencies are  $DE_{\text{SPAD1}}(651.34 \text{ nm}) = 0.6988 \pm 0.0012$  for SPAD1,  $DE_{\text{SPAD2}}(651.34 \text{ nm}) = 0.7073 \pm 0.0011$  for SPAD2, and  $DE_{\text{SNSPD}}(1551.97 \text{ nm}) = 0.1501 \pm 0.0028$  for the SNSPD. The Metrology Light Source was used to bridge the gap in the radiant power needed to operate the classical reference detectors with low uncertainties and the photon fluxes that allow low uncertainty measurements with the SPADs and the SNSPD.

The exploitation of the properties of synchrotron radiation offers a method to calibrate single photon detectors in the visible and NIR. The uncertainties achievable with this method are limited by the capabilities of the single photon detectors and the measurement uncertainty of the electron storage ring current in the high ring current range only. The uncertainty contribution of the ring current measurement can be reduced down

### 3 Bridging the Radiometric Gap

to a level of about 0.02% by proper calibration of the parametric current transformers that are used to measure the ring current in the high current range and, hence, would make this method the most promising candidate for the lowest calibration uncertainty achievable. The uncertainties achieved within this work are of about the same numerical value or slightly better than the best results published so far [8]. With the experiences gained with this attempt to calibrate single photon detectors by means of synchrotron radiation in the visible, the uncertainty for upcoming calibrations of free space single photon detectors could be reduced down to a level of 0.1%. This uncertainty level equals a reduction of the uncertainties available so far by a factor of two.

For the traceable calibration of fibre-coupled single photon detectors, the synchrotron calibration method offers a significant reduction of the achievable uncertainties. Within the “MIQC” project, the synchrotron radiation method was expanded to support fibre-coupled calibrations. The aim of the “MIQC” project is to reduce the uncertainties of traceable single photon detector calibrations down to 3%. This goal has been fulfilled with the synchrotron radiation method which enables radiometric calibrations of fibre-coupled single photon detectors with uncertainties smaller than 2%. Though third generation electron storage rings are only available to a few national metrology institutes the unique properties of these sources make this method valuable. In particular, the combination of the number of wavelengths at which calibrations can be performed and the low uncertainties achievable are unrivalled by any other calibration method. Especially stakeholders in sciences such as astronomy or elementary particle physics will profit from this highly reliable method where radiation conditions can be adapted to the needs of the experiment, such as, e.g., the simulation of a space-like radiation background.

Furthermore, the photon statistics of monochromatised synchrotron radiation in the NIR was measured for the first time. The result, a Poissonian statistic, i.e.  $g^{(2)}(0) \approx 1$ , agrees well with the expected value [157]. The knowledge of the appropriate correction mechanism is a prerequisite for the use of the synchrotron calibration method with photon rates of 100000/ s or higher.

## 4 Conclusions and Outlook

The results presented in this work show a substantial progress in the development of detector-based radiometry. The first central subject of this work, to reduce the uncertainties associated with the measurements of radiometric units was achieved with the calibration of photodetectors with a primary detector standard, a cryogenic radiometer. The uncertainties have been reduced to a level of  $10^{-5}$  with the setup of the new cryogenic radiometer facility of PTB [19]. The new facility has been used in this work to validate the potential novel primary detector standard for radiometric measurements in the wavelength range from 400 nm to 800 nm, the Predictable Quantum Efficient Detector (PQED). In addition, the PQED is the only potential primary radiometric detector standard that can be used in the future to bridge the radiometric gap, i.e. that is suitable for the application with radiant power levels from milliwatts down to the pW level.

The second central subject of this work, i.e. to bridge the radiometric gap between the classical and the few photon radiometry, was achieved by two different approaches.

First: The PQED, suitable for radiometric measurements in both the classical and the few photon regime was characterised, validated and the linearity of the detector was tested down to 0.1 nW level [18, 19]. The PQED marks the most recent detector development, aiming to reduce the uncertainties in radiant power measurements in the wavelength range from 400 nm to 800 nm by one to two orders of magnitude down to the ppm level.

Second: A calibration method based on the unique properties of synchrotron radiation, that enables radiometric calibrations of single photon detectors with the lowest uncertainties reported so far, was used to calibrate single photon detectors in the visible and NIR traceable to a primary standard, a cryogenic radiometer.

To achieve a significant reduction of the uncertainty of detector based radiometry and to characterise and validate the potential of the novel PQED the following objectives were accomplished:

- A power stabilised laser source was developed that enables radiometric measurements at the 10 ppm level with a standard deviation of the laser power of  $7.34 \cdot 10^{-6}$  within a time period of 300 minutes.
- The photodiodes to be used in the PQED were characterised in terms of relative uniformity and linearity of the spectral responsivity. To measure the uniformity of the relative spectral responsivity of single photodiodes a dedicated facility was set up. Furthermore, a facility to measure the linearity of the spectral responsivity was adopted to be compatible with the PQED, the power stabilised DFB laser and

#### 4 Conclusions and Outlook

the necessary measurement equipment. The measurements with these facilities achieved relative standard uncertainties of the order of  $4 \cdot 10^{-5}$  for the relative uniformity of the spectral responsivity and  $3 \cdot 10^{-5}$  for the linearity of single PQED photodiodes.

- For the fabrication and simulation of the photodiodes produced for the PQED, the dependence of the photocurrent on the applied bias voltage and on the temperature of the photodiodes was evaluated. The results of these measurements revealed that the absorption coefficient of silicon is a major source of uncertainty for the simulation of the internal quantum deficiency for wavelengths above 600 nm when operated at temperatures of approximately 78 K. Furthermore, the application of an additional back electrode on the photodiodes produced in the second batch to reduce the recombination losses at temperatures of 78 K was driven by the results of this thesis.
- The facility to accommodate the new cryogenic radiometer of PTB was set up. The new cryogenic radiometer facility has been characterised and an uncertainty budget has been compiled that proved a significant reduction of the relative standard uncertainty to 19 ppm associated with the measurement of the radiant power.
- The PQED has been validated by verifying the predicted spectral responsivity by measurements with the new cryogenic radiometer of PTB.
- An uncertainty budget for the validation of the PQED with the new cryogenic radiometer facility of PTB has been compiled that proved a relative standard uncertainty of the validation of about 30 ppm.
- The experimental results obtained in this work have been evaluated and merged to provide input for the development of the PQED. In addition, it has been shown that the PQED can be used as a primary detector standard in the wavelength range from 400 nm to 800 nm if the temporal stability has been validated.

To bridge the radiometric gap by means of synchrotron radiation four objectives were fulfilled:

- Two types of single photon detectors to be calibrated in terms of detection efficiency have been chosen, i.e. single photon avalanche photodiodes to prove the calibration method with free space single photon detectors in the visible wavelength range and fibre-coupled superconducting nanowire single photon detectors for measurements in the NIR. The single photon detectors have been characterised to quantify the contributions of the detectors to the uncertainty budgets of the calibration of the detection efficiency.
- The photon statistics of the MLS was calculated and was validated experimentally. The results show a good agreement of the calculated and the experimental value with a relative deviation of less than 0.1% and, thus, enables the use of synchrotron radiation for the calibration of single photon detectors.

- Two calibration setups were established and characterised to allow the calibration of fibre-coupled and free space single photon detectors by means of synchrotron radiation. These setups were used to determine the detection efficiency of two free space SPADs and a fibre-coupled SNSPD.
- Uncertainty budgets for the calibration of fibre-coupled and free space single photon detectors were compiled. The relative standard uncertainty of the measured detection efficiency for the free space single photon detectors is 0.16% and 0.17%. The relative standard uncertainty of the measured detection efficiency of the fibre-coupled single photon detector is 1.87% with the polarisation dependence of the detection efficiency being the dominant uncertainty contribution.

With the synchrotron radiation based method for single photon detector calibrations in the visible and NIR, a traceability chain has been established that achieved the lowest uncertainties published so far. This method can be applied to free space and fibre-coupled single photon detectors. Furthermore, this method can be used to validate the substitution and SPDC calibration method.

With the new cryogenic radiometer of PTB, the newly developed PQED, and the unique properties of the Metrology Light Source, the PTB is able to provide radiant power scales with extremely low uncertainties in the range from milliwatts of radiant power down to a few photons per second in the visible and NIR.

## Outlook

In the coming years, the work presented in this thesis will be continued to further improve radiometric techniques and to reduce the uncertainties associated with radiometric measurements in classical and few photon radiometry.

Recently a joint European research project, “NEWSTAR” (New Standards and Traceability for Radiometry) was started to improve the PQED, i.e. to improve the design, the production procedure, and the modelling of the PQED. “NEWSTAR” brings together NMIs from twelve countries (Italy, Czech Republic, France, Spain, Norway, Estonia, Finland, Hungary, Germany, New Zealand, Brazil, Republic of Korea) and two universities from Norway and Estonia. Much effort will be put into the determination of the solid-state parameters that are necessary for the prediction of the PQED. For this purpose the effective electron-hole pair lifetime will be measured at different densities of fixed SiO<sub>2</sub>-oxide surface charge of the photodiodes from the different sets of photodiodes that have been and will be produced. The aim is to ultimately identify a processing technique that improves the effective electron-hole pair lifetime.

Furthermore, the SiO<sub>2</sub>-oxide charge, doping profiles and electron-hole pair lifetime of the photodiodes produced in the “Candela” and the “NEWSTAR” project will be measured. These data will be used by to develop three-dimensional software models based on the measured parameters. These models will be used to simulate the internal quantum deficiency of the various batches of diodes at different wavelengths, reverse bias voltages and temperatures.

The absorption coefficient in silicon as a function of wavelength and temperature will

#### 4 Conclusions and Outlook

be studied to create a table with justified estimates of spectrally dependent silicon absorption coefficients over the spectral range from 400 nm to 900 nm at 300 K and 77 K. The uncertainty contribution of the absorption coefficient of silicon was identified in this work as one of the dominant uncertainties in the prediction of the internal quantum deficiency of the PQED.

The responsivity ratio of PQEDs equipped with photodiodes from the different processing will be measured to validate the developed software models with uncertainties at the ppm level. The characterisations and comparison of the PQEDs from the different manufacturing rounds could identify any differences in the manufacturing rounds. Measurements against the CRCF of PTB will be used to evaluate the accuracy of the prediction in addition to the comparisons shown in this work. To validate the spectral responsivity of the PQED, that will be predicted by three-dimensional software models, the uncertainty in the cryogenic radiometry has to be further reduced. To achieve a relative standard uncertainty of the order of 10 ppm when validating the PQED with the CRCF, the CRCF has to be improved and more precisely characterised. The first important step to reduce the uncertainties to the 10 ppm level are the deployment of higher resolution temperature controllers at the CRCF that, in addition, have to provide traceability of the measured heater power of the cryogenic radiometer of the CRCF to the SI. The second step is to measure the absorption coefficient of the cryogenic radiometer cavity of the CRCF traceable to the SI with a relative standard uncertainty of approximately 2 ppm.

To improve the traceability of radiometric measurements to the SI at the few photon level, the synchrotron radiation method will be validated by the SPDC and substitution method with reduced uncertainties by directly comparing the three methods. In addition, the PQED will be used as the reference the detector when calibrating free-space single photon detectors in the visible. The linearity of the PQED, proven in this work in the range from about 450  $\mu\text{W}$  to less than 1 nW, can then be used to validate the independence of the vertical source size of the synchrotron radiation of the MLS on the number of stored electrons for ring currents below 1 mA.

Currently radiometry is based on the three primary standards: Calculable blackbody radiation, synchrotron radiation and cryogenic radiometer.

With this work, an important step towards a new primary standard - the PQED - has been achieved. Further work on the PQED in the framework of “NEWSTAR” has the aim to establish a completely independent, compact and easy to use, primary standard. This would implement a significant progress in modern radiometry.

# Bibliography

- [1] BIPM. The International System of Units (SI brochure (EN)): 8th edition, 2006. pages 1–88, April 2006.
- [2] H Payn. *The Merchandise marks act 1887: with special reference to the importation sections and the customs regulations and orders made thereunder*. Stevens, 1888.
- [3] F Kurlbaum. 5. Bericht über die Thätigkeit der Physikalisch-Technischen Reichsanstalt. *Zeitschrift für Instrumentenkunde*, 14:261–278, 1894.
- [4] F Kurlbaum and O. Lummer. Der electrisch geglühte "absolut schwarze" Körper und seine Temperaturmessung. *Verhandlungen der Deutschen Physikalischen Gesellschaft*, 17:106–111, 1898.
- [5] F Kurlbaum. Ueber eine Methode zur Bestimmung der Strahlung in absolutem Maass und die Strahlung des schwarzen Körpers zwischen 0 und 100 Grad. *Annalen der Physik*, 301(8):746–760, 1898.
- [6] V Scarani, A Acín, G Ribordy, and N Gisin. Quantum Cryptography Protocols Robust against Photon Number Splitting Attacks for Weak Laser Pulse Implementations. *Physical Review Letters*, 92(5):057901–1–057901–4, 2004.
- [7] C Branciard, N Gisin, B Kraus, and V Scarani. Security of two quantum cryptography protocols using the same four qubit states. *Physical Review A*, 72(3):32301–1–032301–18, September 2005.
- [8] S Polyakov and A Migdall. Quantum radiometry. *Journal Of Modern Optics*, 56(9):1045–1052, May 2009.
- [9] TE Hansen. Silicon UV-Photodiodes Using Natural Inversion Layers. *Physica Scripta*, 18:471–475, 1978.
- [10] W Wien. Ueber die Energievertheilung im Emissionsspectrum eines schwarzen Körpers. *Annalen der Physik*, 294(8):662–669, 1896.
- [11] M Planck. Zur Theorie des Gesetzes der Energieverteilung im Normalspectrum. *Verhandlungen der Deutschen Physikalischen Gesellschaft*, 2(17):237–245, 1900.
- [12] S Polyakov. High accuracy calibration of photon-counting detectors "on demand" (Proceedings Paper). *Proceedings of SPIE*, 6583:65830A–1–65830A–8, 2007.

- [13] I Müller, RM Klein, J Hollandt, G Ulm, and L Werner. Traceable calibration of Si avalanche photodiodes using synchrotron radiation. *Metrologia*, 49(NEWRAD):S152–S155, 2012.
- [14] Ingmar Müller. Wave meets Particle. *PTB-news*, 2012(2):4, December 2012.
- [15] M Richter, J Hollandt, U Kroth, W Paustian, H Rabus, R Thornagel, and G Ulm. Source and detector calibration in the UV and VUV at BESSY II. *Metrologia*, 40:S107–S110, 2003.
- [16] M Richter, A Gottwald, F Scholze, R Thornagel, and G Ulm. Calibration of space instrumentation with synchrotron radiation. *Advances In Space Research*, 37(2):265–272, January 2006.
- [17] J Gran, T Kübarsepp, M Sildoja, F Manoocheri, and Ingmar Müller. Simulations of a predictable quantum efficient detector with PC1D. *Metrologia*, 49(NEWRAD):S130–S134, 2012.
- [18] M Sildoja, F Manoocheri, M Merimaa, E Ikonen, I Müller, L Werner, J Gran, T Kübarsepp, M Smîd, and ML Rastello. Predictable quantum efficient detector: I. Photodiodes and predicted responsivity. *Metrologia*, 50(4):385–394, July 2013.
- [19] I Müller, U Johannsen, U Linke, L Socaciu-Siebert, M Smîd, G Porrovecchio, M Sildoja, F Manoocheri, E Ikonen, J Gran, T Kübarsepp, G Brida, and L Werner. Predictable quantum efficient detector: II. Characterization and confirmed responsivity. *Metrologia*, 50(4):395–401, July 2013.
- [20] DN Klyshko. Coherent decay of photons in a nonlinear medium. *Pis’ma Zh. Eksp. Teor. Fiz*, 6:490–492, 1967.
- [21] DN Klyshko. Utilization of vacuum fluctuations as an optical brightness standard. *Soviet Journal of Quantum Electronics*, 7(5):591–595, May 1977.
- [22] R Klein, G Brandt, R Fliegauf, A Hoehl, R Müller, R Thornagel, G Ulm, M Abo-Bakr, J Feikes, and M Hartrott. Operation of the Metrology Light Source as a primary radiation source standard. *Physical Review Special Topics-Accelerators and Beams*, 11(11):110701, 2008.
- [23] J Hartmann, J Hollandt, P Meindl, D. Taubert, and L Werner. Traceable radiometric calibration of semiconductor detectors and their application for thermodynamic temperature measurement. *Mapan*, 25(1):3–10, 2010.
- [24] L Werner, J Fischer, U Johannsen, and J Hartmann. Accurate determination of the spectral responsivity of silicon trap detectors between 238 nm and 1015 nm using a laser-based cryogenic radiometer. *Metrologia*, 37(4):279–284, 2000.
- [25] J Geist. Quantum Efficiency of the P-N-Junction in Silicon as an Absolute Radiometric Standard. *Applied Optics*, 18(6):760–762, 1979.

- [26] JE Martin, NP Fox, and PJ Key. A cryogenic radiometer for absolute radiometric measurements. *Metrologia*, 21:147–155, 1985.
- [27] JN Shive. The properties of germanium phototransistors. *JOSA*, 43(4):239–243, 1953.
- [28] A Einstein. Über einen die Erzeugung und Verwandlung des Lichtes betreffenden heuristischen Gesichtspunkt. *Annalen der Physik*, 322:132–148, 1905.
- [29] E Zalewski and J Geist. Silicon photodiode absolute spectral response self-calibration. *Applied Optics*, 19(8):1214–1216, 1980.
- [30] J Geist. Generalized photodiode self-calibration formula. *Applied Optics*, 30(7):884–886, 1991.
- [31] J Geist, G Brida, and ML Rastello. Prospects for improving the accuracy of silicon photodiode self-calibration with custom cryogenic photodiodes. *Metrologia*, 40(1):132, 2003.
- [32] J Geist and H Baltes. High accuracy modeling of photodiode quantum efficiency. *Applied Optics*, 28(18):3929–3939, 1989.
- [33] M Gerlach, M Krumrey, L Cibik, P Müller, H Rabus, and G Ulm. Cryogenic radiometry in the hard x-ray range. *Metrologia*, 45(5):577–585, October 2008.
- [34] M Krumrey, C Herrmann, P Muller, and G Ulm. Synchrotron-radiation-based cryogenic radiometry in the X-ray range. *Metrologia*, 37(5):361–364, 2000.
- [35] H Rabus, R Klein, F Scholze, R Thornagel, and G Ulm. Validation of the uncertainty budget for soft X-ray radiant power measurement using a cryogenic radiometer. *Metrologia*, 39(4):381–389, 2002.
- [36] P Kuschnerus, H Rabus, M Richter, F Scholze, L Werner, and G Ulm. Characterization of photodiodes as transfer detector standards in the 120 nm to 600 nm spectral range. *Metrologia*, 35(4):355–362, 1998.
- [37] P Meindl, AE Klinkmüller, L Werner, U Johannsen, and K Grützmacher. New UV spectral responsivity scale of the PTB based on a cryogenic radiometer and an argon plasma arc radiation source. *Metrologia*, 43(2):S72–S77, March 2006.
- [38] M Richter, U Johannsen, P Kuschnerus, U Kroth, H Rabus, G Ulm, and L Werner. The PTB high-accuracy spectral responsivity scale in the ultraviolet. *Metrologia*, 37(5):515–518, 2000.
- [39] L Werner, R Friedrich, U Johannsen, and A Steiger. Precise scale of spectral responsivity for InGaAs detectors based on a cryogenic radiometer and several laser sources. *Metrologia*, 37(5):523–526, 2000.

## Bibliography

- [40] L Werner, H-W Hübers, P Meindl, R Müller, H Richter, and A Steiger. Towards traceable radiometry in the terahertz region. *Metrologia*, 46(4):S160–S164, June 2009.
- [41] EH Putley. History of infrared detection - Part 1. The first detectors of thermal radiation. *Infrared Physics*, (22):125–131, 1982.
- [42] F Hengstberger. *Absolute radiometry*. Academic Press, July 1989.
- [43] AC Parr. TN 1421 - A National Measurement System for Radiometry, Photometry, and Pyrometry Based upon Absolute Detectors , 1996.
- [44] RW Brusa and C Fröhlich. Absolute radiometers (PMO6) and their experimental characterization. *Applied Optics*, 25(22):4173–4180, 1986.
- [45] G Allègre, B Guillet, D Robbes, L Méchin, S Lebargy, and S Nicoletti. A room temperature Si 3N 4/SiO2 membrane-type electrical substitution radiometer using thin film platinum thermometers. *Measurement Science and Technology*, 18(1):183–189, November 2006.
- [46] CC Hoyt and PV Foukal. Cryogenic radiometers and their application to metrology. *Metrologia*, 28:163–167, 1991.
- [47] KD Stock, H Hofer, M White, and NP Fox. Lowest uncertainty direct comparison of a mechanically-cooled and a helium-cooled cryogenic radiometer. *Metrologia*, 37(5):437–439, 2000.
- [48] N Fox. Trap detectors and their properties. *Metrologia*, 28:197–202, 1991.
- [49] Ö Bazkır and F Samadov. Characterization of silicon photodiode-based trap detectors and establishment of spectral responsivity scale. *Optics and lasers in engineering*, 43:131–141, 2005.
- [50] KD Stock, S Morozova, L Liedquist, and H Hofer. Nonlinearity of the quantum efficiency of Si reflection trap detectors at 633 nm. *Metrologia*, 35(4):451–454, 1998.
- [51] R Goebel and M Stock. Nonlinearity and polarization effects in silicon trap detectors. *Metrologia*, 35(4):413–418, 1998.
- [52] R Goebel, S Yilmaz, and R Pello. Polarization dependence of trap detectors. *Metrologia*, 33:207–213, 1996.
- [53] TR Gentile, JM Houston, and CL Cromer. Realization of a scale of absolute spectral response using the national institute of standards and technology high-accuracy cryogenic radiometer. *Applied Optics*, 35(22):4392–4403, 1996.
- [54] J Hartmann. High-temperature measurement techniques for the application in photometry, radiometry and thermometry. *Physics Reports-Review Section of Physics Letters*, 469:205–269, 2009.

- [55] RG Hunsperger. *Integrated Optics*. Theory and Technology. Springer, April 2009.
- [56] DJ Butler, R Kohler, and GW Forbes. Diffraction effects in the radiometry of coherent beams. *Appl. Opt*, 35(13):2162–2166, April 1996.
- [57] J Fischer and L Fu. Photodiode nonlinearity measurement with an intensity stabilized laser as a radiation source. *Applied Optics*, 32(22):4187–4190, 1993.
- [58] Michael Bock. private communication.
- [59] L Boivin and K Gibb. Monochromator-based cryogenic radiometry at the NRC. *Metrologia*, 32:565–570, 1995.
- [60] CA Schrama, R Bosma, K Gibb, H Reijn, and P Bloembergen. Comparison of monochromator-based and laser-based cryogenic radiometry. *Metrologia*, 35:431–435, 1998.
- [61] P Blattner. Neue optische Strahlungsmessbasis am METAS. *metINFO*, 12:1–6, 2005.
- [62] M López, H Hofer, and S Kück. Measurement of the absorptance of a cryogenic radiometer cavity in the visible and near infrared. *Metrologia*, 42(5):400–405, September 2005.
- [63] S Lorentz. Characterization Results CryoRad II. *Manual*, pages 1–46, January 2010.
- [64] KA Snail, DP Brown, JP Costantino, WC Shemano, CW Schmidt, WF Lynn, CL Seaman, and TR Knowles. Optical characterization of black appliques. In A Peter M Glassford, Robert P Breault, and Stephen M Pompea, editors, *SPIE’s 1996 International Symposium on Optical Science, Engineering, and Instrumentation*, pages 465–474. SPIE, November 1996.
- [65] P Debye. Zur Theorie der spezifischen Wärmen. *Annalen der Physik*, 344(14):789–839, 1912.
- [66] F Lei and J Fischer. Characterization of photodiodes in the UV and visible spectral region based on cryogenic radiometry. *Metrologia*, 30(4):297–303, 1993.
- [67] J Geist, E Liang, and AR Schaefer. Complete Collection of Minority-Carriers from the Inversion Layer in Induced Junction Diodes. *Journal of Applied Physics*, 52(7):4879–4881, 1981.
- [68] AR Schaefer, EF Zalewski, and J Geist. Silicon detector nonlinearity and related effects. *Applied Optics*, 22(8):1232–1236, 1983.
- [69] EF Zalewski and CR Duda. Silicon photodiode device with 100% external quantum efficiency. *Appl. Opt*, 22(18):2867–2867, 1983.

## Bibliography

- [70] F Manoocheri, M Sildoja, M Merimaa, E Ikonen, I Müller, L Werner, J Gran, SH Stian, T Kübarsepp, G Porrovecchio, M Smid, G Brida, and ML Rastello. Predictable quantum efficient detector (pqed). In *Proceedings of NEWRAD 2011*, pages 13–14, 2011.
- [71] M Sildoja, F Manoocheri, M Merimaa, E Ikonen, I Mueller, L Werner, J Gran, T Kuebarsepp, M Smid, and ML Rastello. Predictable quantum efficient detector i: Photodiodes and design. In *Proceedings of NEWRAD 2011*, pages 227–228, 2011.
- [72] SS Hoem, J Gran, M Sildoja, F Manoocheri, E Ikonen, and I Müller. Physics of self-induced photodiodes. In *Proceedings of NEWRAD 2011*, pages 259–260, 2011.
- [73] BE Deal, M Sklar, AS Grove, and EH Snow. Characteristics of the Surface-State Charge (Q<sub>ss</sub>) of Thermally Oxidized Silicon. *Journal of The Electrochemical Society*, 114(3):266–274, 1967.
- [74] I Mueller, G Brida, J Gran, SS Hoem, E Ikonen, T Kuebarsepp, U Linke, F Manoocheri, M Sildoja, M Smid, LD Socaciu-Siebert, and L Werner. Predictable quantum efficient detector ii: Characterization results. In *Proceedings of NEWRAD 2011*, pages 209–210, 2011.
- [75] KD Stock. Si-photodiode spectral nonlinearity in the infrared. *Applied Optics*, 25(6), 1986.
- [76] M Sildoja, F Manoocheri, and E Ikonen. Reflectance calculations for a predictable quantum efficient detector. *Metrologia*, 46(4):S151–S154, 2009.
- [77] W Zinth and U Zinth. *Optik. Lichtstrahlen- Wellen- Photonen*. Oldenbourg Verlag, March 2011.
- [78] MA Green. Self-consistent optical parameters of intrinsic silicon at 300K including temperature coefficients. *Solar Energy Materials and Solar Cells*, 92(11):1305–1310, November 2008.
- [79] G Ghosh. Dispersion-equation coefficients for the refractive index and birefringence of calcite and quartz crystals. *Optics Communications*, 163(1):95–102, 1999.
- [80] T Toyoda and M Yabe. The temperature dependence of the refractive indices of fused silica and crystal quartz. *Journal of Physics D: Applied Physics*, 16(5):L97–L100, May 1983.
- [81] SG Warren. Optical constants of ice from the ultraviolet to the microwave. *Applied Optics*, 23:1206–1225, April 1984.
- [82] EA Taft. The Optical Constants of Silicon and Dry Oxygen Oxides of Silicon at 5461Å. *Journal of The Electrochemical Society*, 125(6):968, 1978.

- [83] D Aspnes and J Theeten. Optical Properties of the Interface between Si and Its Thermally Grown Oxide. *Physical Review Letters*, 43(14):1046–1050, October 1979.
- [84] C M Herzinger, B Johs, W A McGahan, J A Woollam, and W Paulson. Ellipsometric determination of optical constants for silicon and thermally grown silicon dioxide via a multi-sample, multi-wavelength, multi-angle investigation. *Journal of Applied Physics*, 83(6):3323–3336, 1998.
- [85] DA Clugston and PA Basore. PC1D version 5: 32-bit solar cell modeling on personal computers. In *Photovoltaic Specialists Conference, 1997., Conference Record of the Twenty-Sixth IEEE*, pages 207–210, 1997.
- [86] R Korde, C Prince, D Cunningham, and R Vest. Present status of radiometric quality silicon photodiodes. *Metrologia*, 40:S145–149, 2003.
- [87] J He, M Fang, B Li, and Y Cao. A new analytic approximation to general diode equation. *Solid-State Electronics*, 50(7-8):1371–1374, jul 2006.
- [88] R Korde and J Geist. Quantum efficiency stability of silicon photodiodes. *Applied Optics*, 26(24):5284–5290, 1987.
- [89] KO Kiepenheuer. Über Zählrohre für das sichtbare Spektralgebiet. *Zeitschrift für Physik*, 107(3-4):145–152, March 1937.
- [90] RJ McIntyre. Theory of Microplasma Instability in Silicon. *Journal of Applied Physics*, 32(6):983–995, 1961.
- [91] RE Warburton, M Itzler, and GS Buller. Free-running, room temperature operation of an InGaAs/InP single-photon avalanche diode. *Applied Physics Letters*, 94(7):071116–1–071116–3, November 2009.
- [92] RH Hadfield. Single-photon detectors for optical quantum information applications. *Nature Photonics*, 3(12):696–705, 2009.
- [93] MD Eisaman, J Fan, A Migdall, and SV Polyakov. Invited Review Article: Single-photon sources and detectors. *Review of Scientific Instruments*, 82(7):071101–1–071101–25, 2011.
- [94] F Zappa, S Tisa, A Tosi, and S Cova. Principles and features of single-photon avalanche diode arrays. *Sensors and Actuators A: Physical*, 140(1):103–112, October 2007.
- [95] S Cova, M Ghioni, A Lacaita, C Samori, and F Zappa. Avalanche photodiodes and quenching circuits for single-photon detection. *Applied Optics LP*, 35:1956, April 1996.
- [96] PerkinElmer. SPCM-AQRH Single Photon Counting Module. (11/07/V2/HW):1–10, October 2007.

- [97] J Bardeen, L Cooper, and J Schrieffer. Theory of Superconductivity. *Physical Review*, 108(5):1175–1204, 1957.
- [98] L Testardi. Destruction of Superconductivity by Laser Light. *Physical Review B*, 4(7):2189–2196, 1971.
- [99] AM Kadin and MW Johnson. Non-equilibrium photon-induced hotspot: A new mechanism for photo detection in ultra-thin metallic films. *Applied Physics Letters*, 69:3938–3940, December 1996.
- [100] A Semenov, G Gol’tsman, and A Korneev. Quantum detection by current carrying superconducting film. *Physica C: Superconductivity and its applications*, 351:349–356, 2001.
- [101] GN Gol’tsman, O Okunev, G Chulkova, A Lipatov, A Semenov, K Smirnov, B Voronov, A Dzardanov, C Williams, and R Sobolewski. Picosecond superconducting single-photon optical detector. *Applied Physics Letters*, 79:705–707, August 2001.
- [102] AD Semenov, GN Gol’tsman, and R Sobolewski. TOPICAL REVIEW: Hot-electron effect in superconductors and its applications for radiation sensors. *Superconductor Science and Technology*, 15:R1–R16, April 2002.
- [103] G Gol’tsman, A Korneev, I Rubtsova, and I Milostnaya. Ultrafast superconducting single-photon detectors for near-infrared-wavelength quantum . . . . *Physica Status Solidi C*, 2(5):1480–1488, 2005.
- [104] A Semenov, P Haas, K Ilin, H-W Huebers, M Siegel, A Engel, and A Smirnov. Energy resolution and sensitivity of a superconducting quantum detector. *Physica C: Superconductivity*, 460-462:1491–1492, September 2007.
- [105] A Kerman, E Dauler, W Keicher, and J Yang. Kinetic-inductance-limited reset time of superconducting nanowire photon counters. *Applied Physics Letters*, 88:111116–1–111116–3, 2006.
- [106] M Tarkhov, J Claudon, J P Poizat, A Korneev, A Divochiy, O Minaeva, V Seleznev, N Kaurova, B Voronov, AV Semenov, and G Gol’tsman. Ultrafast reset time of superconducting single photon detectors. *Applied Physics Letters*, 92(24):241112–1–241112–3, 2008.
- [107] J Bar, P Grabiec, M Górska, V Zwiller, and C Latta. Fiber-coupled single-photon detectors based on NbN superconducting nanostructures for practical quantum cryptography and photon-correlation studies. *Applied Physics Letters*, 88:261113–1–261113–3, 2006.
- [108] KM Rosfjord, JKW Yang, EA Dauler, Andrew J Kerman, V Anant, BM Voronov, GN Gol’tsman, and KK Berggren. Nanowire single-photon detector with an integrated optical cavity and anti-reflection coating. *Optics Express*, 14:527–534, 2006.

- [109] AD Semenov, P Haas, B Guenther, H-W Huebers, K Il'in, and M Siegel. Energy resolution of a superconducting nanowire single-photon detector. *Journal Of Low Temperature Physics*, 151:564–569, 2008.
- [110] V Anant, A Kerman, E Dauler, and J Yang. Optical properties of superconducting nanowire single-photon detectors. *Optics Express*, 16(14):10750–10761, 2008.
- [111] KD Irwin, SW Nam, B Cabrera, B Chugg, and BA Young. A quasiparticle-trap-assisted transition-edge sensor for phonon-mediated particle detection. *Review of Scientific Instruments*, 66(11):5322–5326, 1995.
- [112] B Cabrera, RM Clarke, P Colling, AJ Miller, S Nam, and RW Romani. Detection of single infrared, optical, and ultraviolet photons using superconducting transition edge sensors. *Applied Physics Letters*, 73(6):735–737, 1998.
- [113] D Magde and H Mahr. Study in ammonium dihydrogen phosphate of spontaneous parametric interaction tunable from 4400 to 16 000 Å. *Physical Review Letters*, 18(21):905–907, 1967.
- [114] M Brida, Gand Chekhova, M Genovese, A Penin, ML Rastello, and I Ruo-Berchera. Absolute Calibration of Analog Detectors by using Parametric Down Conversion. *arXiv*, quant-ph(arXiv:0705.2991), May 2007.
- [115] G Brida, M Chekhova, M Genovese, M L Rastello, and I Ruo-Berchera. Absolute calibration of analog detectors using stimulated parametric down conversion. In *Journal of Modern Optics*, pages 401–404, 2009.
- [116] C Hong and L Mandel. Theory of parametric frequency down conversion of light. *Physical Review A*, 31(4):2409–2418, 1985.
- [117] JY Cheung, CJ Chunnillall, ER Woolliams, NP Fox, JR Mountford, J Wang, and PJ Thomas. The quantum candela: a re-definition of the standard units for optical radiation. *Journal Of Modern Optics*, 54(2):373–396, 2007.
- [118] G Brida, S Castelletto, I P Degiovanni, M Genovese, C Novero, and ML Rastello. Towards an uncertainty budget in quantum-efficiency measurements with parametric fluorescence. *Metrologia*, 37(5):629–632, March 2003.
- [119] SV Polyakov and AL Migdall. High accuracy verification of a correlated-photon-based method for determining photon-counting detection efficiency. *Optics Express*, 15(4):1391–1407, 2007.
- [120] B Sanguinetti, E Pomarico, P Sekatski, H Zbinden, and N Gisin. Quantum cloning for absolute radiometry. *Physical Review Letters*, 105(8):80503–1–080503–4, 2010.
- [121] V Scarani, S Iblisdir, N Gisin, and A Acín. Quantum cloning. *Reviews of Modern Physics*, 77(4):1225–1256, 2005.

- [122] N Gisin and S Massar. Optimal Quantum Cloning Machines. *Physical Review Letters*, 79(11):2153–2156, 1997.
- [123] E Pomarico, B Sanguinetti, P Sekatski, H Zbinden, and N Gisin. Applications of quantum cloning. *Optics and Spectroscopy*, 111(4):510–519, October 2011.
- [124] AR Beaumont, JY Cheung, CJ Chunnillall, JW Ireland, and G Malcolm. Providing reference standards and metrology for the few photon–photon counting community. *Nuclear Instruments and Methods in Physics Research Section A: Accelerators, Spectrometers, Detectors and Associated Equipment*, 610(1):183–187, October 2009.
- [125] AC Carter, SI Woods, SM Carr, TM Jung, and RU Datla. Absolute cryogenic radiometer and solid-state trap detectors for IR power scales down to 1 pW with 0.1 percent uncertainty. *Metrologia*, 46(4):S146–S150, June 2009.
- [126] DJ Livigni, NA Tomlin, CL Cromer, and JH Lehman. Optical fibre-coupled cryogenic radiometer with carbon nanotube absorber. *Metrologia*, 49(2):S93–S98, 2012.
- [127] ZP Yang, L Ci, A James, SY Lin, and PM Ajayan. Experimental observation of an extremely dark material made by a low-density nanotube array. *Nano Letters*, 8(2):446–451, 2008.
- [128] J Lehman, A Sanders, L Hanssen, B Wilthan, J Zeng, and C Jensen. Very Black Infrared Detector from Vertically Aligned Carbon Nanotubes and Electric-Field Poling of Lithium Tantalate. *Nano Letters*, 10(9):3261–3266, September 2010.
- [129] JY Cheung, CJ Chunnillall, G Porrovecchio, M Smid, and E Theocharous. Low optical power reference detector implemented in the validation of two independent techniques for calibrating photon-counting detectors. *Optics Express*, 19(21):20347–20363, 2011.
- [130] J Mountford, G Porrovecchio, M Smid, and R Smid. Development of a switched integrator amplifier for high-accuracy optical measurements. *Applied Optics*, 47(31):5821–5828, 2008.
- [131] T Kübarsepp and M White. Ten-element photodetector for optical power and attenuation measurements. *Applied Optics*, 49(19):3774–3779, 2010.
- [132] T Kübarsepp and M White. Characterization of the throughput beam of a ten-photodiode transmission trap detector. *Metrologia*, 48(5):359–364, September 2011.
- [133] J Cheung, JL Gardner, A Migdall, S Polyakov, and M Ware. High accuracy dual lens transmittance measurements. *Applied Optics*, 46(22):5396–5403, 2007.

- [134] G Brida, J Cheung, I Degiovanni, M Gramegna, MG Mingolla, T Kübarsepp, I Mueller, G Porrovecchio, ML Rastello, M Smid, and L Werner. Toward Traceable Few Photon Radiometry. In *Proceedings of NEWRAD 2011*, pages 293–294. INRIM, NPL, Metroser, MIKES, CMI, PTB, NEWRAD, June 2011.
- [135] F Hinterberger. *Physik der Teilchenbeschleuniger und Ionenoptik (German Edition)*. Springer, 2nd edition, April 2008.
- [136] J Schwinger. On the Classical Radiation of Accelerated Electrons. *Physical Review*, 75(12):1912–1925, 1949.
- [137] DH Tomboulia and PL Hartman. Spectral and Angular Distribution of Ultraviolet Radiation From the 300-Mev Cornell Synchrotron. *Physical Review*, 102(6):1423–1447, 1956.
- [138] Burkhard Beckhoff, Alexander Gottwald, Roman Klein, Michael Krumrey, Ralph Müller, Mathias Richter, Frank Scholze, Reiner Thörnagel, and Gerhard Ulm. A quarter-century of metrology using synchrotron radiation by PTB in Berlin. *physica status solidi (b)*, 246(7):1415–1434, July 2009.
- [139] U Arp, R Friedman, ML Furst, S Makar, and PS Shaw. SURF III - an improved storage ring for radiometry. *Metrologia*, 37(5):357–360, 2000.
- [140] PS Shaw, U Arp, HW Yoon, RD Saunders, AC Parr, and KR Lykke. A SURF beamline for synchrotron source-based absolute radiometry. *Metrologia*, 40(1):S124–S127, 2003.
- [141] R Thörnagel, R Klein, and G Ulm. The electron storage ring BESSY II as a primary source standard from the visible to the X-ray range. *Metrologia*, 38(5):385–389, 2001.
- [142] J Gardner, A Parr, and RU Datla. *Optical radiometry*. Academic Pr Inc, October 2005.
- [143] U Arp. Influence of the vertical emittance on the calculability of the Synchrotron Ultraviolet Radiation Facility. *Journal of Research-National Institute of Standards and Technology*, 107(5):419–424, 2002.
- [144] P Shaw, U Arp, and KR Lykke. Absolute radiant flux measurement of the angular distribution of synchrotron radiation. *Phys.Rev.ST Accel.Beams*, 9:070701–1–070701–9, 2006.
- [145] R Klein, R Thörnagel, and G Ulm. From single photons to milliwatt radiant power-electron storage rings as radiation sources with a high dynamic range. *Metrologia*, 47(5):R33–R40, 2010.
- [146] T Tanabe, MC Teich, TC Marshall, and J Galayda. Measurement of photon statistics of wiggler radiation from an electron storage ring. *Nuclear Instruments*

- and Methods in Physics Research Section A: Accelerators, Spectrometers, Detectors and Associated Equipment*, 304(1):77–80, 1991.
- [147] WK Lee and DM Mills. Counting statistics and loss corrections for the APS. *Review of Scientific Instruments*, 63(1):1225–1228, 1992.
  - [148] T Miyahara. From First-Order Coherence to Higher-Order Coherence of Synchrotron Radiation. *Journal of Synchrotron Radiation*, 5:305–308, May 1998.
  - [149] RZ Tai, Y Takayama, N Takaya, T Miyahara, S Yamamoto, H Sugiyama, J Urakawa, H Hayano, and M Ando. Chaotic nature of the stored current in an electron storage ring detected by a two-photon correlator for soft-x-ray synchrotron radiation. *Physical Review A*, 60(4):3262–3266, 1999.
  - [150] R Tai, Y Takayama, N Takaya, T Miyahara, S Yamamoto, H Sugiyama, J Urakawa, H Hayano, and M Ando. A novel intensity interferometer for synchrotron radiation in the vacuum ultraviolet and soft x-ray regions. *Review of Scientific Instruments*, 71(3):1256–1263, 2000.
  - [151] DF Walls and Gerard J Milburn. *Quantum Optics*. Springer, 2 edition, January 1995.
  - [152] L Mandel, ECG Sudarshan, and E Wolf. Theory of photoelectric detection of light fluctuations. In *Proceedings of the Physical Society*, pages 435–444. Department of Physics, Imperial College, London, September 1964.
  - [153] R Glauber. The Quantum Theory of Optical Coherence. *Physical Review*, 130(6):2529–2539, June 1963.
  - [154] N Wiener. Generalized harmonic analysis. *Acta Mathematica*, 55(1):117–258, 1930.
  - [155] A Khintchine. Korrelationstheorie der stationären stochastischen Prozesse. *Mathematische Annalen*, 109(1):604–615, December 1934.
  - [156] R Hanbury Brown and RQ Twiss. Correlation between Photons in two Coherent Beams of Light. *Nature*, 177:27–29, 1956.
  - [157] Y Kuniyama, Y Yoda, K Izumi, M Yabashi, XW Zhang, T Hara, M Ando, and S Kikuta. Two-photon correlations in X-rays from a synchrotron radiation source. *Journal of Synchrotron Radiation*, 4:199–203, 1997.
  - [158] I Müller, RM Klein, J Hollandt, G Ulm, and L Werner. Photon Counting Metrology in NIR. In *The 506th Wilhelm and Else Heraeus-Seminar on Infrared: Science, Technology, and Applications*. Physikalisch-Technische Bundesanstalt, 2012.

# List of Figures

2.1	Schematic of the operation principle of an electrical substitution radiometer (see text). A detailed description is given in chapter 2.3. . . . .	9
2.2	Schematic of a three-element reflection trap detector and the path of light (red line) inside the trap detector. . . . .	11
2.3	Cross section of a typical silicon photodiode. At the Si-SiO <sub>2</sub> interface, located at the intersection of the passivation layer and the bulk silicon, the collection efficiency $P(x)$ is decreased (see text and Figure 2.4). . . . .	13
2.4	Collection efficiency of a silicon p-n-photodiode as a function of distance from the front surface (see text). . . . .	13
2.5	Schematic of the stabilised laser source. The laser beam of the DFB-laser with a wavelength of 760 nm is expanded with the spatial filter to a diameter of about 4 mm. Wedged glasses are used to decouple a fraction of the laser radiation for the feed-back-monitor and the out-of-loop-monitor. . . . .	16
2.6	Photograph of the laser stabilisation setup with $M$ the mirrors, $WP$ the $\lambda/2$ -wave-plate to control the polarisation direction, $SF$ the spatial filter, $WG$ the wedged-glass decoupler for the feed-back-monitor and $FB-D$ the feed-back-monitor. . . . .	17
2.7	Calculated relative change of the emitted laser wavelength due to the modulation of the laser diode current for a period of 4 seconds. The wavelength change was calculated with (2.6) and the output signal of the laser power controller that directly modulates the laser diode current. The change is well below 0.001 nm and is therefore negligible. . . . .	18
2.8	Relative change of the laser power of the stabilised laser radiation measured with the out-of-loop-detector and normalised by the signal of out-of-loop-monitor (see Figure 2.5). . . . .	19
2.9	Comparison of the relative change of the laser power with external stabilisation (red points) and without external stabilisation (green points). The external stabilisation reduces the noise by a factor of approximately 50. . . . .	19

## LIST OF FIGURES

2.10	CAD picture (Figure 2.10(a)) and photograph (Figure 2.10(b)) of the cryogenic radiometer facility set-up in the “detector radiometry” group of PTB. The CAD picture [58] shows the Brewster-window (a), the cryogenic radiometer (b), the detector chamber (c) containing the detectors to be calibrated (DUTs), the cryostat of the “Predictable Quantum Efficient Detector (PQED)” (see chapter 2.1.1) at a spare port (d), the distribution chamber (e) and the bearing (f). The laser radiation enters the setup through the fixed Brewster-window (a) and is then directed onto the cryogenic radiometer and the DUTs by moving the table around the axis (f). The photograph shows the cryogenic radiometer (b), the Predictable Quantum Efficient Detector (d), the detector chamber (c), and the distribution chamber (e). . . . .	22
2.11	Drawing of the cavity and the laser beam path of the new cryogenic radiometer of PTB. The laser beam hits the cavity surface in a distance of $L = 34.15$ mm from the opening aperture ( $2R = 8$ mm). The overall length of the cavity is 51.41 mm. . . . .	23
2.12	Picture of the inside of the new cryogenic radiometer of PTB. The cavity of the cryogenic radiometer of the CRCF is irradiated with laser radiation (red line) through a set of baffles inside the pipe to suppress stray light and thermal radiation detectable with the cavity. . . . .	24
2.13	Normalised heating power of the CRCF-cryogenic radiometer measured without laser radiation. The relative standard deviation of the heating power is $u_{hp} = 2.23 \cdot 10^{-6}$ . . . . .	27
2.14	Cross section (Figure 2.14(a)) and charge density distribution (Figure 2.14(b)) of induced junction photodiodes that are used in the PQED (see text and [70, 71]). The charges are: $Q_{ss}$ positive surface charge, $Q_B$ negative depletion charge, $Q_n$ the inversion layer charge in the silicon and the mirror charge $Q_G$ . . . . .	30
2.15	Induced charge $Q_n$ as a function of surface charge $Q_{ss}$ for different $\text{SiO}_2$ -oxide thicknesses (figure taken from [72]). The blue line indicates the calculation for a $\text{SiO}_2$ -oxide thickness of 50 nm, the red line for 100 nm, the yellow line for 150 nm and the green line for 310 nm. All calculations were made for an applied bias voltage of 0 V, a doping density $N_A = 2 \cdot 10^{12} \text{ cm}^{-3}$ and a temperature of 78 K. To have a working photodiode, $Q_n$ has to be negative. . . . .	31
2.16	Relative spectral responsivity of first batch photodiodes with an $\text{SiO}_2$ -oxide thickness of 100 nm (Figure 2.16(a)) and 300 nm (Figure 2.16(b)). The induced surface charges between $2 \cdot 10^{11} e/\text{cm}^2$ and $4 \cdot 10^{11} e/\text{cm}^2$ were not sufficient to create a working photodiode in the case of a $\text{SiO}_2$ -oxide thickness of 100 nm which results in a highly non-uniform relative spectral responsivity while the photodiode with a $\text{SiO}_2$ -oxide thickness of 300 nm shows a uniform relative spectral responsivity. The relative spectral responsivity was measured with the setup described in chapter 2.4.2. . . . .	32

2.17	The structure of the PQED with two photodiodes in a “wedge” configuration yielding seven reflections [76]. The angle $\beta$ between the photodiodes is set to $15^\circ$ . The first photodiode is irradiated at an angle of incidence of $45^\circ$ . . . . .	34
2.18	Custom made induced junction photodiode on a printed circuit board to be incorporated into a Predictable Quantum Efficient Detector. . . . .	34
2.19	Calculated reflectance of the PQED operated at room temperature for p-polarised radiation. . . . .	36
2.20	Calculated reflectance of the PQED at a temperature of 77 K plotted over the ice layer thickness for wavelengths of 532 nm (Figure 2.20(a)) and 760 nm (Figure 2.20(b)). The reflectance was calculated according to (2.13). The change of reflectance due to ice growth contributes to the uncertainty budget of the PQED at 77 K because the possibility of ice growth cannot be counted out with the present cryostats. . . . .	37
2.21	CAD-drawing of the setup to determine the uniformity of the spectral responsivity. The PQED-photodiodes are mounted in a cryostat (A) to provide clean room like ambient conditions and the possibility to change the temperature down to approximately 80 K. The single PQED photodiode is irradiated by a power stabilised DFB-laser with a wavelength of 760 nm through a fixed Brewster-window at position B (not shown) and mounted inside a cryostat on an x-y-translation stage to scan the uniformity of the spectral responsivity. The laser spot size was approx. 0.5 mm and the laser power was lower than $2.5 \mu\text{W}$ to suppress any non-linearity while measuring. The photodiode temperature was $25^\circ\text{C}$ . . . . .	40
2.22	Schematic of the power stabilised laser source, adopted to enhance the long-term stability. The PQED-photodiodes, the monitor detector, and the feed-back-monitor for the power stabilisation are irradiated by radiation that is decoupled in an identical way. This setup reduces the influence of a change of the polarisation state of the laser radiation at the expense of wanted radiant power. . . . .	41
2.23	Uniformity of the spectral responsivity of a photodiode with a $\text{SiO}_2$ -oxide layer of 300 nm. The figure shows the deviation from the mean of the central photodiode area. The measurement was performed at a wavelength of 760 nm, at room temperature, with a step size of 0.5 mm, and with a reverse bias voltage of 5 V. . . . .	43
2.24	Equivalence circuit of a photodiode in series with a resistance $R_S$ . The symbols are: $I_T$ the radiation generated photocurrent, $V_D$ the forward voltage across the photodiode, $I_D = I_0[\exp(\frac{eV_D}{nkT}) - 1]$ the current through the diode, $R_S$ the series resistance, $V_O$ the output voltage, $R_L$ the load resistance and the output current $I_T$ . The shunt resistance and capacitance of the photodiode are not shown as the influence on the linearity of the photodiode of these parameters can be neglected. . . . .	44

## LIST OF FIGURES

2.25	Non-linearity of sample PQED photodiodes with a 300 nm SiO <sub>2</sub> -oxide layer (Figure 2.25(a)) and a 220 nm SiO <sub>2</sub> -oxide layer (Figure 2.25(b)). No non-linearity was detected within the uncertainty of the measurements of $3 \cdot 10^{-5}$ (marked as grey shaded area in the figures) up to a radiant power level 300 $\mu$ W at a wavelength of 760 nm, a bias voltage of 5 V and room temperature. . . . .	45
2.26	Non-linearity of a 220 nm SiO <sub>2</sub> -oxide layer photodiode up to a laser power of 450 $\mu$ W. To reach the higher radiant power level the laser stabilisation had to be removed which led to higher scatter of the measurement points. At a photocurrent of 450 $\mu$ A sub-linearity occurs due to the series resistance of the photodiodes (see text). The non-linearity could not be measured at higher photocurrents due to the limited available laser power. The uncertainty of the measurements of $8 \cdot 10^{-5}$ is marked as grey shaded area. . . . .	47
2.27	Measured deviation of the bias dependent photocurrent from the value at 5 V bias of the PQED plotted over the bias voltage for a laser wavelength of 532 nm (Figure 2.27(a)) and 760 nm (Figure 2.27(b)). The photocurrent $I_{\text{phot}}$ was determined by subtracting the bias dependent dark current from the output under illumination. The squares show results at room temperature and circles show the results at the temperature of liquid nitrogen. . . . .	48
2.28	Photograph of the stray light detector. The cover is made from blackened metal and has a circular aperture slightly larger than the apertures of the detectors used and a blackened metal disc in the centre with a diameter slightly smaller than the apertures of the detectors. This detectors measures the stray light in the vicinity of the apertures of the cryogenic radiometer and the PQED. . . . .	50
2.29	Comparison of measured (circles) and predicted (squares) external quantum deficiency of the PQED for the wavelengths 532 nm and 760 nm. The uncertainty of the predicted external quantum deficiency for the 760 nm, 78 K and 5 V reverse bias voltage is highly increased as compared to the other values. At this condition a higher fraction of photons is absorbed behind the n-p-junction, where the collection efficiency is decreased (see text). . . . .	51
2.30	Comparison of the measured internal quantum deficiency of two trap detectors made from Hamamatsu S1337 photodiodes (red) that are used at PTB as transfer standards and of the PQED (green) plotted over the wavelength. . . . .	52
2.31	Comparison of the calculated reflectance of a three-element trap detector made from Hamamatsu S1337 photodiodes (blue) and of the PQED for p-polarised (green) and s-polarised (red) radiation plotted over the wavelength. . . . .	53
3.1	Cross sections of “thin” and “thick” single photon avalanche photodiodes. . . . .	59

3.2	Schematics of the supercurrent-assisted hotspot formation mechanism in an ultra-thin and narrow superconducting strip, kept far below the critical temperature are shown (see text). The arrows indicate the direction of the supercurrent flow. . . . .	61
3.3	Schematic of the setup (Figure 3.3(a)) and photograph of the inside of the light-tight enclosure (Figure 3.3(b)) used to calibrate a Single Photon Counting Module (SPCM) with attenuated laser radiation. Both detectors, trap detector (trap) in connection with the switch integrator amplifier (SIA) and SPCM, are mounted on a translation stage that allows the irradiation of the detectors at the same position with the same radiant power. The lens in front of the SPCM is necessary to achieve an under-filling of the active area of the SPCM with the laser radiation. . . .	69
3.4	Result of a measurement sequence containing several measurements of the photon rate with the reference trap detector (green squares) and several photon counting measurements with the SPCM (red circles). The uncertainty bars of the photon counting measurements are smaller than the red circles. . . . .	70
3.5	Calculated spectral radiant power of synchrotron radiation sources used by PTB as primary source standards with different characteristic photon energies compared with a blackbody radiator [138]. . . . .	72
3.6	Photon statistic correction $[p(2) + p(3)]p(1)^{-1}$ plotted over the photon rate of the Metrology Light Source for the assumptions, thermal radiation (green line) and coherent radiation (red line). . . . .	76
3.7	Schematic of the setup to measure the coincidence rate of the synchrotron radiation (Figure 3.7(a)) and the resulting number of coincidences (Figure 3.7(b)). The spectrally filtered radiation of the Metrology Light Source has been fed into a fibre-coupled Hanbury-Brown and Twiss setup (HBT) [156] with the detectors D1 and D2. The schematic shows the fibre-coupled beamsplitter with a splitting ratio of 50/50 (50/50 BS), the two SNSPDs (D1 and D2), and the coincidence counter. The systematic temporal evolution of the bunch structure of the synchrotron radiation introduces a high amount of, so-called [150], trivial correlation. The measured value of $g^{(2)}(0)$ without normalisation is 1.13, i.e. significantly higher than the estimated value $g_e^{(2)}(0) = 1.006$ . . . . .	80
3.8	Schematic of the extended setup of that shown in Figure 3.7(a) to measure the photon statistics of the Metrology Light Source (see Figure 3.8(a)) to take into account the trivial coincidences due to the electron bunch structure (see Text) and the resulting normalised coincidences (Figure 3.8(b)). The measured value of $g^{(2)}(0)$ of $1.0049 \pm 0.0008$ is close to the estimated value $g_e^{(2)}(0) = 1.006$ . . . . .	81

## LIST OF FIGURES

- 3.9 Schematic of the setup used to calibrate Single Photon Avalanche Diodes (SPADs). The photon rate ( $PR_{I_{\text{high}}}$ ) in the high ring current range was measured in the focus of the synchrotron radiation by a calibrated trap detector using its known responsivity  $S_{\text{trap}}(\lambda)$ . In a second step the count rate of the SPAD  $CR_{\text{SPAD}}$  was measured in the low ring current range. The uncorrected detection efficiency of the SPAD  $DE_{\text{SPAD}}^*$  can then be calculated according to equations (3.46) to (3.50). . . . . 83
- 3.10 Count rate of SPAD1 and SPAD2 (black crosses) per stored electron (left scale) and number of stored electrons (blue line measured electron number, red line guidance for the eye, right scale) vs. measurement time. The discrete steps in the red and blue line are due to electron losses (figure taken from [13]). . . . . 84
- 3.11 Schematic of the setup used to determine the correction factor for the different detector sizes of SPAD and trap detector. The photodiode signal was measured for three configurations, without pinhole and with pinholes with a diameter of  $149\ \mu\text{m}$  and  $196\ \mu\text{m}$ . The results are given in Table 3.1. 86
- 3.12 Stability of the transmission through a  $196\ \mu\text{m}$  pinhole and, thus, of the vertical source size  $\varepsilon$  of the synchrotron radiation. The relative standard uncertainty of the measurement is given by the uncertainty of the ratio of the photocurrent and the ring current  $u_{I_{\text{trapnorm}}} = 0.051\%$ . The spike at 50 mA ring current arises from a short instability of the cooling system of the Metrology Light Source and has been neglected. . . . . 86
- 3.13 Uniformity of the two calibrated SPADs. Figure 3.13(a) shows SPAD1 and Figure 3.13(b) shows SPAD2. The measurements were performed with an attenuated He-Ne laser at a wavelength of 633 nm and a spot size smaller than  $15\ \mu\text{m}$ . The active diameter, obtained from the full width at half maximum diameter, is  $210\ \mu\text{m}$  for both devices. . . . . 88
- 3.14 Visualisation of the input parameters for the equations (3.52), (3.53) (see text). The figures show the calculated spectral radiant power of the Metrology Light Source (Figure 3.14(a)), the transmittance of the interference filter (Figure 3.14(b)) taken from the data sheet, the detection efficiency of the SPADs (Figure 3.14(c)) taken from the data sheet [96], and the measured spectral responsivity of the reference detector (Figure 3.14(d)). . . . . 89
- 3.15 Output signal of SPAD1 measured with an oscilloscope. The photon induced output voltage pulse (time span 0 ns to 20 ns) is followed by a, so-called, afterpulse (time span 28 ns to 48 ns) directly after the end of the dead time of SPAD1 of 28 ns. . . . . 90

3.16	Schematic of the setup used to calibrate a fibre-coupled superconducting nanowire single photon detector (SNSPD). The photon rate ( $PR_{I_{\text{high}}}$ ) in the high ring current range is measured by a calibrated InGaAs reference detector using its known responsivity $S_{\text{IGA}}(\lambda)$ . In a second step the count rate of the SNSPD $CR_{\text{SNSPD}}$ is measured in the low ring current range. Both detectors are, depending on the ring current, alternately connected to the same optical fibre. The uncorrected detection efficiency of the SNSPD $DE_{\text{SNSPD}}^*$ can then be calculated according to equations (3.46) to (3.50). . . . .	93
3.17	Ratio of the photon rate ( $PR$ ) to the number of stored electrons ( $N$ ) (red circles) and ratio of the count rate of the SNSPD ( $CR_{\text{SNSPD}}$ ) and the number of stored electrons ( $N$ ) (green squares) plotted over the electron ring current of the Metrology Light Source. The uncertainty of the measured ring current and, thus, of the measured ratios in the high ring current range was $u_{I_{\text{InGaAsnorm}}} = 0.53\%$ and $u_{\text{CR}} = 0.075\%$ in the low ring current regime. . . . .	95
3.18	Measured detection efficiency (green squares) and dark count rate (red circles) of the SNSPD plotted over the bias current normalised to the critical bias current. The uncertainty bars of the measured detection efficiency are about the same size as the green markers. . . . .	96
3.19	Relative change of the fibre-coupling efficiency of the synchrotron radiation of the Metrology Light Source into the optical fibre at $1.55 \mu\text{m}$ plotted over the electron beam current. Within the uncertainties of the ring current measurement no systematical dependence of the coupling efficiency on the electron beam current has been detected for ring currents below 1 mA (figure taken from [158]). . . . .	98



# List of Tables

2.1	The relative difference of the heater power of the regular heater and of the additional heater at a different position and the standard uncertainty of this difference. The measurements were performed at a heater power of 350 $\mu\text{W}$ and 750 $\mu\text{W}$ . . . . .	25
2.2	Uncertainty budget of the radiant power measurement for the CRCF and it's predecessor RTCR without uncertainty contributions from the DUTs. The uncertainty budget of the RTCR was taken from [66], The instrumental uncertainties are stated for a calibration of the DMMs not longer than 90 days before usage. . . . .	28
2.3	Predicted reflectance $r_{\text{PQED}}(\lambda)$ , predicted internal quantum deficiency $iQD(\lambda)$ , and predicted external quantum deficiency $\Delta_p$ for the comparison conditions at the new CR-facility of PTB. The uncertainties are stated with a coverage factor $k = 2$ (see text). For asymmetric uncertainty boundaries, the lower and upper boundaries are indicated by the subscript and superscript, respectively. The uncertainties of $r_{\text{PQED}}$ and $iQD(\lambda)$ are added quadratically to obtain the uncertainty of $\Delta_p$ . The values of $iQD(\lambda)$ are taken from [17] and the estimation of the uncertainty of $r_{\text{PQED}}(\lambda)$ is taken from [18]. . . . .	39
2.4	Measured relative uniformity of the spectral responsivity of a randomly chosen photodiode of each type produced. The measurements were performed at a wavelength of 760 nm. The uniformity is given as the standard deviation of the measured points normalised by the monitor detector, the reference point and the mean of the photocurrent measured at the positions inside the electrode ring (see Figure 2.14(a) and Figure 2.18). . . . .	42
2.5	Main contributions to the uncertainty budget of the PQED validation measurements. Relative standard uncertainties are stated. *The stray light uncertainty contains the positional error of the detectors and the difference of the apertures in front of the detectors. . . . .	50
2.6	Comparison of predicted and measured external quantum deficiency of the PQED at different temperatures $T$ , wavelengths $\lambda$ , and reverse bias voltages $U_{\text{bias}}$ . The uncertainties are given at 95% confidence level. For the asymmetric uncertainty boundaries of $\Delta_p(\lambda)$ , the lower and upper boundaries are indicated by the subscript and superscript, respectively. . .	51

## LIST OF TABLES

3.1	Measurement of the radiation losses associated with the two different pin-holes and the linear extrapolated value* for an active SPAD diameter of 210 $\mu\text{m}$ . . . . .	87
3.2	Relative standard uncertainties and correction factors contributing to the traceable calibration of the detection efficiency of two SPADs using synchrotron radiation. . . . .	91
3.3	Measurement of the repeatability of the polarisation adjustment of the radiation incident on the SNSPD. The counts were integrated over a period of 30 s. . . . .	97
3.4	Relative standard uncertainties and correction factors contributing to the traceable calibration of a SNSPD by means of synchrotron radiation. . . .	99

# List of own Publications

Parts of this thesis have been published in:

## Peer-reviewed journal articles

**I Müller**, R Klein, J Hollandt, G Ulm & L Werner. Traceable calibration of Si avalanche photodiodes using synchrotron radiation. *Metrologia*, **49**(2):152–155, April 2012.

J Gran, T Kübarsepp, M Sildoja, F Manoocheri, & **I Müller**. Simulations of a predictable quantum efficient detector with PC1D. *Metrologia*, **49**(2):130–134, April 2012.

M Sildoja, F Manoocheri, M Merimaa, E Ikonen, **I Müller**, L Werner, J Gran, T Kübarsepp, M Smid, & ML Rastello. Predictable quantum efficient detector: I. Photodiodes and predicted responsivity. *Metrologia*, **50**(4):385–394, July 2013.

**I Müller**, U Johannsen, U Linke, L Socaciu-Siebert, M Smid, G Porrovecchio, M Sildoja, F Manoocheri, E Ikonen, J Gran, T Kübarsepp, G Brida, & L Werner. Predictable quantum efficient detector: II. Characterization and confirmed responsivity. *Metrologia*, **50**(4):395–401, July 2013

## Conference contributions

**I Müller**, R Klein, J Hollandt, G Ulm & L Werner (2011). Towards traceable calibration of Si-avalanche photodiodes using synchrotron radiation. In *Proceedings of Single Photon Workshop 2011*, Braunschweig, Germany.

G Brida, J Cheung, I Degiovanni, M Gramegna, MG Mingolla, T Kübarsepp, **I Müller**, G Porrovecchio, ML Rastello, M Smid, & L Werner (2011). Toward Traceable Few Photon Radiometry. In *Proceedings of NEWRAD 2011*, pages 293–294, Maui, Hawaii, USA.

M Sildoja, F Manoocheri, M Merimaa, E Ikonen, **I Müller**, L Werner, J Gran, T Kübarsepp, M Smid, & ML Rastello (2011). Predictable quantum efficient detector I: Photodiodes and design. In *Proceedings of NEWRAD 2011*, pages 227–228, Maui, Hawaii, USA.

**I Müller**, G Brida, J Gran, SS Hoem, E Ikonen, T Kübarsepp, U Linke, F Manoocheri, M Sildoja, M Smid, L Socaciu-Siebert & L Werner (2011). Predictable Quantum Effi-

cient Detector II: Characterization Results. *In Proceedings of NEWRAD 2011*, pages 209–210, Maui, Hawaii, USA.

SS Hoem, J Gran, M Sildoja, F Manoocheri, E Ikonen, & **I Müller** (2011). Physics of self-induced photodiodes. *In Proceedings of NEWRAD 2011*, pages 259–260, Maui, Hawaii, USA.

F Manoocheri, M Sildoja, M Merimaa, E Ikonen, **I Müller**, L Werner, J Gran, SS Hoem, T Kübarsepp, G Porrovecchio, M Smid, G Brida, & ML Rastello (2011). Predictable quantum efficient detector. *In Proceedings of NEWRAD 2011*, pages 13–14, Maui, Hawaii, USA.

J Gran, T Kübarsepp, M Sildoja, F Manoocheri, E Ikonen, & **I Müller** (2011). Simulations of Predictable Quantum Efficient Detector with PC1D. *In Proceedings of NEWRAD 2011*, pages 263–264, Maui, Hawaii, USA.

**I Müller**, R Klein, J Hollandt, G Ulm & L Werner (2011). Traceable calibration of Si-avalanche photodiodes using synchrotron radiation. *In Proceedings of NEWRAD 2011*, pages 288–289, Maui, Hawaii, USA.

**I Müller**, R Klein, J Hollandt, G Ulm, & Werner, L. (2012). Photon Counting Metrology in NIR. *Presented at the The 506th Wilhelm and Else Heraeus-Seminar on Infrared: Science, Technology, and Applications*, Bad Honnef, Germany.

**I Müller**, S Kück & R Klein (2013). Traceable Calibration of a fibre-coupled superconducting nano-wire single photon detector using synchrotron radiation. *Presented at the Single Photon Workshop 2013*, Oak Ridge National Laboratory, Knoxville, Tennessee, USA.

### Magazine article

**I Müller**. Wave meets particle. *PTB-news*, 2012(2), 4.

# Acknowledgement

Over the past five years I have received support and encouragement from a great number of individuals.

First of all, I would like to gratefully and sincerely thank Dr. Lutz Werner for his guidance, understanding and patience during my graduate studies at PTB. His mentorship was paramount for the achievements of this work. He encouraged me to grow as a experimental physicist and an independent thinker.

I also would like to thank Prof. Oliver Benson, who supervised this work despite his many other academic and professional commitments. His wisdom, knowledge and dedication to the highest standards inspired and motivated me.

Furthermore, I also would like to thank Dr. Jörg Hollandt and Dr. Gerhard Ulm for giving me the chance of working at PTB and their support in extending the framework of this thesis to quantum radiometry.

Especially, I would like to thank Uwe Johannsen for his assistance and guidance that helped me to make the first successful steps at PTB and for his help and work to setup the new cryogenic radiometer facility.

I would like to express my gratitude for the precious support of Dr. Liana Socaciu-Siebert, for her help concerning the measurements for the characterisation and validation of the PQED.

I would also like to thank Ulrike Linke, for setting up the detector non-linearity facility and writing the software for the new cryogenic radiometer.

I am very thankful to Katrin Vogel, for the calibrations of PQED photodiodes and a trap detector over and above her high working load.

I would like to thank all my colleagues in the working group detector radiometry namely Dr. Peter Meindl for pushing me beyond my limits, Josef Breuer for introducing me into LabView and taking care of my security, Jürgen Schirren for helping me solving

all my electrical problems and Martin Wähler for being the best room mate so far.

Furthermore, I would also like to acknowledge, with much appreciation, the crucial role of the staff of the Metrology Light Source and most of all Dr. Roman Klein, who operated the Metrology Light Source during the measurements with synchrotron radiation described in this work. He gave the permission to use all required equipment and the necessary materials to complete the measurements on the synchrotron calibration method.

I would like to thank all the colleagues working at PQED project, especially Prof. Erkki Ikonen, Dr. Farshid Manoocheri and Meelis Sildoja for their hard work on the construction of the PQED.

Finally, and most importantly, I would like to thank my family which always supported me and is the bedrock of my life.

# Selbstständigkeitserklärung

Ich erkläre, dass ich die vorliegende Arbeit selbstständig und nur unter Verwendung der angegebenen Literatur und Hilfsmittel angefertigt habe.

Berlin, den 16.10.2013

Ingmar Müller